University of Science and Technology of China

Hefei, CHINA

Di-lepton production measurements in p+p and Au+Au collisions at RHIC

A dissertation submitted

for the degree of

Doctor of Philosophy in Physics

by

Bingchu Huang

黄柄矗

Co-supervisors: Ziping Zhang, Lijuan Ruan

2011

© Copyright by

Bingchu Huang

黄柄矗

2011

All Rights Reserved

Dedicated to my dear family

谨献给我亲爱的父母

Acknowledgments

First and foremost I would like to express my deepest gratitude to Prof. Ziping Zhang and Hongfang Chen for introducing me to the relativistic heavy-ion physics research. With their encouragement, tremendous support and sound advice, they make the research interesting for me. I would like to thank Dr. Timothy Hallman, Dr. James Dunlop and Prof. Zhangbu Xu for offering me the opportunity to work at BNL. Prof. Zhangbu Xu provided me wise advice, excellent ideas and brilliant guidance in my research. I learned a lot from him and I want to express my sincerely thanks to him.

I would especially thank Dr. Lijuan Ruan for guiding me through all the detailed analysis in my research for two years. Her perpetual energy and enthusiasm in research had motivated me. She offered me plenty helps and fruitful discussions. I benefit a lot from her guidance. I would have been lost without her.

I would like to thank Dr. Yifei Zhang who introduced me into the data analysis. He keeps offering me the help in my research. My thanks also go to Dr. Xin Dong, Dr. Zebo Tang, and Dr. Yichun Xu for their amount of fruitful discussions on work. I would like to thank Dr. Jian Deng for his valuable discussions. I would like to thank Mr. Jie Zhao and Liang Xue, my roommates in BNL, for enjoyable corporation on work and living and abundant helpful discussions. I would like to thank Ms. Xiangli Cui and Mr. Hao Qiu for their assistances in my research.

I would like to express my thanks to the STAR group colleagues at BNL and High Energy Physics Group colleagues at USTC, especially Prof. Zizong Xu, Prof. Xiaolian Wang, Prof. Qun Wang, Prof. Ming Shao, Dr. Yi Zhou, Mr. Haojie Xu, Mr. Hui Zeng.

I would like to thank the STAR physics working groups (PWG) especially the convenors for providing healthy physics discussions. I also thank Dr. Nu Xu, Dr. Bedanga Mohanty, and Dr. Aihong Tang for helpful suggestions and discussions.

I would like to thank all my friends for inspiring me in research and life during the

hours we spent together at USTC and BNL. They are, for example, Hongwei Ke, Shusu Shi, Na Li, Xiaoping Zhang, Chengming Du, Yan Yang, Lizhu Chen, Yi Guo, Chi Yang, Liang Zheng and so on.

Finally, my deep gratitude goes to my family for their unflagging love and support throughout my life. This dissertation is impossible without them.

摘要

位于美国布鲁克海文国家实验室（BNL）的相对论重离子对撞机（RHIC）用于在实验室条件下产生接近大爆炸后大约几十微秒的宇宙早期极端条件的强相互作用的物质。一种具有强关联的夸克胶子等离子态（sQGP）被认为已经在RHIC的重离子碰撞中产生。研究QGP的未知行为和性质成为当前最感兴趣的物理学课题之一。电磁相互作用探针，例如双轻子，能够穿过重离子碰撞中产生的热密物质而只受到极小的末态作用，能够携带重离子碰撞中整个演化过程中的信息。它们被认为是研究sQGP的关键性的探针。

螺旋管径迹探测器（STAR）是RHIC上最大的实验装置。STAR近年升级完成的飞行时间探测器（TOF）使得双轻子的测量成为可能。本文中我们给出了在2009年RHIC的质心能量200 GeV的质子-质子碰撞和2010年RHIC的每核子对质心能量为200 GeV的金核-金核碰撞中双轻子对的产额的测量结果。质子-质子碰撞中的双轻子质量谱与由模拟轻介子以及重味夸克介子双轻子衰变得到的质量谱一致。从质子-质子碰撞中双轻子道测量到的ω介子的不变产额谱与PHENIX合作组已发表的结果一致。金核-金核碰撞中的ω介子的不变产额谱符合Tsallis爆炸波（TBW）模型拟合的预期。从质子-质子碰撞双轻子道中提取的ϕ介子和J/ψ介子的不变产额与之前已发表的测量结果相符合。测量得出新的$\eta \to e^+e^-$衰变分支比上限为4.3×10^{-6}，约为现有的分支比上限的五分之一。从双轻子谱中拟合得到的质子-质子碰撞中粲夸克的产生截面为$0.96 \pm 0.10(stat.) \pm 0.27(syst.)\ mb$.

质子-质子碰撞中测得的双轻子谱为金核-金核碰撞中的研究提供了参考。与模拟结果相比，我们观测到的金核-金核碰撞中的双轻子产额在小不变质量区间是预计的产额的$1.53 \pm 0.07(stat.) \pm 0.41(syst.)$倍。双轻子质量谱与PHENIX的测量结果的比较将会在本文中给出。

ABSTRACT

The Relativistic Heavy Ion Collider at Brookhaven National laboratory (BNL) was built to create strongly interacting matter in a laboratory setting to reach extreme condition of the early universe where a few tens of microseconds following the Big Bang. A strongly coupled Quark Gluon Plasma (sQGP), is believed that has been created in heavy ion collisions at RHIC. The study of unobserved behaviors and properties of QGP becomes one of the most interesting physics topics. Electro-magnetic probes, *i.e.* lepton pairs, can penetrate the hot dense matter created in heavy ion collisions with minimal final state interaction, bring the whole evolution information of the heavy ion collisions. They are considered as the crucial probes for the sQGP.

The analysis is carried out at the Solenoidal Tracker at RHIC (STAR) experiment. The newly installed Time-of-Flight (TOF) enables the di-electron study at STAR. In this thesis, we present measurement of di-electron pairs production from p+p collisions at $\sqrt{s}$ = 200 GeV in year 2009 RHIC run and Au+Au collisions at $\sqrt{s_{\rm NN}}$=200 GeV during year 2010 RHIC run with the STAR detector. The di-electron mass spectrum in p+p is consistent with the simulations of di-electrons from light meson decays and heavy flavor decays (charmonium and open charm correlation). The extracted $\omega \rightarrow e^+e^-$ invariant yields in p+p are consistent with the previous publication. The invariant yields of ω in Au+Au are measured and consistent with the Tsallis-Blast-Wave model fit. The extracted dN/dy of ϕ and J/ψ in p+p, through their di-electron channels are consistent with the previous measurements of $\phi \rightarrow K^+K^-$ and $J/\psi \rightarrow e^+e^-$. The new upper limit of the branching ratio of the $\eta \rightarrow e^+e^-$ is 4.3×10^{-6}, a factor of six below the world limit. The charm cross section extracted from the simultaneously fit of di-electron mass spectrum, previous published D, and non-photonic electron spectra is $0.96 \pm 0.10(stat.) \pm 0.27(syst.)\ mb$.

The di-electron continuum measured in p+p provides a reference for the study in Au+Au. We observed an enhanced factor of $1.53 \pm 0.07(stat.) \pm 0.41(syst.)$ of di-electron

yields in Low Mass Region (LMR) in minimum bias Au+Au collisions compared to the cocktail simulation. Comparison between STAR data and PHENIX results will be discussed.

Table of Contents

1 Physics **1**

1.1 Quantum Chromodynamics 1

1.1.1 Asymptotic freedom 2

1.1.2 Deconfinement and phase diagram 3

1.1.3 Chiral symmetry 5

1.2 Di-leptons 11

1.3 Exotic decay 14

1.4 Previous experimental results 14

1.4.1 NA60 15

1.4.2 PHENIX 16

2 Experiment Set-up **20**

2.1 RHIC Accelerator Complex 20

2.2 STAR Detector 22

2.2.1 Time Projection Chamber 24

2.2.2 Barrel Electro-Magnetic Calorimeter 29

2.2.3 Barrel Shower Maximum Detector 32

2.2.4 Barrel Time of Flight 33

2.3 Detector upgrades 42

3 Di-electron production analysis **43**

3.1 Data Sets and Event Triggers 43

3.1.1 p+p collisions 43

3.1.2 Au+Au collisions 44

3.2 Electron Identification 46
3.3 Pair reconstruction 53
3.3.1 Background analysis 53
3.3.2 Normalization 54
3.4 Efficiency and Acceptance 57
3.4.1 In p+p collisions 59
3.4.2 In Au+Au collisions 61
3.4.3 Pair detection efficiency 63
3.5 Cocktail simulation 65
3.5.1 Light flavor meson 65
3.5.2 Heavy flavor contribution 68
3.6 Systematic uncertainties 71

4 Results and Discussion 77
4.1 Di-electron production in p+p Collisions at 200 GeV at STAR 77
4.1.1 Charm cross section in p+p at 200 GeV 79
4.1.2 Yields of ϕ and J/ψ in p+p at 200 GeV 81
4.1.3 Rare decay 81
4.2 ω meson yields in p+p and Au+Au Collisions at 200 GeV at STAR 82
4.3 Di-electron production in Au+Au Collisions at 200 GeV at STAR 86
4.3.1 Comparison of STAR and PHENIX di-electron continuum 88

5 Summary and Outlook 92
5.1 Summary 92
5.2 Outlook 92

A Publication list **95**

References **97**

List of Figures

1.1 Summary of measurements of α_s as a function of the respective energy scale Q. The figure is taken from [Bet09]. 3

1.2 Schematic picture of the QCD phase diagram shown in $T \approx \mu_B$ space [USA07]. 4

1.3 Scalar potential Eq. 1.18 for $\mu^2 > 0$ (a) and for $\mu^2 < 0$ (b). 8

1.4 The expectation value of the quark condensate. Calculation is based on the Nambu-Jona-Lasinio model [KLW90]. Figure is from [Her01]. 11

1.5 Schematic di-lepton mass distribution of ultra-relativistic heavy ion collisions.Figure is from [Her01]. 12

1.6 Feynman diagram for Drell-Yan process 13

1.7 Left panel:Di-muon invariant mass spectrum before(dots) and after subtraction of the known decay sources(triangle). Right panel: Comparison between excess dimuons and theoretical predictions [Rap02]. Figure is from [Dam08]. 15

1.8 Left panel: a fit of the weighted offset distribution of $\mu^+\mu^-$ pairs to prompt and charm decays in the IMR region. Right Panle: acceptance corrected excess yield compared to Drell-Yan, open charm decays. Figure is from [Dam08]. 16

1.9 T_{eff} of the excess m_T-spectra vs. $\mu^+\mu^-$ pair mass. Figure is from [Arn08]. 17

1.10 Left: inclusive mass spectrum of e^+e^-pairs in the PHENIX acceptance in p+p collisions. The expectation from the light hadrons decays, correlated open charm, bottom decays and Drell-Yan compared to the e^+e^-signals. Right: inclusive mass spectrum of e^+e^-pairs in the PHENIX acceptance in minimum bias Au+Au. The expected contributions from the decays of light hadrons and correlated decays of charm bottom and Drell-Yan compared to the e^+e^-continuum. Figure is from [Ada10]. 18

1.11 Comparison of PHENIX di-electron continuum in Au+Au collisions in the LMR to the sum of cocktail (a) and the contribution from different models. Calculations are from: Panel (b) Rapp and van Hees [Rap01, Rap02],Panel (c) Dusling and Zahed [DZ09, DTZ07, DZ10], and panel (d) Cassing and Bratkovskays [MBC11, CB99, BC08]. Figure is from [Ada10]. 19

2.1 Schematic of the RHIC complex. 21

2.2 STAR detectors. 22

2.3 Cutaway side view of the STAR detectors. 24

2.4 The STAR TPC surrounds a beam-beam interaction region at RHIC. The collisions take place near the center of the TPC [And03]. 25

2.5 The anode pad plane with one full sector shown. The inner subsector is on the right and it has small pads arranged in widely spaced rows. The outer subsector is on the left and it is densely packed with larger pads. 27

2.6 Distribution of $log_{10}(dE/dx)$ as a function of $log_{10}(p)$ for electrons, pions, kaons and protons. The units of dE/dx and momentum are keV/cm and GeV/c, respectively. The color bands denote within $\pm 1\sigma$ the dE/dx resolution. I70 means Bichsel's prediction for 30% truncated dE/dx mean. . . 29

2.7 Side view of a calorimeter module showing the projective nature of the towers. The 21st mega-tile layer is also shown in plan view. 30

2.8 End view of a STAR BEMC module showing the mechanical assembly including the compression components and the rail mounting system. The location of the two layers of shower maximum detector at a depth of approximately $5X_0$ from the front face at $\eta = 0$ is also shown. 31

2.9 Schematic illustration of the double layer STAR BSMD. Two independent wire layers, separated by an aluminum extrusion, image electromagnetic showers in the η and ϕ on corresponding pad layers. 32

2.10 Two side views of MRPC. The upper (lower) is for long (short) side view. The two plots are not at the same scale. 34

2.11 Geometry of trays, modules and pads. 35

2.12 An example of tdc vs. tot correlation for VPD slewing correction. The units are ns for each axis. The blue squares are the data points, the red lines represent the Spline fit. 37

2.13 TOF tray calibration procedures. 39

2.14 Overall resolution of TOF system in run 10 fast offline production. 40

2.15 Left: M^2 vs. momentum distribution after TOF calibrations. Right: inverse velocity vs. momentum distribution after TOF calibrations. 40

2.16 Top two panels: $n\sigma_{dE/dx}$ as function of mass measured by TOF system. Bottom panel: the masses of Helium-3 and Helium-4 and their anti particles. Figure is from [Aga11b]. 41

3.1 Left: Vz vs. VpdVz distribution. Right: Vertex z difference between TPC and VPD measured value in p+p collisions, fit by Gaussian function. . . . 44

3.2 Vertex z difference between TPC and VPD measured value, fit by Gaussian function. 46

3.3 Inverse velocity $1/\beta$ vs. p in p+p collisions from the TOF at $|\eta| < 1$. The red line indicates the PID cut $|1/\beta - 1| < 0.03$. 47

3.4 The normalized dE/dx distribution as a function of p_T with the cut of $|1/\beta - 1| < 0.03$ in p+p collisions. 47

3.5 Left: 2-Gaussian fit, Right: exponential + Gaussian fit. 49

3.6 Left: 2-Gaussian fit, Right: exponential + Gaussian fit. 50

3.7 Left: 2-Gaussian fit, Right: exponential + Gaussian fit. 51

3.8 Left: 2-Gaussian fit, Right: exponential + Gaussian fit. 52

3.9 nσ_e width fit. 52

3.10 Electron purity estimation from two kinds of fit. 52

3.11 nσ_e cuts efficiency and the purity after fixing width fit for electron candidates as a function of p_T at $|\eta| < 1$ in p+p. 52

3.12 The normalized dE/dx distribution as a function of p_T with the cut of $|1/\beta - 1/\beta_{mean}| < 0.03$ in Au+Au collisions. 52

3.13 The difference between real and mixed-events like-sign distributions divided by its standard deviation $(N_{\pm\pm} - A \times B^{comb}_{\pm\pm})/\sigma_{N_{\pm\pm}}$ in p+p data (left) and in PYTHIA [SMS06] (right). The background $B^{comb}_{\pm\pm}$ is normalized to the foreground $N_{\pm\pm}$ in the normalization range $0.4 < M_{ee} < 1.5$ GeV/c^2, A is the normalization factor. 55

3.14 Panel (a): The ratio of like-sign over mixed-event distributions in minimum-bias p+p collisions. Panel (b): The ratio of like-sign over mixed-event distributions in EMC triggered p+p collisions. Panel (c): The $\Delta\phi$ distribution of the difference of the azimuthal angles. of the two electrons in the unlike-sign, like-sign and mixed-event pairs in minimum-bias p+p collisions. Panel (d): The $\Delta\phi$ distributions of like-sign and mixed-event pairs by selecting $M_{ee} > 1$ GeV/c^2in minimum-bias p+p collisions. Errors are statistical. 56

3.15 The e^+e^-pair invariant mass distributions for unlike-sign foreground, like-sign and mixed-event background. Left is for p+p collisions, right is for Au+Au collisions. 57

3.16 The signal over background ratio. Left is for p+p collisions, right is for Au+Au collisions. 57

3.17 Background-subtracted mass spectrum for dielectrons. Left is for p+p collisions, right is for Au+Au collisions. 58

3.18 *nDedx* cut efficiency in p+p at 200 GeV. 60

3.19 The TOF efficiency as a function of tray ID. Tray 1-60 is at $\eta > 0$, with tray 1 covering 75 to 80 degree in azimuth, tray 2 covering 81 to 86, and so on. Tray 61-120 is $\eta < 0$, with tray 61 covering 105 to 110 degree in azimuth, tray 62 covering 111 to 116, and so on. The gaping hole corresponds to the 28% trays that still needed to be installed in 2009. 60

3.20 $1/\beta$ cut efficiency in p+p at 200 GeV. 60

3.21 The efficiency for single electrons as a function of p_T in p+p collisions at $\sqrt{s_{\rm NN}}$= 200 GeV. 60

3.22 The efficiencies calculate from data in Au+Au collisions. Black dots represent *nDedx* cut efficiency. Open circles are The TOF $1/\beta$ efficiency at low momentum. Red stars show the nσ_e cut efficiency. 62

3.23 The efficiency for single electrons as a function of p_T in the pseudo-rapidity of $|\eta| < 1$ in Au+Au collisions at $\sqrt{s} = 200$ GeV . Blue triangle is the TPC tracking efficiency. Open circles represent TOF matching efficiency. 62

3.24 (a) The M_{ee} distribution within STAR acceptance with the efficiency factors for single electrons set to be 100% (solid line) or be the correct (dashed line). (b) The efficiency of di-electron continuum as a function of M_{ee} within the STAR acceptance, which is $|y_{e^+e^-}| < 1$, $|\eta_e| < 1$, and $p_T(e) > 0.2$ GeV/c, in p+p collisions at $\sqrt{s} = 200$ GeV. 64

3.25 (a) The M_{ee} distribution within STAR acceptance. The descriptions for lines are same as Fig. 3.24. (b) The efficiency of e^+e^-pair efficiency in Au+Au at $\sqrt{s_{\rm NN}}$= 200 GeV. 64

3.26 The Tsallis Blast-Wave fit for meson measurements in p+p at 200 GeV. . . 66

3.27 The Tsallis Blast-Wave fit for meson and baryon measurements in Au+Au at 200 GeV. 66

3.28 Fit the simulated $b \to e/NPE_{run8}$ to the ratio of $b \to e$ to $b \to e{+}c \to e$ in p+p at 200 GeV. 69

3.29 The fixed $b \rightarrow e$ and $c \rightarrow e$ from PYTHIA simulation. 69

3.30 Comparisons of $c \rightarrow e$ and D^0 yields data and PYTHIA simulation in p+p at 200 GeV. 71

3.31 The cocktail within STAR acceptance in p+p at 200 GeV. 72

3.32 The cocktail within STAR acceptance in Au+Au at 200 GeV. 73

3.33 Systematic uncertainties as a function of mass from different source contributions in p+p at 200 GeV. Also shown are the systematic uncertainties for the cocktail simulation. 75

3.34 Systematic uncertainties from different sources in Au+Au at 200 GeV. . . 76

4.1 The comparison for di-electron continuum between data and simulation after efficiency correction within the STAR acceptance in 200 GeV minimum-bias p+p collisions. The di-electron continuum from simulations with different source contributions are also shown. The statistical errors are shown as bars. The systematic uncertainties are shown as boxes. The 14% normalization uncertainty on data is not shown. The band on top of the curve illustrates the systematic uncertainties on cocktail. 78

4.2 $e^+e^-$of charm components from PYTHIA simulation fit to the data shown as red line. Red triangles show the fit data points which are dominant by charm contributions. The fit of random e^+e^-pair is estimated to be the systematic uncertainty. 79

4.3 Left: The simulations scaled with a charm cross section number compared to the corresponding measurements in p+p collisions. Right: χ^2 between simulation and measurement as a function of input charm cross section. . . 80

4.4 Left: The M_{ee} distribution after the mixed-event background subtraction at $0.95 < M_{ee} < 1.08$ GeV/c^2 in p+p collisions at $\sqrt{s} = 200$ GeV. The curve represents the fit in the range of $0.98 < M_{ee} < 1.04$ GeV/c^2. Errors on data points are statistical. Right: The M_{ee} distribution after the mixed-event background subtraction at $2.85 < M_{ee} < 3.30$ GeV/c^2 in p+p collisions at $\sqrt{s} = 200$ GeV. The curve represents the fit in the range of $3 < M_{ee} < 3.16$ GeV/c^2. Errors on data points are statistical. 82

4.5 m_{ee} distribution for di-electron production in p+p collisions at $\sqrt{s} = 200$ GeV. The dashed curve is the cocktail with the $\eta \to e^+e^-$ decay channel included in the fit. The dot-dashed peak is the $\eta \to e^+e^-$ contribution with the upper limit of its branching ratio from the PDG [BB08], which is 2.7×10^{-5}. The best fit is shown as the solid curve. 83

4.6 The M_{ee} distribution for three different p_T bins after the mixed-event background subtraction at $0.65 < M_{ee} < 0.95$ GeV/c^2 in p+p collisions at $\sqrt{s} = 200$ GeV. The curves represent fits in the range of $0.7 < M_{ee} < 0.85$ GeV/c^2. Errors on data points are statistical. 84

4.7 The M_{ee} distribution for six p_T bins from 0-3 GeV/c after the mixed-event background subtraction at $0.65 < M_{ee} < 0.95$ GeV/c^2 in Au+Au collisions at $\sqrt{s} = 200$ GeV. The curves represent fits in the range of $0.73 < M_{ee} < 0.82$ GeV/c^2. Errors on data points are statistical. 85

4.8 The efficiency including STAR acceptance for $\omega \to e^+e^-$ at $|y| < 1$. Left is for p+p collisions, right is for Au+Au collisions. 86

4.9 The $\omega \rightarrow e^+e^-$ invariant yield, divided by its B.R.. Star symbols are the yields in non-singly diffractive p+p collisions at $\sqrt{s}$ = 200 GeV. Red squares are the yields in Au+Au minimum bias collisions. The circles represent PHENIX published results [Ada11]. The bars are statistical errors and boxes are systematic uncertainties. The lines represent predictions of Tsallis blast-wave function by fitting other measurements in p+p and Au+Au. 87

4.10 Comparison for di-electron continuum between data and simulation after efficiency correction within STAR acceptance in minimum bias Au+Au collisions at $\sqrt{s_{\rm NN}}$=200 GeV. The di-electron continuum from simulation includes light hadron and correlated decays of charm, bottom and Drell-Yan. The charm contribution is generated from PYTHIA and scaled by the number of binary collisions. Statistical errors are shown as bars. The systematic uncertainties are shown as boxes. The bottom panel shows the ratio of data to cocktail. 89

4.11 The di-electron cocktail within PHENIX acceptance compared to PHENIX cocktail in minimum bias Au+Au collisions at $\sqrt{s_{\rm NN}}$=200 GeV. Blue solid line is the reproduced cocktail within PHENIX acceptance. Green dotted dashed line is PHENIX cocktail in the [Ada10]. Statistical errors are shown as bars. Red solid line is charm contribution scaled by PHENIX charm cross section. Magenta dotted dashed line is the charm contribution by PHENIX PYTHIA simulation in the [Ada10]. 90

4.12 Comparison for di-electron continuum between STAR and PHENIX in minimum bias Au+Au collisions at $\sqrt{s_{\rm NN}}$=200 GeV. Blue dots represent the STAR di-electron continuum scaled by the acceptance difference between STAR and PHENIX. Open circles show the PHENIX data. Statistical errors are shown as bars. Band is the PHENIX data systematic uncertainties. 91

5.1 The expected electron-muon correlation from charm pair production and from background of random combination in d+Au collisions. The statistics of simulation are equivalent to 2 billion minimum bias d+Au collisions. Figure is taken from [Rua09]. 93

List of Tables

2.1 Performance specifications of RHIC 21

2.2 Parameters of the TPC inner and outer subsectors. 27

2.3 TOF system performance in different runs. 39

3.1 Centrality classes and corresponding $< N_{part} > < N_{coll} > < b >$ in Au+Au collisions at $\sqrt{s_{\rm NN}}$=200 GeV. 45

3.2 The numbers of events after vertex cuts in p+p and Au+Au collisions. . . 45

3.3 Cuts of electron identification 47

3.4 The parameterized electro-magnetic transition form factor Λ of hadrons. . 68

3.5 Hadron non-single diffractive cross section 68

3.6 Hadron cross section 69

3.7 Systematic uncertainties from different sources for di-electron continuum. . 76

CHAPTER 1

Physics

1.1 Quantum Chromodynamics

In the 1950s, particle physicists discovered a large number of particles called hadrons with the bubble chambers and spark chambers. To understand fundamental particles of the hadrons, Gell-Mann and George Zweig explained the hadrons could been sorted into groups having similar properties and masses by the existence of three flavours of smaller particles inside the hadrons: the quarks. But some of the hadron composed with three identical quarks with parallel spin, such as Ω^-, is forbidden by the Pauli exclusion principle. In 1965, Greenberg resolved the problem by proposing an additional SU(3) gauge degree of freedom of quarks called color charge. Moo-Young Han and Nambu realized the interaction between quarks might be via an octet of vector gauge bosons called gluons. In 1972, Gell-Man and Fritzsch introduced the Quantum Chromodynamics to describe the strong interaction between the colored quarks and gluons [FG72]. Now QCD is part of the Standard Model that describes the strong and electroweak forces. QCD is a renormalizable nonabelian gauge field theory based on the gauge group $SU(3)_C$, with gauge bosons - color octet gluons for factors and a unique group coupling constant g_s. The QCD Lagrangian can be written as:

$$\mathcal{L}_{QCD} = -\frac{1}{4}F^{(a)}_{\mu\nu}F^{(a)\mu\nu} + i\sum_q \bar{\psi}^i_q \gamma^\mu (D_\mu)_{ij}\psi^j_q - \sum_q m_q \bar{\psi}^i_q \psi^i_q, \tag{1.1}$$

$$F^{(a)\mu\nu} = \partial A^a_\nu - \partial A^a_\mu - g_s f_{abc} A^b_\mu A^c_\nu, \tag{1.2}$$

$$(D_\mu)_{ij} = \delta_{ij}\partial_\mu + ig_s \sum_a \frac{\lambda^a_{ij}}{2} A^a_\mu, \tag{1.3}$$

where g_s is the QCD coupling constant, and the f_{abc} are the structure constants of the $SU(3)_C$ algebra. γ^μ are the Dirac matrices and $\psi^i_q(x)$ are the 4-component Dirac spinors associated with each quark field of color i and flavor q. The field strength tensor $F^{(a)\mu\nu}$ describes the interaction between gluons. $(D_\mu)_{ij}$ is the covariant derivative with the Gell-Mann matrices λ^i and the Yang-Mills (gluon) fields $A^a_\mu(x)$.

QCD shows two peculiar properties of the strong interaction: 1) asymptotic freedom; 2) confinement.

1.1.1 Asymptotic freedom

The effective QCD coupling $\alpha_s(\mu)$ shows a dependence on the renormalization scale, similar to that in QED(running coupling). The coupling can be expressed as:

$$\alpha_s(\mu) \equiv \frac{g_s^2(\mu)}{4\pi} \approx \frac{4\pi}{\beta_0 \ln(\mu^2/\Lambda^2_{QCD})}, \tag{1.4}$$

Where β_0 is a constant and has a dependence on the number of quarks with mass less than the energy scale μ. With $\beta_0 > 0$ and increasing momentum transfer, the coupling decreases and the solution illustrates the asymptotic freedom [GW73b, Pol73, GW73a, HP74]. QCD can be calculated by perturbative method in high momentum transfer or short distance approach. On the other hand, when the $\mu \sim \Lambda_{QCD}$ QCD becomes strongly coupled. The perturbative QCD breaks down in this case. α_s is determined from experiment, the world averaged α_s at the fixed-reference $\mu_0 = M_z$ is: $\alpha_s(M_z) = 0.1184 \pm 0.0007$ [Bet09], and the QCD scale $\Lambda_{QCD} \approx 200$ MeV. Fig. 1.1 provides the measurements and the prediction by QCD of the scale dependence of the strong coupling.

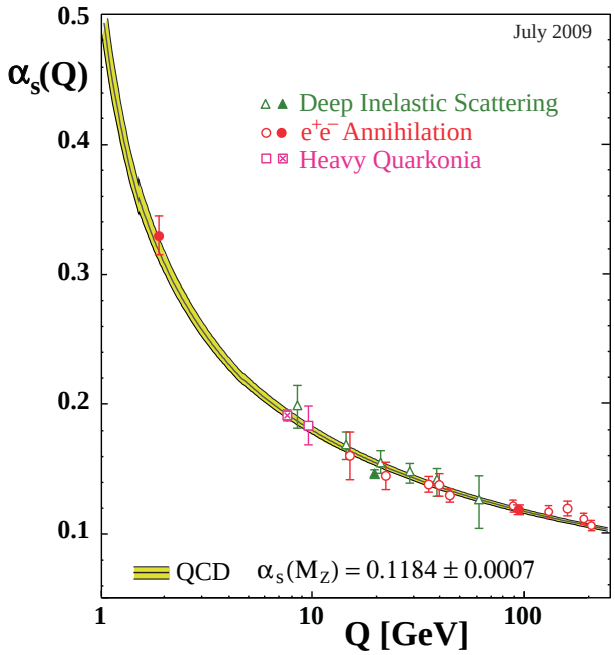

Figure 1.1: Summary of measurements of α_s as a function of the respective energy scale Q. The figure is taken from [Bet09].

1.1.2 Deconfinement and phase diagram

One of the most mysterious and unexplained physics phenomenon in QCD is color confinement. QCD has no analytic deviation that claim the quarks and gluons should be confining. Experimentally, the isolated quarks and gluons have never been observed, they cannot be isolated singularly from hadrons. But intuitively the confinement is due to force-carrying gluons having color charge. The interaction between quarks and gluons must be strong on large distance scale due to the property of asymptotic freedom. When two quarks have large enough energies and become separated, at same point it is more energetically favorable for a new quark/anti-quark pair to spontaneously appear out of the vacuum, than to allow the quark to separate further. As a result of this, when quarks are produced at high energy, instead of seeing the individual quarks, many color-neutral particles clustered together are observed, called *jet*. The process is called hadronization.

On the other side, when the partons are at high energies or at high density, the quarks and gluons are able to move over larger distances that of the size of a nucleon ($\approx 1fm$) and hence forming the quark-gluon plasma (QGP). This phenomenon is called deconfinement.

At such extreme conditions of high energies or high baryon density, the quarks and gluons are deconfined from hadrons. Lattice QCD predicted a phase transition from normal QCD matter to the new matter QGP, with new color degrees of freedom. The phase transition temperature as prediction is 154 ± 8 MeV [KLP01]. Fig. 1.2 shows the schematic phase diagram of hadronic matter. From Lattice QCD prediction, there is a boundary in the phase diagram which separates the region of matter dominated by hadronic degrees of freedom from that dominated by quark-gluonic degrees of freedom. The boundary is called "first order phase transition" line or "QGP phase boundary". The point in the figure is called "critical point". Lattice QCD predicts the first order phase transition ends at the critical point, and when the μ_B close to 0, the explicit phase transition will not be real, and it becomes rapid crossover. The dotted line represents the crossover. One of the main aim of high-energy heavy-ion collision experiments is to explore the QCD phase diagram, to locate the position of critical point, and to determine the QCD phase boundary. To explore the QCD phase diagram and study the deconfined QGP matter, the Relativistic Heavy Ion Collider (RHIC) at Brookhaven National Laboratory (BNL) is designed for head-on Au+Au collisions at $\sqrt{s_{\rm NN}}$=200 GeV.

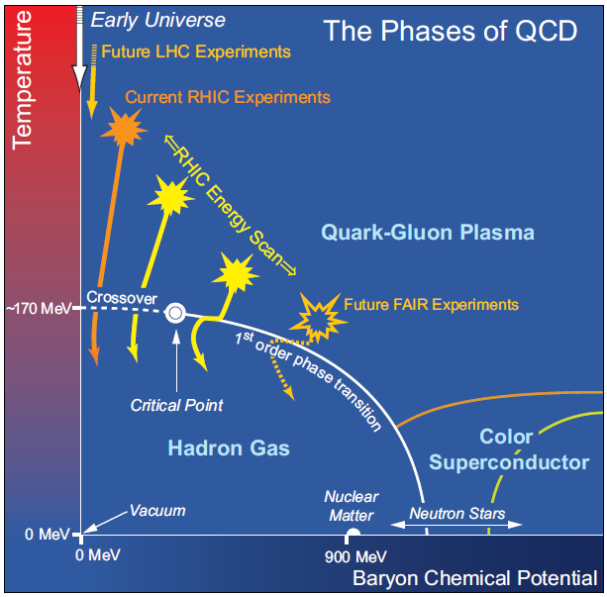

Figure 1.2: Schematic picture of the QCD phase diagram shown in $T \approx \mu_B$ space [USA07].

1.1.3 Chiral symmetry

From the Lagrangian density given by Eq. 1.1, the Lagrangian possesses local *SU(3)* color gauge symmetry. In addition, $\mathcal{L}_{QCD}$ exhibits several global symmetries. The most relevant one is *U(1)* Symmetry entailing the baryon number conservation. Lagrangian has additional symmetries in the limit of vanishing quark mass. The momentum transfers of $q \simeq 1$ GeV/c is a good approximation for the up- and down-quark and to a lesser extent in the strange quark. The Lagrangian is invariant under global vector and axial vector transformations in *SU(3)* flavor space:

$$\psi \rightarrow e^{-i\alpha_V^i \frac{\lambda^i}{2}}\psi \;\; and \;\; \psi \rightarrow e^{-i\alpha_A^i \frac{\lambda^i}{2}}\gamma_5\psi. \tag{1.5}$$

The associated conserved Noether currents of these symmetries are

$$j^\mu_{V,i} = \bar{\psi}\gamma^\mu \frac{\lambda^i}{2}\psi \;\; and \;\; j^\mu_{A,i} = \bar{\psi}\gamma^\mu \frac{\lambda^i}{2}\gamma^5\psi. \tag{1.6}$$

The corresponding charges will become

$$\mathcal{Q}_i^V = \int d^3x\psi^+ \frac{\lambda_i}{2}\psi, \quad \mathcal{Q}_i^A = \int d^3x\psi^+ \frac{\lambda_i}{2}\gamma_5\psi \tag{1.7}$$

commute with the Hamiltonian of QCD, $[\mathcal{Q}_i^{V,A}, H_{QCD}] = 0$.

The quark fields can be decomposed into left and right chirality components, $\psi_{L,R} = \frac{1}{2}(1 \mp \gamma_5)\psi$, the Lagrangian form will become

$$\mathcal{L}_{QCD} = \bar{\psi}_L i\gamma^\mu D_\mu \psi_R + \overline{\psi}_R i\gamma^\mu D_\mu \psi_R - \frac{1}{4}G^a_{\mu\nu}G^{\mu\nu}_a - (\overline{\psi}_L \mathcal{M}^\circ \psi_R + \overline{\psi}_R \mathcal{M}^\circ \psi_L) \tag{1.8}$$

and the transforms Eq. 1.5 translate to

$$\psi_L \rightarrow e^{-i\alpha_L^i \frac{\lambda^i}{2}}\psi_L \;\; and \;\; \psi_R \rightarrow \psi_R \tag{1.9}$$

$$\psi_R \to e^{-i\alpha_R^i \frac{\lambda^i}{2}} \psi_R \quad and \quad \psi_L \to \psi_L, \tag{1.10}$$

which constitutes a global $SU(3)_L \times SU(3)_R$ chiral symmetry in flavor space for small quark masses. $\mathcal{M}^0$ is the diagonal matrix of current quark mass as parameters of the Standard Model (SM). Chiral invariance of the QCD Lagrangian refers to the conservation of quark handed-ness and isospin. Left and right handed quarks do not mixed dynamically in strong interactions. As a consequence, the associated conserved charges

$$\mathcal{Q}_i^L = \int d^3x \psi_L^+ \frac{\lambda_i}{2} \psi_L = \frac{1}{2}(\mathcal{Q}_i^V - \mathcal{Q}_i^A) \tag{1.11}$$

$$\mathcal{Q}_i^R = \int d^3x \psi_R^+ \frac{\lambda_i}{2} \psi_R = \frac{1}{2}(\mathcal{Q}_i^V + \mathcal{Q}_i^A) \tag{1.12}$$

again commute with the QCD Hamiltonian.

So the Lagrangian of QCD contains a symmetry in the limit of vanishing quark masses. Apply the global $U_A(1)$ transformations (axial term),

$$\psi \to e^{-i\alpha\gamma_5} \psi, \tag{1.13}$$

the Lagrangian is implying a conserved Noether current shown as the form

$$j_{A,0}^\mu = \overline{\psi} \gamma^\mu \gamma_5 \psi \tag{1.14}$$

The divergence of $j_{A,0}^\mu$ thus has an anomaly which called the $U(1)_A$ axial anomaly, has the form

$$\partial_\mu j_{A,0}^\mu \equiv \frac{3}{8} \alpha_s G_{\mu\nu}^a \hat{G}_a^{\mu\nu}, \hat{G}_{\mu\nu}^a \equiv \epsilon^{\mu\nu\alpha\beta} G_{\alpha\beta}^a, \tag{1.15}$$

So the final QCD Lagrangian is symmetric only under the group

$$SU(3)_L \times SU(3)_R \times U(1)_V. \tag{1.16}$$

It means the baryonic conservation relate to the vector and axialvector currents.

Spontaneous Breaking of Chiral Symmetry In the quantum field theory, spontaneously broken symmetry plays a major role in the applications of QCD and also find applications in the theory of the strong interactions. For the chiral symmetry, because the chiral partners, *e.g.*, the ρ and a_1 mesons have a mass difference of $\simeq 550$ MeV$/c^2$ [Ams08], this observation of the mass splitting indicates a spontaneous breaking of chiral symmetry. It is because the vacuum expectation value of the quark condensate $\langle\overline{\psi}\psi\rangle \neq 0$. In consequence of this non-vanishing value, the vector current $j_V = j_L + j_R$ is still conserved while the axial vector symmetry ($j_A = j_L - j_R$) is spontaneously broken. The axial-vector charge $\mathcal{Q}_i^A$ in Eq. 1.7 is still commutes with the QCD Hamiltonian, but the ground state $\mathcal{Q}_0^A|0\rangle \neq 0$. According to the Goldstone theorem [JG61], the chiral symmetry is spontaneously broken when the ground state is chosen, and results in the existence of eight massless Goldstone bosons ($\pi^{\pm}, \pi^0, K^{\pm}, K^0, \overline{K^0}, and\ \eta$).

For a simple example, consider a scalar self-interacting real field Lagrangian,

$$\mathcal{L} = \frac{1}{2}\partial_\mu\phi\partial^\mu\phi - V(\phi), \tag{1.17}$$

with following potential

$$V(\phi) = \frac{1}{2}\mu^2\phi^2 + \frac{1}{4}\lambda\phi^4. \tag{1.18}$$

The Lagrangian is invariant under the transformation

$$\phi \rightarrow -\phi. \tag{1.19}$$

The vacuum (ϕ_0) can be obtained from the Hamiltonian

$$\mathcal{H} = \frac{1}{2}[(\partial_0\phi)^2 + (\nabla\phi)^2] + V(\phi). \tag{1.20}$$

We can see that $\phi_0 = constant$ corresponds to the ground state of $V(\phi)$ where

$$\phi_0(\mu^2 + \lambda\phi_0^2) = 0. \tag{1.21}$$

To ensure the $\mathcal{H}$ is bounded, the λ should be positive. The sign of μ determined the minimum of the $V(\phi)$, for $\mu^2 > 0$, there is just one vacuum at $\phi_0 = 0$ and it is invariant under Eq. 1.19 (see Fig. 1.3(a)). However, for $\mu^2 < 0$, the state $\phi_0 = 0$ is a local maximum and therefore unstable. The ground state become two vacua states $\phi_0^{\pm} = \pm\sqrt{-\mu^2/\lambda}$ (Fig. 1.3(b)). The choice of one ground state between ϕ_0^+ or ϕ_0^- does not effect the invariance of the Lagrangian under transformation Eq. 1.19. Nevertheless, once one choice is made the symmetry is spontaneously broken since $\mathcal{L}$ is invariant but vacuum is not. If a continuous symmetry is spontaneously broken, with the identification of the fields $\phi^*\phi$ around the symmetry axis, *i.e.*, axial-vector rotations, correspond to the massless Goldstone bosons. In contract, radial excitations correspond to massive particles. Therefore it contains one massless scalar particle for each broken generator of the original symmetry group.

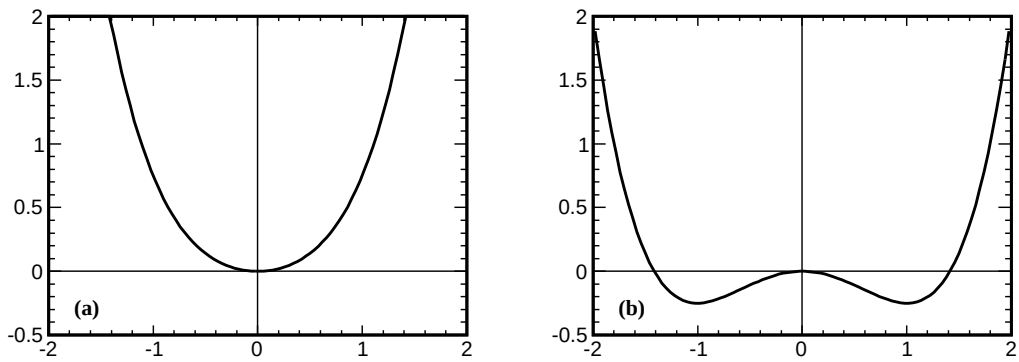

Figure 1.3: Scalar potential Eq. 1.18 for $\mu^2 > 0$ (a) and for $\mu^2 < 0$ (b).

As a further consequence of chiral symmetry breaking, the axial current matrix element between the vacuum and a Goldstone boson is nonvanishing. The finite quark masses lead to a contribution for the quark condensate

$$\langle\overline{\psi}\psi\rangle \equiv \langle 0|\overline{\psi}_L\psi_R + \overline{\psi}_R\psi_L|0\rangle, \tag{1.22}$$

in the Lagrangian of Eq. 1.1, which exhibits the explicit mixing of left- and right-handed quarks in the QCD vacuum. For pions, one has the vacuum expectation value of such

Goldstone bosons which is:

$$\langle 0|j^{\mu}_{A,k}(x)|\pi_j(p)\rangle = i\delta_{jk} f_\pi p^\mu e^{-ipx}. \tag{1.23}$$

The pion decay constant $f_\pi = 93$ MeV is an order parameters which measures the strength of the symmetry breaking. The vacuum expectation value or quark condensate Eq. 1.22 is a second order parameter. The order parameters f_π and $\langle\overline{\psi}\psi\rangle$ are related. They can be expressed as the Gell-Mann-Oakes-Renner relation (GOR) [GOR68]

$$m_\pi^2 f_\pi^2 = -2\overline{m}\langle\overline{q}q\rangle, \tag{1.24}$$

where $\overline{m} = \frac{1}{2}(m_u + m_d)$ and $\langle\overline{q}q\rangle = \langle\overline{u}u\rangle = \langle\overline{d}d\rangle$. Taking $\overline{m} = 6$ MeV yields the vacuum value for the quark condensate, $\langle\overline{q}q\rangle = -(240\ MeV)^3 = -1.8\ fm^{-3}$.

In-Medium Condensates and Chiral Restoration In the ultra-relativistic heavy-ion collisions, it is to be expected that the quark and gluon condensates are modified in a hot and dense medium created in the collisions. From the schematic view of the QCD phase diagram Fig. 1.2. It is expected that hadronic matter go through a phase transition at high temperature and pressure. The quarks condensates are melted in the medium, and before reaching the deconfinement stage, chiral symmetry is partially restored.

To discuss the modifications, we start from a given system of 3-volume V with finite temperature, T and quark chemical potential, μ_q in contact with a heat bath which is specified by the grand canonical partition function

$$\mathcal{Z}(V, T, \mu_q) = Tr\{e^{-(\hat{H}-\mu_q\hat{N})/T}\}, \tag{1.25}$$

where $\hat{H}$ is the Hamiltonian of the system and $\hat{N}$ is the quark number operator.

The expectation value of the quark condensates can be given by

$$\langle\langle\bar{\psi}\psi\rangle\rangle = \mathcal{Z}^{-1}\sum_n \langle n|\bar{\psi}\psi|n\rangle e^{-(E_n-\mu_q)/T}, \tag{1.26}$$

where the sum extends over a complete set of eigenstates of H and E_n. The $|n\rangle$ and E_n are the QCD eigenstates and energies, respectively. Considering a non-interacting pion gas, the leading order result to the vacuum condensate $\langle\overline{\psi}\psi\rangle$ is therefore given by the matrix element $\langle\pi|\overline{\psi}\psi|\pi\rangle$, and the leading order result to Eq. 1.26 with respect to the vacuum expectation value ratio becomes

$$\frac{\langle\langle\overline{\psi}\psi\rangle\rangle}{\langle\overline{\psi}\psi\rangle} \simeq 1 - \frac{\sum_\pi \rho_\pi^s(T)}{f_\pi^2 m_\pi^2} \tag{1.27}$$

where $\sum_\pi$ denotes the pion σ-term and ρ_π^s the pion scalar density at given temperature. For the case of finite baryon density and vanishing temperature, the result is a linear decrease with density

$$\frac{\langle\langle\overline{\psi}\psi\rangle\rangle}{\langle\overline{\psi}\psi\rangle} \simeq 1 - \frac{\sum_N \rho_N^s(\mu_N)}{f_\pi^2 m_\pi^2} \tag{1.28}$$

where $\sum_N$ is the nucleon σ-term and ρ_N^s the nucleon scalar density at given μ_q ($\mu_N = 3\mu_q$). At nuclear saturation densities ($\rho_0 = 0.16 fm^{-3}$) the quark condensate has dropped by 30% with a experimentally determined nucleon σ-term of $\sigma_N \approx 45$ MeV [RW00]. Based on these calculations, the expected scalar quark condensate as function of temperature and density can be derived, which is displayed in Fig. 1.4.

Chiral meson Lagrangians should be scale invariant on the classical level for dimension 4. From the derivation of Brown and Rho [BR91], the effective Lagrangian has appropriate scaling behavior of the QCD Lagragian. They predict that the quark and gluon condensates change in dense matter, and the meson masses will decrease when the quark condensates are proposed. The change in the quark condensate at a given density can be expressed as

$$\frac{\langle\langle\overline{\psi}\psi\rangle\rangle}{\langle\overline{\psi}\psi\rangle} = (\frac{\chi^*}{\tilde{\chi}_0})^3, \tag{1.29}$$

where $\tilde{\chi}_0$ denotes the vacuum expectation value of the χ^* field. So an in-medium pion decay constant can be defined as

$$f_\pi^* = f_\pi \frac{\chi^*}{\tilde{\chi}_0}. \tag{1.30}$$

As a result of the derivation [BR91], a universal Brown-Rho (BR) scaling relation of the

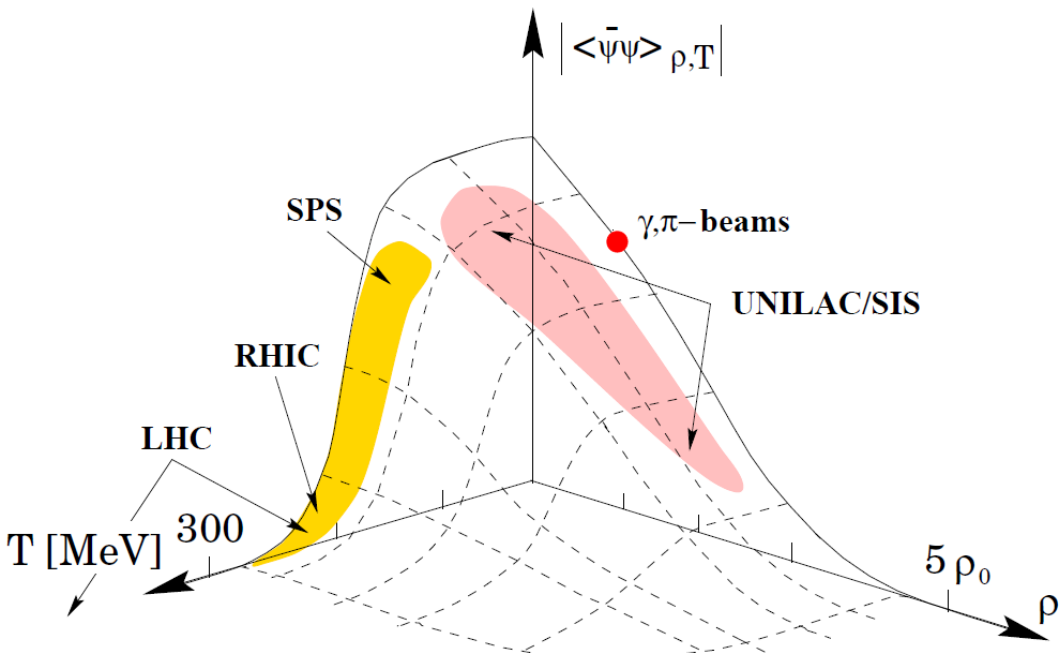

Figure 1.4: The expectation value of the quark condensate. Calculation is based on the Nambu-Jona-Lasinio model [KLW90]. Figure is from [Her01].

in-medium vector meson masses can be expressed as

$$\Phi(\rho) \equiv \frac{f_\pi^*}{f_\pi} = \frac{m_\sigma^*}{m_\sigma} = \frac{m_N^*}{m_N} = \frac{m_\rho^*}{m_\rho} = \frac{m_\omega^*}{m_\omega}. \tag{1.31}$$

The typical values for $\Phi(\rho_0) = 0.82 \pm 0.06$ at normal nuclear matter density, indicates a dropping of the ρ mass by 15-20%. More details of other relative models of medium modification of vector mesons can be found in Ref. [RW00].

1.2 Di-leptons

In the ultra-relativistic heavy ion collisions, the study of di-lepton was one of probes to map out the behavior of the hot and dense matter created in the collision. Being produced at all stages of the collision and suffering minimal final-state interaction, di-leptons convey a variety of information about the high density and high temperature matter and become a unique tool to study the properties of QGP.

Fig. 1.5 shows the schematic di-lepton mass spectrum in ultra-relativistic heavy ion col-

lisions includes the major sources, they consist of Drell-Yan process, hadron gas/resonanses, heavy flavor hadron contribution, and QGP thermal radiation *etc.*. The contributions of those sources dedicate to different di-lepton invariant mass region due to their production mechanism.

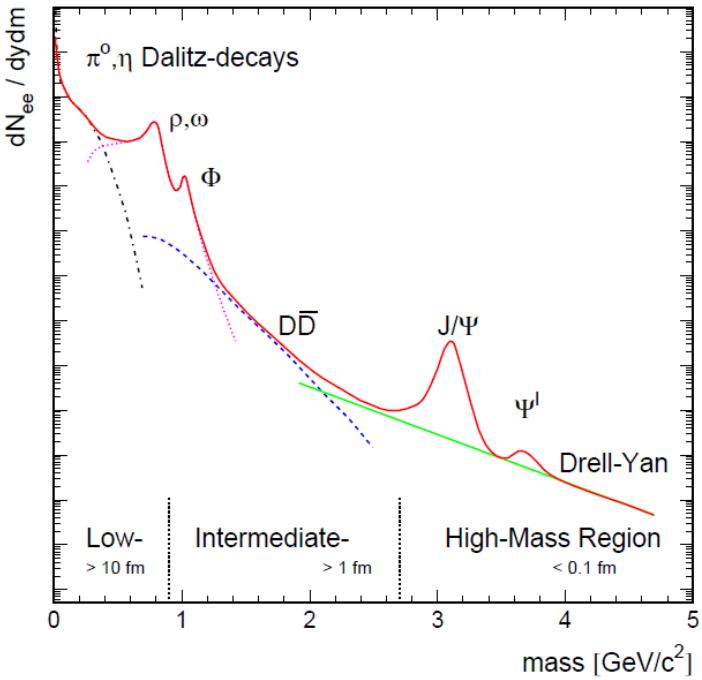

Figure 1.5: Schematic di-lepton mass distribution of ultra-relativistic heavy ion collisions.Figure is from [Her01].

In the high mass region ($m_{ll} > 3$ GeV/c^2), di-leptons stem from hard processes (mostly Drell-Yan annihilation and heavy quarkonia). Drell-Yan process is the annihilation of a quark in one nucleus with an antiquark of another nucleus, creating a virtual photon or Z boson which then converts into a pair of leptons. This process is occurring in the early pre-equilibrium stage of the collision, it can be described by a Feynman diagram shown in Fig. 1.6. The heavy quarkonium contributions are from J/ψ and ψ'. Comparing to the J/ψ, the charmed hadron contribution are small in this mass region. But at intermediate mass region, it is a dominant source.

In the intermediate mass region ($1.1 < m_{ll} < 3$ GeV/c^2), the di-leptons are dominated by the semi-leptonic decays of charm, bottom hadrons and the QGP thermal radiations. Charm and bottom quarks are produced in the inelastic hard scattering processes between

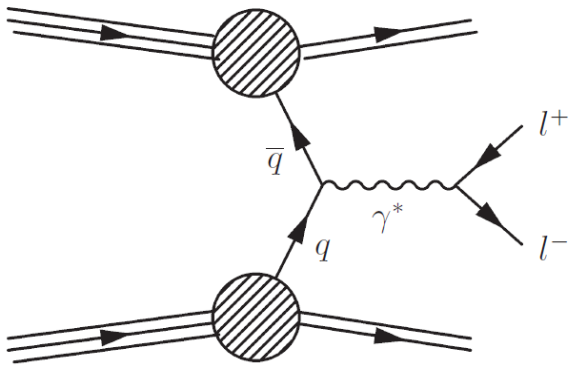

Figure 1.6: Feynman diagram for Drell-Yan process .

two constituent quarks ($q\overline{q} \rightarrow g^* \rightarrow Q\overline{Q}$, here $Q\overline{Q} = c\bar{c}$ or $b\bar{b}$, respectively). Then the open charm and bottom mesons are formed out of a heavy flavor quark (c or b) and a light quark (u, d or s). After a weak decay process, they produce single leptons, *e.g.*, $D^+ \rightarrow \bar{K^0} l^+ \nu_l$. Therefore, the decays of both D^+ and D^- form a di-lepton pair. If there is no enhancement of open-charm production, a thermal signal from the QGP is expected to be revealed in this mass region [Shu78, MT85]. The thermal di-lepton is considered to bring the information of temperature and radial flow of the equilibrium thermalized partonic matter.

The low mass region is dominated by the soft process involving the light quark sector. The di-lepton continuum come from Dalitz decays of neutral mesons such as $\pi^0, \eta, \eta' \rightarrow \gamma l^+ l^-$ and $\omega \rightarrow \pi^0 l^+ l^-$. The two body decays of resonance, for example $\rho, \omega, \phi \rightarrow l^+ l^-$, compose the peaks. This region is particularly sensitive to the in-medium modification of vector mesons which is possible relative to the chiral symmetry restoration. The di-lepton production is mediated by the ρ meson which has broad width (149 MeV [Nak10]) in the hadronic matter. Due to the short life time of only 1.3 fm/c and strong coupling to the $\pi\pi$ channel, the di-lepton signals from ρ undergo a significant modification in medium. The signature can directly be interpreted as the space-time averaged spectral function. QGP thermal radiation in this mass range are not significant. For detail theoretical calculations of thermal di-lepton at SPS and RHIC energies see, *e.g.*, Ref. [Rap01].

1.3 Exotic decay

Rare processes like leptonic decays of hadrons provide possible observables in searching for traces of new physics beyond the Standard Model (BSM) [Dor10, BES09, SLW92, BSS88]. These decays usually involve electromagnetic or weak couplings which can be calculated to high accuracy. In addition to a direct observation of the Higgs boson, the Large Hadron Collider (LHC) looks to explore BSM physics. Precision measurements at low energy target deviations of observables from the SM prediction as indirect evidence of coupling from BSM physics to the rare process [Dor10]. The pseudoscalar mesons (for example, η or η') are particularly interesting since their decay to e^+e^- pairs is suppressed by $\alpha^2(10^{-4})$ and helicity conservation due to the small electron mass ($r^2 = (m_e/m_P)^2 \simeq 10^{-6}$). The branching ratio (B.R.) of $\eta \rightarrow e^+e^-$ can be predicted in SM with good precision, which is 2.3×10^{-9}. Couplings from BSM physics can increase this B.R. significantly [Dor10]. RHIC provides a unique opportunity to search for BSM physics with rare decays of hadrons. The high luminosity and high multiplicity in nucleus-nucleus collisions produce copious hadrons of interest for the rare decay process. With recent upgrades to the detector [Sha06a], including the data acquisition system [Lan03], the STAR Collaboration is able to benefit from high rate capability as well as excellent lepton identification at low momentum in the search for rare decays from the copiously produced hadrons.

1.4 Previous experimental results

There are several measurements on the di-lepton continuum in heavy ion collisions at a variety of energies. The most relevant measurements to this analysis are the measurement of the dimuon continuum by the NA60 collaboration at SPS and the di-electron continuum measurement from PHENIX at RHIC. In this section, the results from two experiments will be briefly discussed.

1.4.1 NA60

The NA60 experiment has been proposed to study the deconfined partonic matter at SPS heavy ion collisions. The detector implements the muon spectrometer and zero degree calorimeter used in NA50 [Abr97] with two state-of-the-art silicon detectors. Benefit from the new detectors, NA60 has the ability to identify the distance between collision vertex and the muon tracks. The dimuon contribution from charmed hadron can be distinguished from the prompt $\mu^+\mu^-$ pairs [Sha07b].

One of their results, the centrality-integrated net dimuon mass spectrum for 158A GeV In-In collisions in the LMR region is shown in the left panel of Fig. 1.7. All sources of hadron decays except ρ decays are included, excess dimuons are isolated from the known sources. The excess dimuons can be illustrated by the modified ρ contributions, which is shown in the right panel of Fig. 1.7. Two main theoretical scenarios for the in-medium spectral properties of the ρ. An in-medium broadened spectral function [RW00] and the dropping mass scenario [BR02], were used for the comparison. The broadening describes the data well.

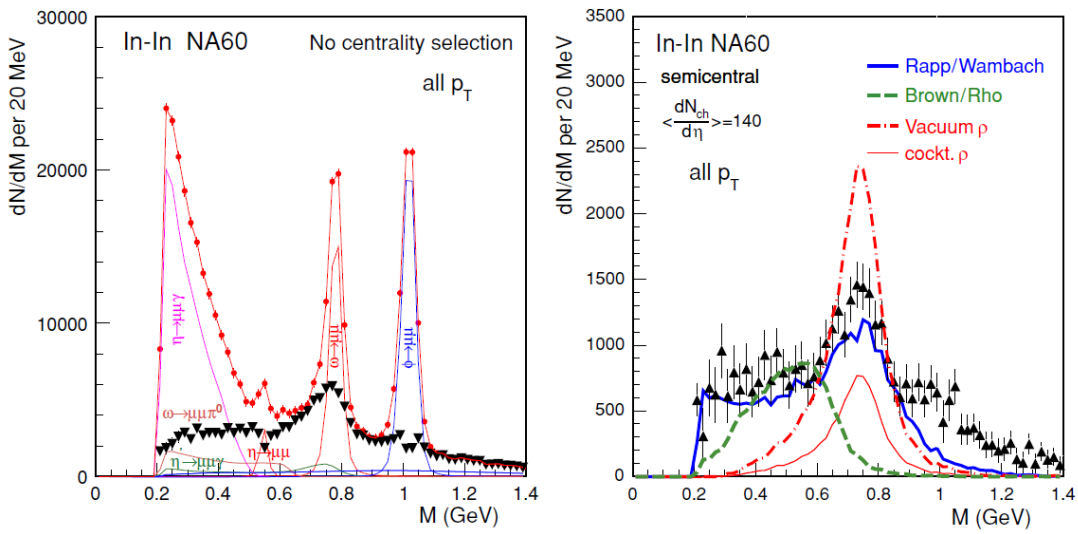

Figure 1.7: Left panel:Di-muon invariant mass spectrum before(dots) and after subtraction of the known decay sources(triangle). Right panel: Comparison between excess dimuons and theoretical predictions [Rap02]. Figure is from [Dam08].

Another result is mass spectrum in the IMR region, which is shown in Fig. 1.8. NA60

the measured offset between the muon tracks and the main event vertex to disentangle prompt and offset dimuons from D decays. Left panel shows the weighted offset distribution of dimuons. The weight in the dimuons offset from the vertex considers the momentum dependent resolution of the vertex measurement of a muon. The weighted offset distribution can be perfectly described by the upscaling NA50 measurements in the IMR in p-A collisions [Arn09a]. It indicates there is no charm enhancement. Right panel shows the excess dimuons compared to the Drell-Yan, open charm decays shapes. The shape of excess at IMR region is quite similar to the open charm decays.

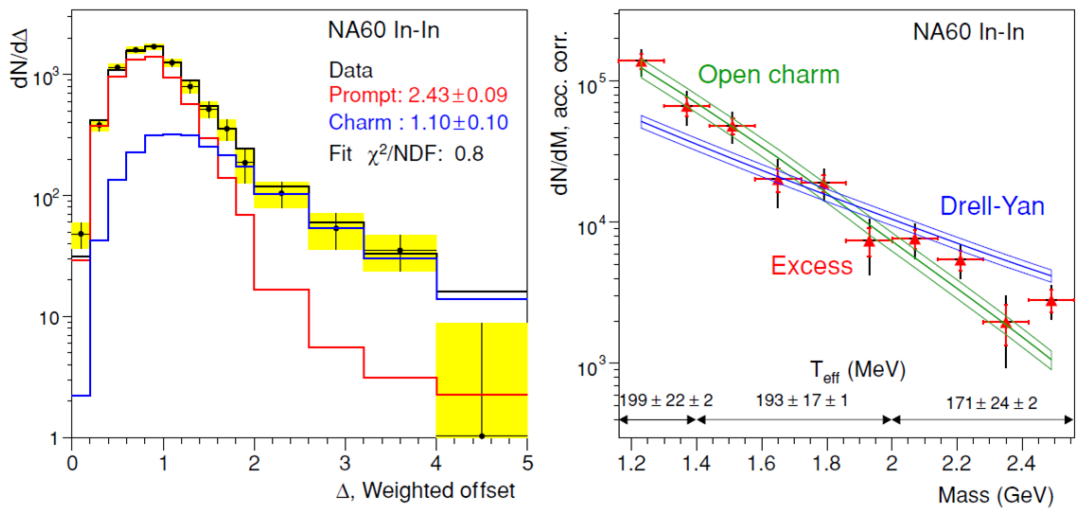

Figure 1.8: Left panel: a fit of the weighted offset distribution of $\mu^+\mu^-$ pairs to prompt and charm decays in the IMR region. Right Panle: acceptance corrected excess yield compared to Drell-Yan, open charm decays. Figure is from [Dam08].

The last result from NA60 discussed here is the slope parameter T_{eff} of m_T-spectra distribution as a function of dimuon mass, which is shown in Fig. 1.9. The T_{eff} follows the trend of a hadronic source with radial flow at $M < 1$ GeV/c^2. The sudden decline for $M > 1$ GeV/c^2 may suggest a dominant partonic emission source in this region.

1.4.2 PHENIX

The PHENIX collaboration at Relativistic Heavy Ion Collider (RHIC) has measured the e^+e^-continuum in $\sqrt{s_{\rm NN}}$= 200 GeV Au+Au and p+p collisions [Ada10], which shows an excess above the expected yield from known sources at LMR. The results is shown

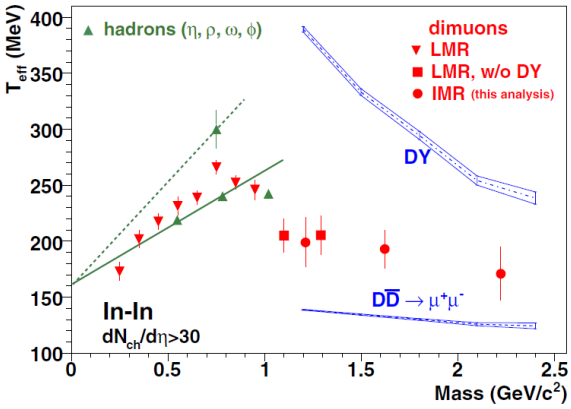

Figure 1.9: T_{eff} of the excess m_T-spectra vs. $\mu^+\mu^-$ pair mass. Figure is from [Arn08].

in Fig. 1.10. Left panel shows the e^+e^-mass spectrum in p+p collisions, and the result in Au+Au minimum bias is shown in right panel. The e^+e^-continuum in Au+Au is compared to expectations from the decays of light hadrons and correlated decays of charm, bottom, and Drell-Yan. An excess is observed at mass range between 0.15-0.75 GeV/c^2. The enhanced factor of the excess compared to expectation yield is measured to be $4.7 \pm 0.4(stat.) \pm 1.5(sys.)$ [Ada10] in the mass 0.15-0.75 GeV/c^2.

Fig. 1.11 shows the comparison of di-electron continuum in the LMR to the theory calculations. Panel (b) shows the calculation from Rapp and van Hees. The calculation has an electro-magnetic spectral function constrained by e^+e^- annihilation data. The spectral function is characterized by the light vector resonances according to the vector-meson dominance model (VDM) and a perturbative quark-antiquark continuum. Panel (c) shows the calculation from Dusling and Zahed. The calculation is based on a chiral reduction formalism. Panel (d) shows the calculation from Cassing and Bratkovskaya. A microscopic relativistic transport model (HSD) is used in the calculation. It incorporates the relevant off-shell dynamics of the vector mesons. These models are relative to chiral symmetry restoration. Models can not reproduce the excess measured by PHENIX.

The accurate theoretical description of the chiral symmetry restoration in heavy ion collisions can be addressed with precise measurement in future.

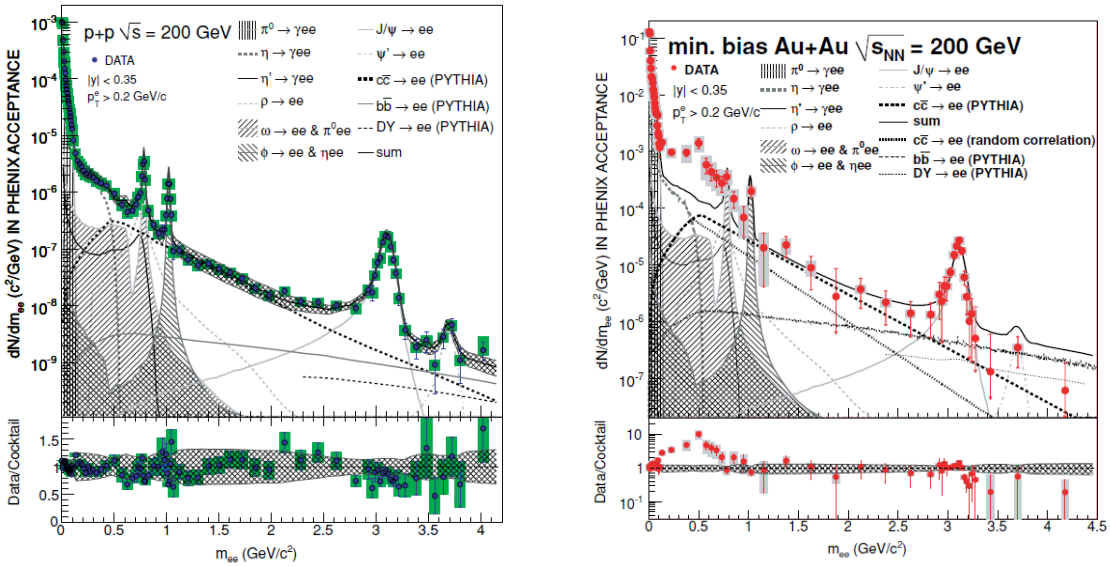

Figure 1.10: Left: inclusive mass spectrum of e^+e^-pairs in the PHENIX acceptance in p+p collisions. The expectation from the light hadrons decays, correlated open charm, bottom decays and Drell-Yan compared to the e^+e^-signals. Right: inclusive mass spectrum of e^+e^-pairs in the PHENIX acceptance in minimum bias Au+Au. The expected contributions from the decays of light hadrons and correlated decays of charm bottom and Drell-Yan compared to the e^+e^-continuum. Figure is from [Ada10].

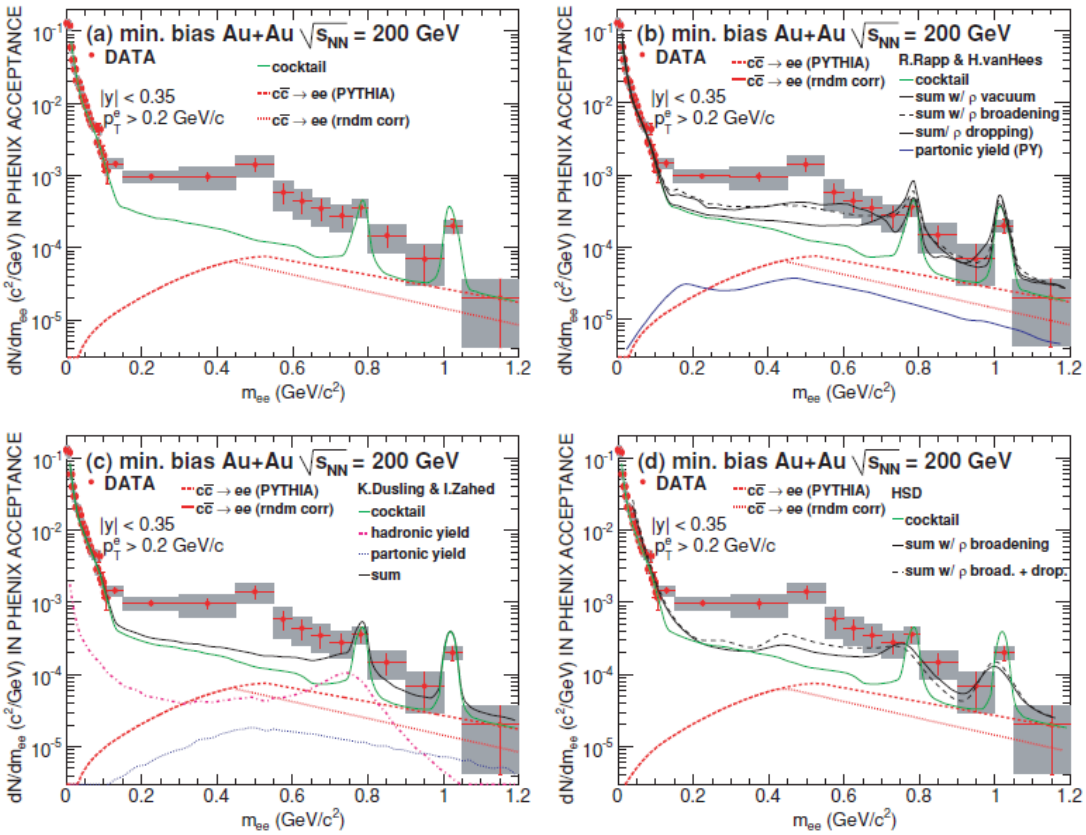

Figure 1.11: Comparison of PHENIX di-electron continuum in Au+Au collisions in the LMR to the sum of cocktail (a) and the contribution from different models. Calculations are from: Panel (b) Rapp and van Hees [Rap01, Rap02],Panel (c) Dusling and Zahed [DZ09, DTZ07, DZ10], and panel (d) Cassing and Bratkovskays [MBC11, CB99, BC08]. Figure is from [Ada10].

CHAPTER 2

Experiment Set-up

2.1 RHIC Accelerator Complex

The Relativistic Heavy Ion Collider (RHIC) at Brookhaven National Laboratory (BNL) provides an excellent environment to discover and study the hot dense matter called Quark Gluon Plasma (QGP). It accelerates and collides heavy ions and polarizes protons with high luminosity, allowing physics to explore the strong interaction through many extensive and intensive measurements. It can be operated at wide range of energies, and a variety of beams: p+p, d+Au, Cu+Cu, and Au+Au with energies up to $\sqrt{s_{\rm NN}}$= 200 GeV. RHIC is also delivering polarized proton beams up to center-of-mass energy 500 GeV to carry on vigorous spin scientific programs. The basic design parameters of the collider are listed in Tab. 2.1 [HLO03].

The RHIC machine complex is shown in Fig. 2.1, including a Van de Graaff facility, a linear proton accelerator, the Booster synchrotron, the Alternative Gradient Synchrotron (AGS), and ultimately the RHIC synchrotron ring. In Au+Au collisions, the Au ions with charge $Q = -1e$ stem from the Pulsed Sputter Ion Source. Then they go through the Van de Graaff facility and a series of stripping foils, and be accelerated to a kinetic energy of 1 MeV/nucleon at the exit with a net charge of $Q = +32e$. The ions are then injected into the booster synchrotron and accelerated to an energy of 95 MeV/nucleon. They are further stripped to $Q = +77e$ after leave the booster, then transferred into the AGS, where they are accelerated to 8.86 GeV/nucleon and sorted into four final bunches. At the final step, the ions are stripped to the bare charge state of $Q = +79e$ and injected into RHIC. For proton operations, protons are injected from the 200 MeV Linac into the

Table 2.1: Performance specifications of RHIC

	For Au+Au	For p+p
Beam energy	→100 GeV/nucleon	30→250 GeV/nucleon
Luminosity	$2 \times 10^{26} cm^{-2} s^{-1}$	$1.4 \times 10^{31} cm^{-2} s^{-1}$
Number of Bunches/ring	60(→120)	60(→120)
Luminosity lifetime	∼10 hours	>10 hours

booster, followed by acceleration in the AGS and injection into RHIC.

RHIC consists of two concentric super-conducting accelerator/storage rings, the circumference is about 3.8 km. The rings are on the same horizontal plane in the tunnel, and there are six intersection points along their circumference. Four of them were equipped with detectors. Fig. 2.1 shows the four experiments positions at RHIC , two large experiments STAR and PHENIX are located at 6 o'clock and 8 o'clock and two small ones PHOBOS and BRAHMS were located at 10 o'clock and 2 o'clock, respectively. The PHOBOS and BRAHMS have been de-commissioned since 2008.

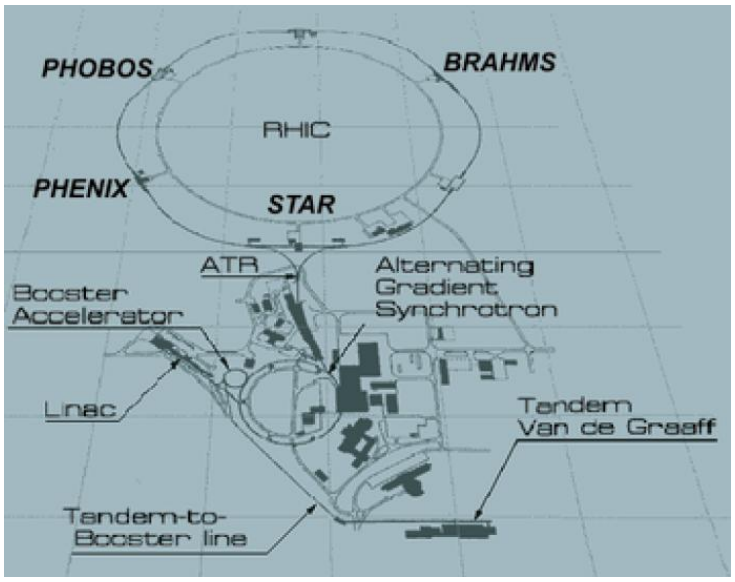

Figure 2.1: Schematic of the RHIC complex.

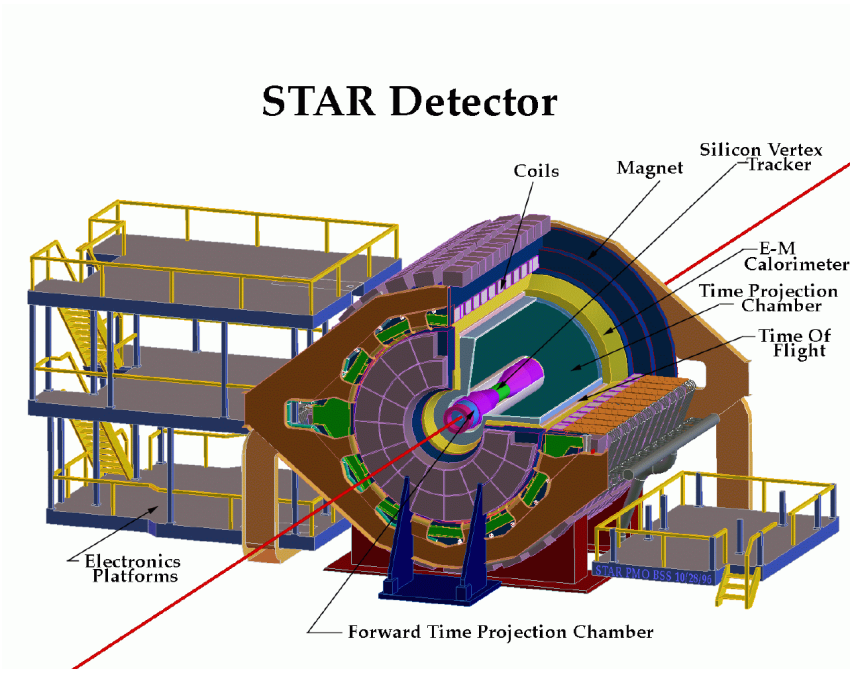

Figure 2.2: STAR detectors.

2.2 STAR Detector

The Solenoidal Tracker at RHIC (STAR) was specially constructed to investigate the behavior of strongly interacting matter at high energy density and to search for signatures of QGP information. RHIC creates a nuclear environment of a large number of produced particles (up to approximately one thousand per unit pseudorapidity) and high momentum particles from hard parton-parton scattering. The main motivation to build the STAR was to measure many observables simultaneously to study signatures of a possible QGP phase transition and to understand the space-time evolution of the collision process in ultra-relativistic heavy ion collisions. The goal is to obtain a fundamental understanding of the microscopic structure of these hadronic interactions at high energy densities. In order to accomplish this, STAR was designed primarily for measurements of hadron production over a large solid angle. STAR is also very effective in high precision tracking, momentum analysis, and particle identification at the central rapidity region. The large acceptance of STAR detector makes it well suited for event-by-event characterizations of heavy ion collisions and for the detection of hadron jets [Ack03].

Fig. 2.2 shows the layout of the STAR detector along with the subsystems, and Fig. 2.3 shows the cross-sectional side view of the STAR detector. The whole detector is enclosed in a solenoidal magnet that provides a uniform magnetic field parallel to the beam direction. The STAR magnet [Ber03] is designed as a cylinder with a length of 6.85 m and has inner and outer diameter of 5.27 m and 7.32 m, respectively. The maximum magnetic field along the z direction is $|B_z| = 0.5T$. STAR has been run in full field, reversed full field and half field configurations.

There are two detectors using for tracker at STAR. The Time Projection Chamber (TPC) is the main tracker of STAR. It covers the $|\eta| < 1.8$ and with complete azimuthal symmetry ($\Delta\phi = 2\pi$). A radial-drift TPC (FTPC) is installed at $2.5 < |\eta| < 4$ and with 2π coverage to identify tracks at forward region.

STAR has two Electro-Magnetic Calorimeter, Barrel Electro-Magnetic Calorimeter (BEMC) located outside of the TPC covers $|\eta| < 1$ with complete azimuthal symmetry [Bed03] and the Endcap Electro-Magnetic Calorimeter (EEMC) coverage for $1 < |\eta| < 2$, over the full azimuthal range [All03]. The EMCs are used to distinguish high momentum single photons from photon pairs of π and η meson decays and electrons from charged hadrons. The EMCs also provide prompt charged particle signals essential to discriminate against pileup tracks in the TPC, arising from other beam crossings falling within the 40 μs drift time of the TPC, which are anticipated to be prevalent at RHIC p+p collision luminosity ($\sim 10^{32} cm^{-2} s^{-1}$). The EMCs are also used as a high p_T hadron and electron trigger.

The STAR Time-Of-Flight (TOF) [Sha06a, Don06, Llo05] has been installed $\sim 3/4$ coverage in RHIC year 2009 and completed in RHIC year 2010. It locates between TPC and BEMC, covers $|\eta| < 0.9$ and full azimuthal angle, has $< 80ps$ intrinsic timing resolution and $> 95\%$ detecting efficiency. The TOF improves the low and moderate p_T range particle identification, extends π/K separation from 0.7 GeV/c to 1.6 GeV/$c$and proton/(π, K) separation from 1.1 GeV/c to 3 GeV/c. Combining with TPC, it also provides electron identification at $p_T >$ 0.2 GeV/c, this enlightened the di-electron analysis at STAR.

The STAR trigger system is designed to facilitate the event selection for purpose of new states of matter and understand the properties of interior hadrons. It is a 10 MHz pipelined system in which digitized signals from the fast trigger detectors, and is used to control the event selection for the much slower tracking detectors. The fast detectors include zero-degree calorimeters (ZDC) located in the forward direction at $\theta < 2$ mrad, Beam-Beam counter (BBC) which consists of a hexagonal scintillator array structure at $\pm 3.5m$ from the nominal interaction point, and Vertex Position Detectors (VPD).

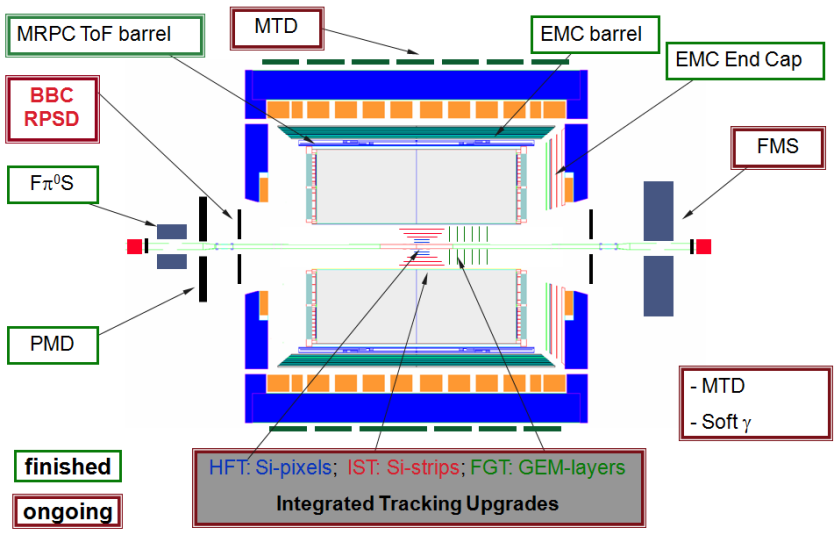

Figure 2.3: Cutaway side view of the STAR detectors.

2.2.1 Time Projection Chamber

The Time Projection Chamber (TPC) [And03], the heart of STAR detector, is the main tracking detector in the STAR experiment. The TPC is capable of recording the tracks of particles, measuring their momenta and identifying the particles by measuring their ionization energy loss (dE/dx).

Fig. 2.4 shows the TPC structure schematically. Shape of the TPC is cylindrical with a length of 4.2 m and diameter 4m. The cylinder is concentric with beam line. It is an empty volume of gas in a well-defined, uniform, electric field of $\sim$ 135 V/cm. When charged particles traverse the gas volume and liberate electrons due to the ionization energy loss, the paths of particles are reconstructed with high precision from the released

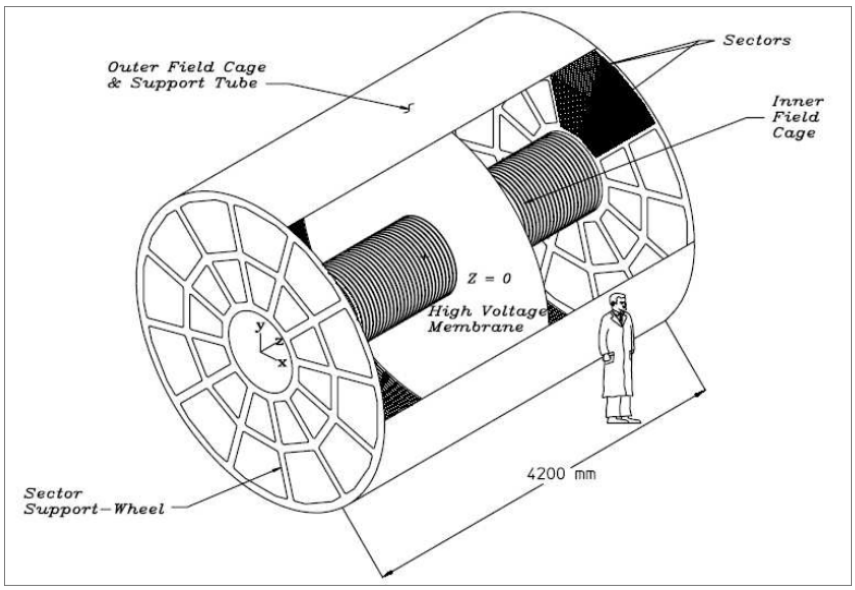

Figure 2.4: The STAR TPC surrounds a beam-beam interaction region at RHIC. The collisions take place near the center of the TPC [And03].

secondary electrons which drift to the read out end caps at the ends of the chamber. The uniform electric field which is required to drift the electrons is defined by a thin conduction Central Membrane (CM) at the center of the TPC, concentric field-cage cylinders and the readout end caps.

The TPC volume is filled with P10 gas (90% Ar, 10% CH4) at 2 mbar above the atmospheric pressure [Koc03]. The P10 gas has an advantage of fast drift velocity which peaks at a low electric field. Operating on the peak of the velocity curve makes the drift velocity stable and insensitive to small variations in temperature and pressure. Low voltage greatly simplifies the field cage design. The drift velocity of P10 gas is 5.45 cm/μs. The transverse diffusion in P10 gas is about $\sigma_T = 3.3$ mm after drifting 210 cm. The longitudinal diffusion of a cluster of electron that drifts the full length of the TPC is $\sigma_L = 5.5$ mm. The longitudinal diffusion width sets the scale for the resolution of the tracking system in the drift direction. The shaping time and electronic sampling rate are chosen accordingly, having values 180 ns FWHM and 9.4 MHz, respectively.

The TPC readout system is based on Multi-Wire Proportional Chamber (MWPC) with readout pads. The readout planes, MWPC chambers with pad readout, are modu-

lar units mounted on aluminium support wheels. These readout modules or sectors, are arranged as on a clock with 12 sectors around the circle in the ϕ plane. The chambers consist of a pad plane and three wire planes. The readout or amplification layer is composed of the anode wire plane with the pad plane on one side and the ground wire plane on the other. The third plane of the chamber is a gating grid which is the outermost wire plane on the sector structure. This grid is a shutter to control entry of electrons from the TPC drift volume into the MWPC. The positive ions produced in the MWPC are blocked by the grid, can not enter the drift volume and could not distort the drift field. The grid is "open" to the drift of electrons while the event is being recorded, with all of the wires on the same potential ($\sim$110 V). It is "closed" when the voltages alternate $\pm$75 V from the nominal value. The ground grid plane of 75 μm wires completes the sector MWPC. The primary purpose of the ground grid is to terminate the field in the avalanche region and provide additional rf shielding for the pads.

Fig. 2.5 shows the structure of one full sector. Each sector is divided into inner and outer subsectors characterized by a change in the readout padrow geometry. Each subsector consists of straight rows of pads that act as cathodes. The inner radius subsectors are in the region of highest track density and thus optimized for good two-hit resolution. This design uses smaller pads of dimension 2.85 mm $\times$ 11.5 mm in 13 rows (1-13) to improve the hit resolution. It improves the tracking by reducing the occurrence of split tracks. The advantages of inner sector are to extend the position measurements along the track to small radii thus improving the momentum resolution and the matching to inner tracking detectors. The detection of particles with lower momentum is also benefited by the design. The outer radius subsectors have continuous pad coverage to optimize the dE/dx resolution. This is optimal because the full track ionization electrons improve statistics on the dE/dx measurement and hence improve the particle identification. Another modest advantage of full pad coverage is an improvement in tracking resolution due to anti-correlation of errors between pad row. The outer sector consists of 32 pad rows (14-45) with pad dimension 6.2 mm$\times$19.5 mm. The details of the subsectors are summarized in Tab. 2.2.

Table 2.2: Parameters of the TPC inner and outer subsectors.

Item	Inner subsector	Outer subsector	Comment
Pad size	2.85 mm× 11.5 mm	6.20 mm× 19.5 mm	
Isolation gap between pads	0.5 mm	0.5 mm	
Pad rows	13	32	
Number of pads	1750	3942	5692 total
Anode voltage	1170 V	1390 V	20:1 signal:noise
Anode gas gain	3770	1230	

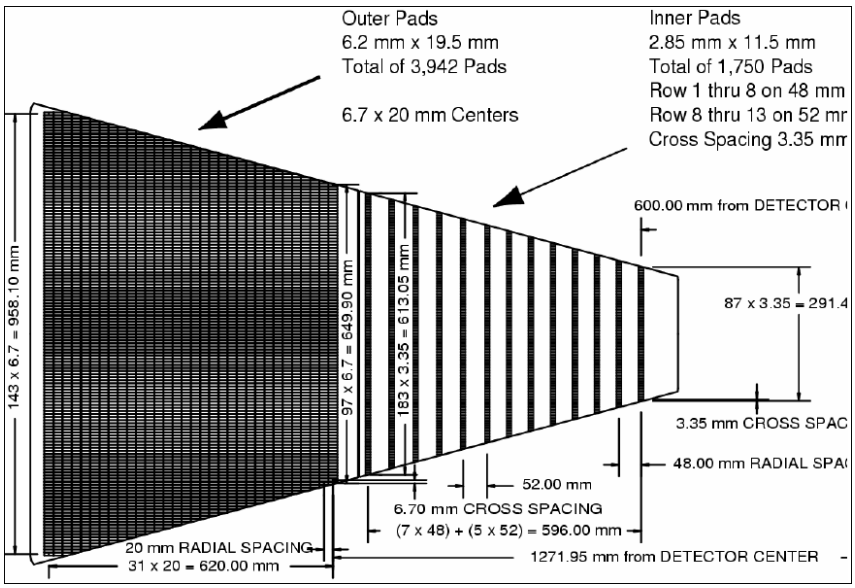

Figure 2.5: The anode pad plane with one full sector shown. The inner subsector is on the right and it has small pads arranged in widely spaced rows. The outer subsector is on the left and it is densely packed with larger pads.

The track reconstruction of a primary particle passing through the TPC bases on the ionization clusters along the track. The clusters are found separately in transverse plane along the beam line. The position resolution is on the level of millimeter, it depends on the drift length, the angle between the particle momentum and the drift direction. The ionization clusters of a track are fitted to track models, which is a helix with a second-order effects include the energy lost in the gas which cause a particle trajectory to deviate slightly from the helix. The track is then be extrapolated to the other detectors and the points from other detectors might be added. At the end, the tracks are refitted in the local coordinate system of the TPC based on a 3D helix model and from now on are called global tracks. The primary collision vertex is reconstructed from these global tracks with pretty good accuracy. The vertex resolution inversely proportional to the square root of the number of tracks in the calculation and can reach 350 μm in central Au+Au collisions. The global tracks with a distance to the primary vertex smaller than 3 cm (*distance of closest approach (DCA)*, can be refitted using the primary vertex as additional point in the fit. The refit tracks are marked as primary tracks and stored into a separated tracks collection in the container. The momentum resolution of primary track in $p+p$ collisions is approximately $\Delta p_T/p_T \approx 1\% + 0.5\% \times p_T$.

Particle species are identified in the TPC by the value of energy loss in the TPC gas volume. The energy loss of a charged particle is measured by the deposit charge collected on the pad rows. The deposit charge are from drifting electrons liberated by the charged particles. The dE/dx is extracted from the energy loss measured on up to 45 pad rows. Energy loss of a charged particle for a given track length can be described by the Bichsel function [Bic06]. However, the mean of the distribution is sensitive to the fluctuations in the tail of the distribution. Therefore, the most probable energy is measured by removing the highes 30% measured clusters. Fig. 2.6 shows the 70% truncated mean dE/dx distribution. The resolution of dE/dx is less than 8%, that makes the π/K separation up to p$\sim$0.7 GeV/c and proton/(π,K) separation up to p$\sim$1.1 GeV/c. At high momentum ($p > 3$ GeV/c), the particles can be also separated by the dE/dx due to the relativistic rise [Sha06b, Xu08]. This method is especially more powerful for high

momentum electron identification. The $e/\pi(e/K)$ separation is approximately 3σ (5σ) at $p_T = 3$ GeV/c and 2σ (3.5σ) at $p_T = 10$ GeV/c [Xu08].

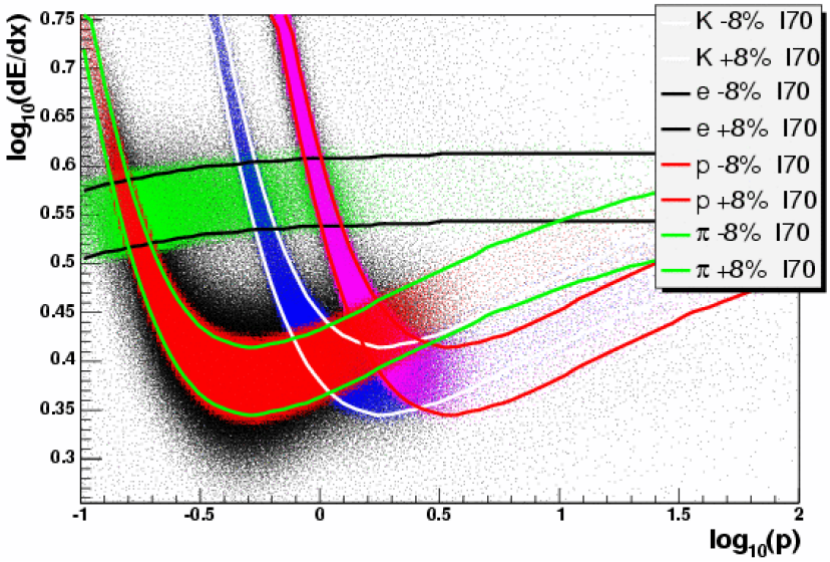

Figure 2.6: Distribution of $log_{10}(dE/dx)$ as a function of $log_{10}(p)$ for electrons, pions, kaons and protons. The units of dE/dx and momentum are keV/cm and GeV/c, respectively. The color bands denote within $\pm 1\sigma$ the dE/dx resolution. I70 means Bichsel's prediction for 30% truncated dE/dx mean.

2.2.2 Barrel Electro-Magnetic Calorimeter

The STAR BEMC is a fast detector, has ability to trigger on and study rare, high p_T processes (jets, leading hadrons, direct photons, heavy quarks), and provide large acceptance for photons, electrons, π^0, η, J/ψ, Υ mesons in systems spanning polarized $p+p$ through Au+Au collisions.

The BEMC is located at interval between the TOF and the aluminum coil of the STAR solenoid, and covers $|\eta| \leq 1$ and 2π in azimuthal, matching the acceptance for full TPC tracking. The radius of inner surface of the BEMC is about 220 cm to the beam line.

The design for the BEMC includes a total of 120 calorimeter modules, each occupying 6° in $\Delta\phi$ (~ 1 rad) and 1.0 unit in $\Delta\eta$. These modules are mounted 60 in ϕ and 2 in η. Each module is 26 cm wide and 293 cm long with an active depth of 23.5 cm plus ~ 6.6

cm in structural plates (of which $\sim$ 1.9 cm lies in front of the detector). The modules are further segmented into 40 towers, 2 in ϕ and 20 in η, with each tower occupying 0.05 in $\Delta\phi$ by 0.05 in $\Delta\eta$. The full BEMC is thus physically segmented into a total of 4800 towers, each of which is projective, pointing back to the center of the TPC. Fig. 2.7 shows a schematic side view of a module illustrating the projective nature of the towers in the η direction [Bed03].

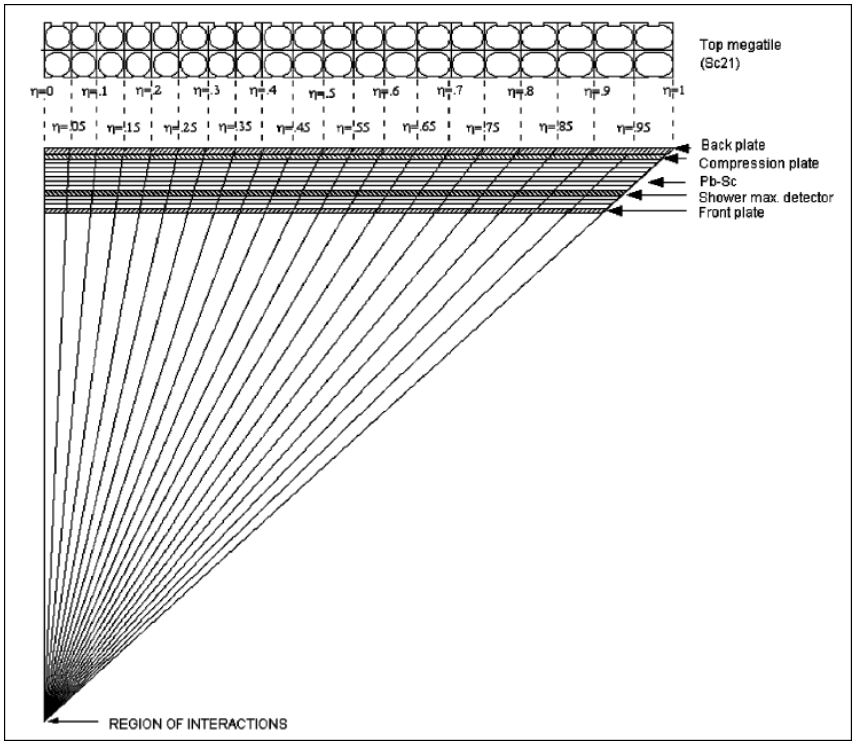

Figure 2.7: Side view of a calorimeter module showing the projective nature of the towers. The 21st mega-tile layer is also shown in plan view.

The BEMC is a sampling calorimeter using lead and plastic scintillator with the large area and complex geometry. An end view of a module with the mounting system and the compression components is shown in Fig. 2.8. The core of each BEMC module consists of a lead-scintillator stack and shower maximum detector (SMD) situated approximately 5 radiation lengths from the front of the stack. There are 20 layers of 5 mm thick lead, 19 layers of 5 mm thick scintillator and 2 layers of 6 mm thick scintillator. The thicker scintillator layers are associated with the preshower detector which is significantly helpful in both π^0/γ and electron/hadron discrimination.

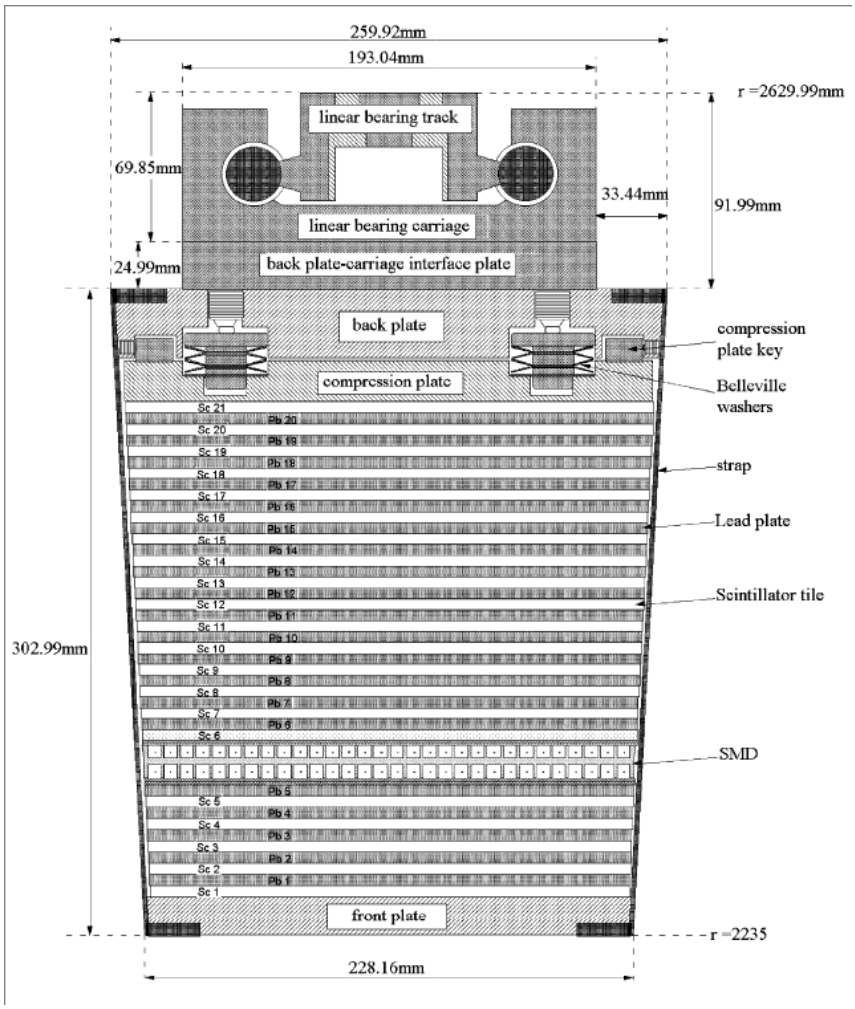

Figure 2.8: End view of a STAR BEMC module showing the mechanical assembly including the compression components and the rail mounting system. The location of the two layers of shower maximum detector at a depth of approximately $5X_0$ from the front face at $\eta = 0$ is also shown.

The total depth of BEMC is $\sim$ 20 radiation length (20 X_0) at $\eta = 0$. The intrinsic energy resolution of tower is $\sigma_E/E \approx 1.5\% \oplus 14\%/\sqrt{E}$. The hadron background can decrease the effective resolution. In central Au+Au collisions, the resolution for electron energy at 1.5 GeV and 3 GeV is around 17% and 10%, respectively [Bed03].

2.2.3 Barrel Shower Maximum Detector

The segmentation (towers) of STAR BEMC is significantly larger than an electromagnetic shower size. Each of its 4800 towers span $\Delta\phi \times \Delta\eta = 0.05 \times 0.05$ which at the radius of the inner face of the detector correspond to tower size $\sim 10 \times 10 cm^2$ at $\eta = 0$ increasing towards $\eta = 1$. The towers can measure the energy precisely and isolate electromagnetic showers but its spatial resolution is not fine enough to measure the shower shape and shower size to distinguish direct γ and π^0. The Shower Maximum Detector (SMD) was embedded into the BEMC to provide fine spatial resolution [Bed03].

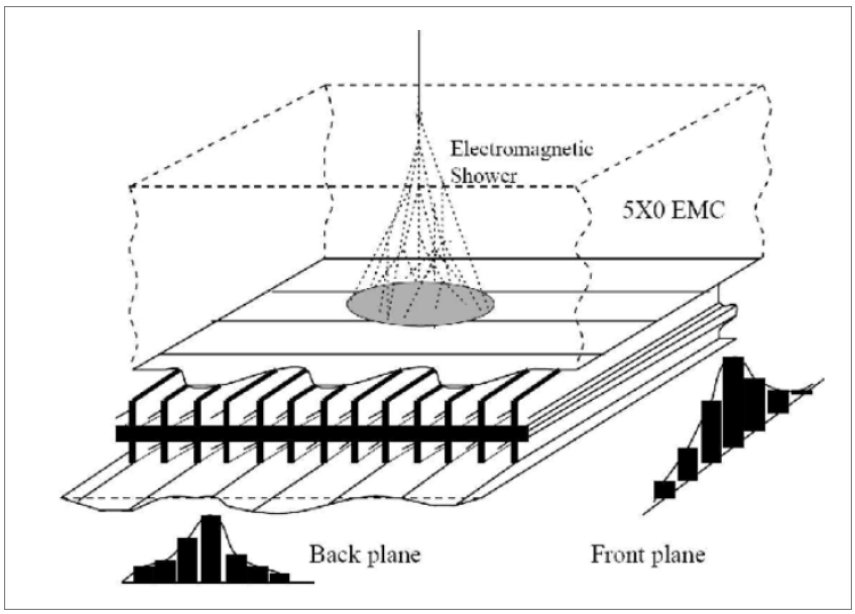

Figure 2.9: Schematic illustration of the double layer STAR BSMD. Two independent wire layers, separated by an aluminum extrusion, image electromagnetic showers in the η and ϕ on corresponding pad layers.

The conceptual design of the SMD is shown in Fig. 2.9. The SMD sits at about 5 radiation length depth in the calorimeter modules, at $\eta = 0$, including all material in

front of the calorimeter. The STAR SMD has a unique feature of double layer design. A two sided aluminum extrusion provides ground channels for two independent planes of proportional wires. In the η and ϕ directions, there are independent PC Board cathode planes with strips etched allowing two dimensional size measurement of the shower. The SMD is a wire proportional counter-strip readout detector using gas amplification. The aluminium extrusion has 5.9 mm wide channels running in the η direction, and 50 μm gold-plated tungsten wires in the center. The detector strips sense the induced charge from the charge amplification near the wire. There are two sets of strips around the wire outside the aluminum extrusion, one is parallel to the wire channel while the other one is perpendicular to the wires, The two sets of strips provide an image of the shower spatial distribution in the η direction and ϕ direction. Each of these strips span 30 channels (30 wires), the strip perpendicular to wires has size of 0.1 radians in ϕ ($\approx 23cm$, *i.e.* the module width) and 0.0064 in η($\approx 1.5cm$ at low η), the parallel strip is physically 1.33 cm wid and has length 0.1 units in η, while the wires are 1.0 units in η.

The BSMD has an has an approximately linear response versus energy, at the depth of $5X_0$ inside the EMC, in the energy range from 0.5 to 5 GeV. The ionization at the back plane of the BSMD is about 10% lower than the front plane. The energy resolution in the front plane is given approximately by $\sigma_E/E = 12\% + 86\%/\sqrt{E}\ GeV$ with the energy resolution on the back plane being 3-4% worse. The position resolution in the front and back planes are given approximately by $\sigma_{front} = 2.4mm + 5.6mm/\sqrt{E}\ GeV$ and $\sigma_{back} = 3.2mm + 5.8mm\sqrt{E}\ GeV$.

2.2.4 Barrel Time of Flight

STAR has performed the upgrade of full barrel Time-Of-Flight (TOF) detector based on the Multigap Resistive Plate Chamber (MRPC) technology. The MRPC technology was first developed by the CERN ALICE group [Cer96] to provide a cost-effective solution for time-of-flight measurement with large coverage.

Fig. 2.10 shows side and end views of an MRPC module appropriate for STAR. The

MRPC basically consists of a stack of resistive plates arranged in parallel. The resistive plates is utilized to quench the streamers which initiate a spark breakdown. The plates one from the other have equal sized spacers. This structure creates a series of gas gaps. The outer surfaces of the plates while applying a strong electric field, keep the MRPC works in avalanche mode. The typical size of a MRPC module is 94 $mm \times 212$ $mm \times 12$ mm and the active area is 61 $mm \times 200$ mm, and has 6 readout pads which has an area of 63 $mm \times 31.5$ mm, the distance between pads is 3 mm. Fig. 2.10 shows side and end views of the MRPC module developed for STAR. A cross-section view of the module is shown in Fig. 2.11.

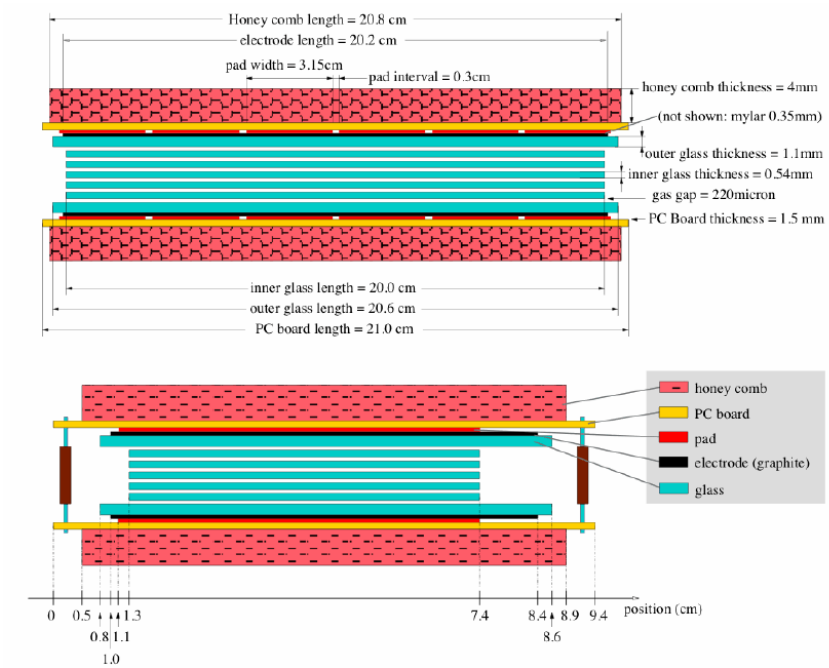

Figure 2.10: Two side views of MRPC. The upper (lower) is for long (short) side view. The two plots are not at the same scale.

The first prototypes of TOF were installed in run III. In run 9, 86 out of 120 trays (72%) were installed at a radius 220 cm out of TPC center at STAR. The TOF worked well and stably during data taking. Only 2 channels out of 16512 were dead. In run 10, all trays were installed with 2π azimuthal coverage. 119 trays participated in nearly all runs, only one tray is out due to a high voltage problem.

A tray includes 32 MRPC modules placed along beam line direction. Each module

includes 6 pads (also called as cell/channel) with read-out strips span azimuthal (ϕ) direction. The geometric location and the definition of local coordinate system on each pad are shown in Fig. 2.11.

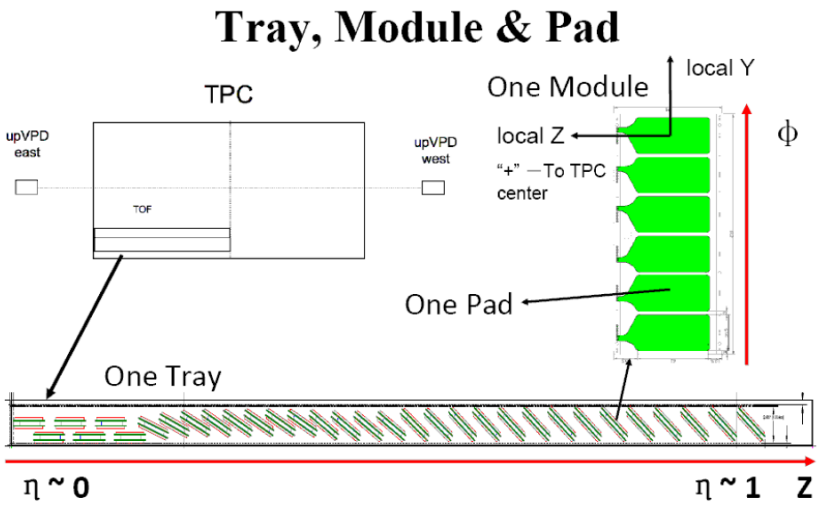

Figure 2.11: Geometry of trays, modules and pads.

TOF system consists of two parts, TOF trays and Vertex Position Detectors (VPD), corresponding to the stop time and start time measurement, respectively. The TOF trays can provide the stop time of tracks which lit the pads. The VPD measures the common start time of the event and also the independent vertex Z component. The timing resolution for each VPD or TOF tray channel is on nanosecond level before calibration. After calibration, the resolution can be improved by an order of magnitude. In general, there are three steps for TOF system calibration: TDC integral non-linearity calibration, VPD calibration, and TOF trays calibration [Sha09].

Integral Nonlinearity (INL) and calibration in TDIG board channel In TOF readout system, TDIG boards are used to read out the time information from MRPC through TINO boards. There are about 1000 TDIG boards used for the entire STAR-TOF system. Each TDIG board has 3 HPTDC chips with 8 read-out channels. The TDC data system acquires data into all TDC bins. But the bin width of each HPTDC bins are not even for the following three reasons.

- A. The HPTDC uses tapped delay line architecture to perform its time-sampling function. The 40 MHz input clock is multiplied on chip to 320 MHz. This 3.125 ns clock signal is fed through a 32-tap delay locked loop (DLL). The unequal bin widths in the DLL are the reason of the differential nonlinearity in HPTDC.

- B. The DLL tap intervals are further subdivided by a 4-tap resistor-capacitor (RC) delay network. The unequal bin widths in the RC tapped delay lines are another source of differential nonlinearity in HPTDC.

- Noise coupling from the logic clock network (40 MHz) within the chip into the sampling clock network (320 MHz) also contributes to the differential nonlinearity in HPTDC.

The nonlinearity of the RC, DLL and the clock feed through is periodic over 4, 32, and 1024 bins (25 ns), respectively. In all cases, these effects are deterministic and periodic for a given chip. Once the DLL and RC parameters are fixed, the clock noise coupling can be determined. There is a standard technique to measure the bin width called as code density test. A pulse generator inputs a uniformly random distribution (with respect to HPTDC clock) into 2 HPTDC channels, if all TDC bins have the same width, then the probability of a pulse arriving in any bin would be the same as that of any other bin. The bin value variations can be measured directly with enough statistics by this method. In the TDIG calibration setup at Rice University, one uses a so called cable delay test, which uses the similar data acquisition condition as STAR-TOF, to perform the Integral Nonlinearity calibration. After calibration, the INL parameters for all boards are saved and uploaded to offline database. The average time resolution per electronic channel is about 14 ps.

VPD calibration The VPD has 19 channels on the east side and 19 channels on the west side. Each channel records tdc and tot information, the tdc is the time of the leading edge of a pulse which reach the threshold, and the time-over-threshold (tot) is the duration of the pulse stay over the threshold. The tot is correlated with the amplitude

of the pulse. The slewing correction is done by removing the correlation of tdc and tot, on east side and west side separately. Since the tdcs are not absolute times but random event-by-event, the reference time of tdc for a channel is determined by the average tdc of the other fired channels in a same event. Fig. 2.12 shows an example for the slewing correction. To ensure a good reference time, we require at least 3 hits on the east and west side in a event.

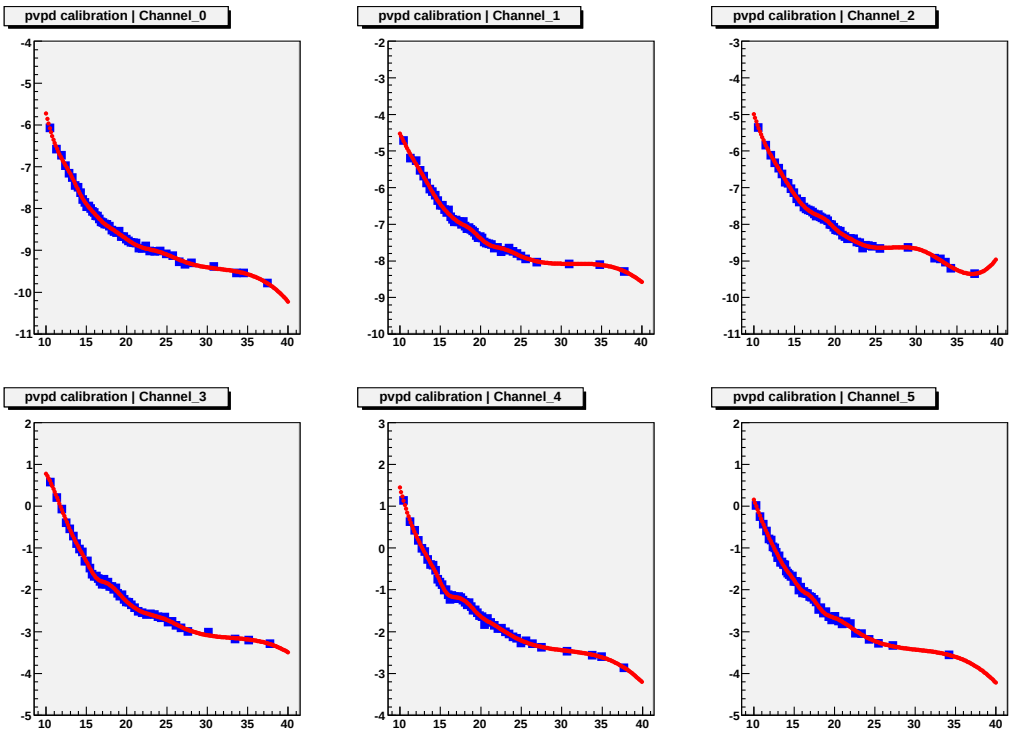

Figure 2.12: An example of tdc vs. tot correlation for VPD slewing correction. The units are ns for each axis. The blue squares are the data points, the red lines represent the Spline fit.

After slewing correction (usually several iterations to correct the residual correlation), the corrected timing of each channel is obtained. For each side, the timing difference between channels on the same side was shifted to zero, but the event start time can not be determined only by the phase difference of two sides of VPD. It is directly correlated with z component of vertex (Vz). The values of vertex z measured by VPD and TPC have a correlation between them. After applying the phase difference between east VPD and west VPD, we shift the mean value of the distribution of Vz(VPD)-Vz(TPC) to zero.

Then the start time of the event can be calculated as:

$$T_{start} = \frac{\sum t_e + \sum t_w - (N_e - N_w) \times V_z/c}{N_e + N_w}. \tag{2.1}$$

Where the $\sum t_e, \sum t_w$ means the sum of the corrected timing of east fired VPD channels and west fired VPD channels, respectively. N_e, N_w means the number of fired channels in east and west side of VPD, respectively. c is light velocity.

TOF tray calibration Once the VPD calibration has been done, the event start time (T_{start}) is determined. The TOF trays provide the stop time of each track. The difference of the two timings is the time of flight (tof) of the associated track. To calibrate the each TOF channel, a tof reference should be known. Usually, a pure pion sample at low momentum is always used to obtain the reference tof. The pure pion sample is identified by TPC. Once the pion was identified, the velocity of the pion can be calculated by the momentum and mass. The track length can be also gotten by projecting the track helix onto TOF. Then the expected time of flight ($tof_{expected}$) of the pion track can be known. By shifting the $tof - tof_{expected}$ to zero, the correction for each channel can be obtained.

The TOF trays calibration consists of 3 parts: T_0 correction, slewing correction and hit position correction. The T_0 correction is due to the different cable lengths and signal transition time for different read-out channels. The slewing correction is quite similar as the VPD because of the electronics are same. The different hit position along the local z direction on the read-out strips result in different transition time. The tof is correlated with the distance between the hit position and the read-out end along the strips which is designed as Z direction. The correction method is similar as that of slewing correction, just use z instead of tot. The 3 corrections are corrected separately in one iteration, and after several iterations all of the TOF trays calibration parameters are obtained. The correction procedures can be summarized as Fig. 2.13. For an example of the calibration results, the overall resolution of TOF system is shown in Fig. 2.14. The calibration was done for the fast offline production and HLT trigger in Au+Au at 200 GeV in run 10. After

Table 2.3: TOF system performance in different runs.

Operation condition		Timing Resolution (ps)		
		VPD	Overall	TOF
Run9	200 GeV p+p	81	110	74
Run10	200 GeV Au+Au	28	87	82

calibration, two kinds of Particle Identification (PID) methods are implement for variety analysis. One can chose either m^2 spectrum or $1/\beta$ functions to select the particles. The mass distribution and inverse velocity ($1/\beta$) vs. momentum distribution after calibrations are shown in Fig. 2.15.

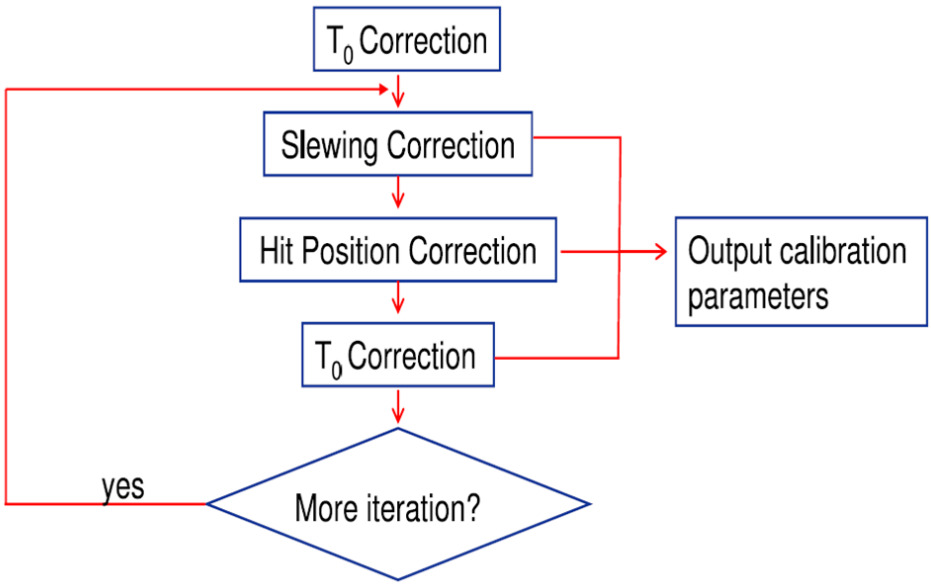

Figure 2.13: TOF tray calibration procedures.

The resolutions in run 9 p+p and run 10 Au+Au at 200 GeV from final offical offline production are summarized in Tab. 2.3.

Recent observation of anti-α particle at STAR is an example for the applications of the TOF detector and its calibrations. TOF system has been embedded into the High-Level-Trigger (HLT) at the beginning of run 10 as a part of my job. HLT is an online trigger to select the rare events taken by TPC to save the tape storage and quickly sample the rare

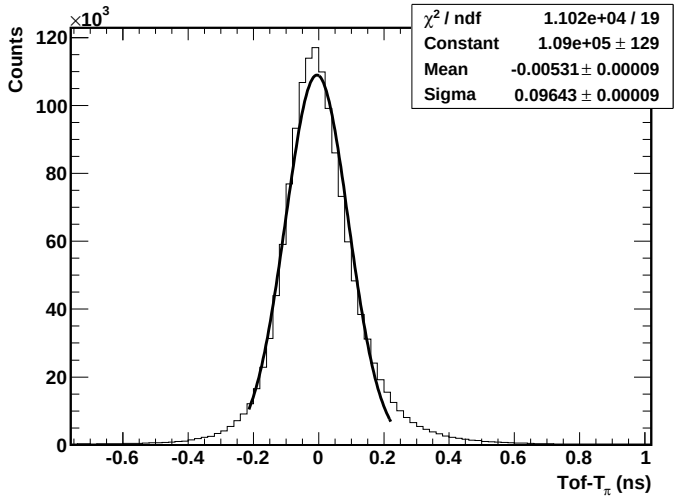

Figure 2.14: Overall resolution of TOF system in run 10 fast offline production.

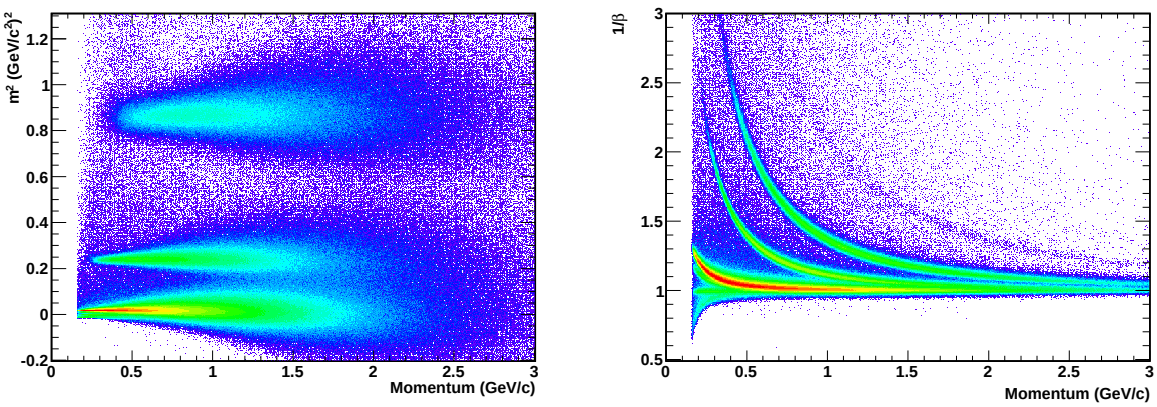

Figure 2.15: Left: M^2 vs. momentum distribution after TOF calibrations. Right: inverse velocity vs. momentum distribution after TOF calibrations.

events with high efficiency, such as J/ψ and heavy nuclei events. The HLT event selection relies on the online particle identification, so it needs fast and reliable calibration tables to correct raw data taken from detectors. As a result, 18 anti-α counts were detected in 10^9 recorded Au+Au collisions at 200 GeV and 62 GeV [Aga11b]. Fig. 2.16 shows a PID of anti-α, the PID based on dE/dx measured by TPC and the mass measured by TOF.

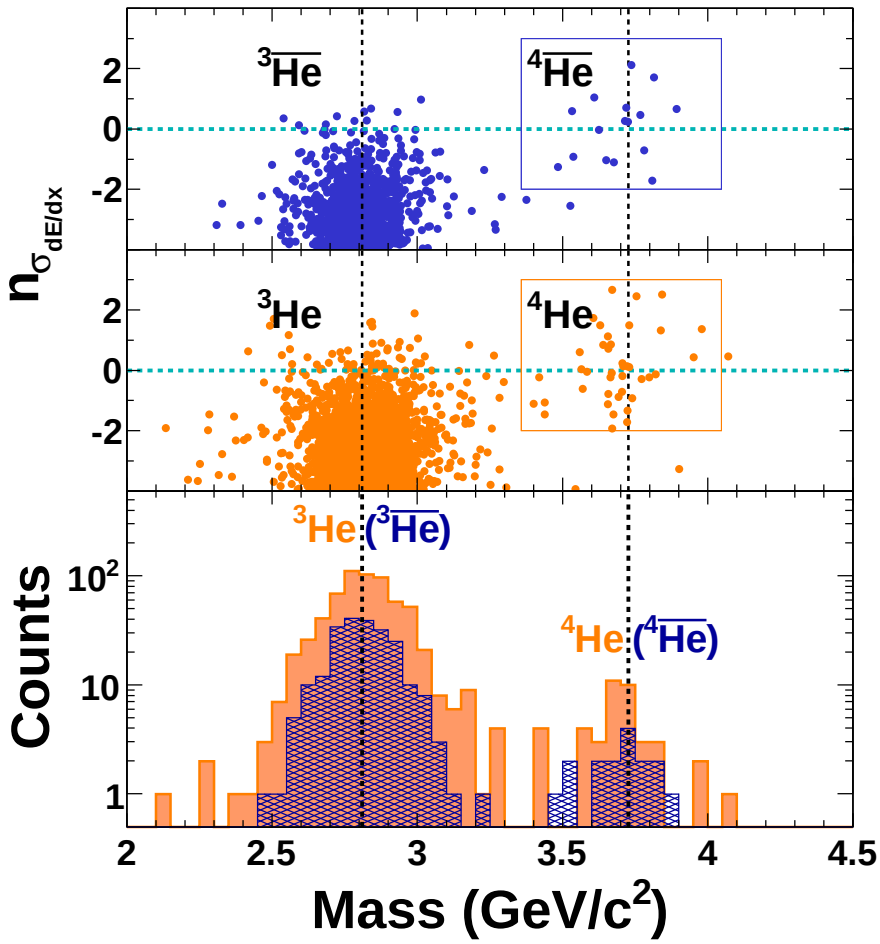

Figure 2.16: Top two panels: $n\sigma_{dE/dx}$ as function of mass measured by TOF system. Bottom panel: the masses of Helium-3 and Helium-4 and their anti particles. Figure is from [Aga11b].

2.3 Detector upgrades

STAR is proposing a μ detector, Muon Telescope Detector (MTD). The MTD sits outside of the STAR magnet, using the BEMC and the magnet steel as absorber to stop electrons and hadrons. It has 40-50% detect efficiency including acceptance effect for μ at $p_T >$ 2 GeV/c. MTD is based on long-MRPC technology, covers 45% acceptance at $|\eta| < 0.5$. The first MTD prototype has been put in from RHIC year 2007 run, and works very well [Rua08, Sun08]. It is proposed that 80% of the full system be installed and ready in RHIC year 2014 run. It will provide excellent measurements for heavy flavor collectivity and production.

The other two detectors, Forward GEM Tracker (FGT) [Sim08] and vertex detector Heavy Flavor Tracker (HFT) [Sha07a, Kap08], are proposed and still in preparation. The FGT is designed to improve the precision of the tracking at the forward region. The HFT is an expectant vertex detector. It will have two layers of pixels with limited materials located at mean radius of 1.5 cm and 5 cm from the beam axis and will be combined with the Silicon Strip Detectors (SSD) [Arn03] to fill the gap between the innermost silicon detectors and the TPC. The first layer of HFT has a resolution of 10 μm over a large pseudo-rapidity range and full azimuthal coverage. The two layers of HFT compose of monolithic CMOS pixel detectors using 30 $\mu m \times 30$ μm square pixels. The HFT is designed to measure the heavy flavor production by the measurement of displaced vertices and to do the direct topological identification of open charm hadrons.

CHAPTER 3

Di-electron production analysis

Di-leptons production is considered as a crucial probe of strongly interacting matter at high energy density matter [Ada05a] which is created by Relativistic Heavy Ion Collider (RHIC). Leptons are only affected by electro-magnetic interaction, can escape from the hot dense matter, and bring information of whole time evolution and dynamics of the medium. They are particularly attractive to study the in-medium properties of low-mass vector mesons, heavy flavor modification, and thermal radiation of the QGP.

In this chapter, the analysis details of the di-electron continuum in p+p and Au+Au collisions at $\sqrt{s_{\rm NN}}$= 200 GeV will be presented in parallel. The analysis procedures applied to two data sets are similar. The case in Au+Au collisions is more complicated than in p+p. The differences will be emphasized where they are presented.

3.1 Data Sets and Event Triggers

3.1.1 p+p collisions

In RHIC Run 9 (year 2009), STAR detector has set up a *minimum bias* trigger called VPDMB to select on *Non Singly Diffractive* (NSD) collisions from p+p collisions. The minimum bias events are triggered by the Vertex Position Detectors (VPD) covering $4.24 < |\eta| < 5.1$. A total of 305 million VPDMB triggered events were used for the analysis, corresponding integrated luminosity is about 12 nb^{-1}. Another trigger set of p+p collisions, called "*high-tower trigger*(HT)", select events which have deposited energy in a BEMC single tower (0.05×0.05 in $\eta - \phi$) larger than a certain threshold. Benefit from high-tower trigger, the sample of events which have high p_T (for example > 2 GeV/c)

tracks were enhanced. The events which have high p_T and high invariant mass of electron-positron pairs were also enriched by HT.

The luminosity of p+p collision was much higher than those in previous year. At highest luminosity of RHIC, the interaction rates can approach $\sim$ 10 MHz. Since year 2008, the TPC data acquisition (DAQ) rate has been upgraded to 1000 Hz. But the high interaction rates caused much more pile up events recorded in the p+p collisions. These pile up events don't have reasonable vertices. The VPD is used for rejecting those pile up events. The vertex z of real event should be correlated in VPD and TPC. Fig. 3.1 left panel shows correlation between the vz measured by TPC and VPD. The typical width of the Vz-vpdvz distribution is about 2.5 cm in p+p collisions which is shown in right panel, here vz is the vertex z measured by TPC, and vpdvz is the VPD measured value. By applying the vertex z difference cut, most of the pile up events can be rejected. So the Vz difference cut $|Vz - vpdvz| < 6$ cm removed most of the pile up events in p+p collisions. Table 3.2 shows the data sets used in p+p di-electron analysis.

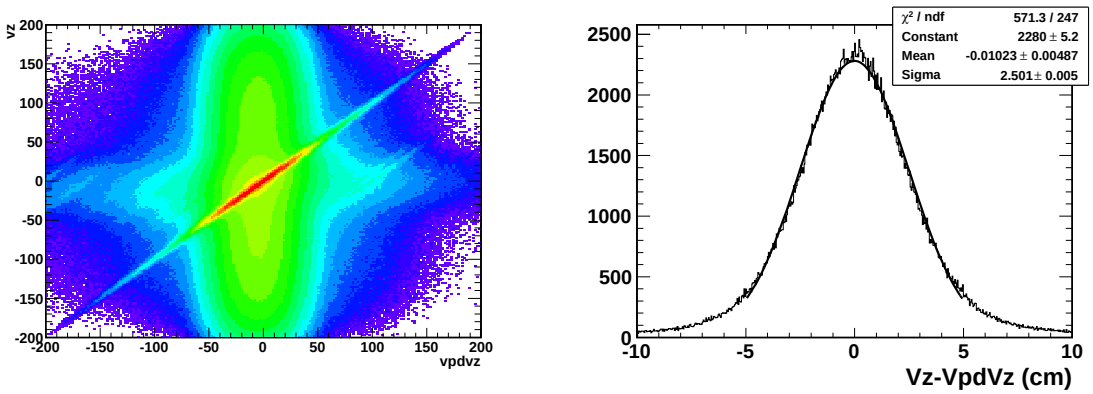

Figure 3.1: Left: Vz vs. VpdVz distribution. Right: Vertex z difference between TPC and VPD measured value in p+p collisions, fit by Gaussian function.

3.1.2 Au+Au collisions

The di-electron analysis in Au+Au at $\sqrt{s_{\rm NN}}$= 200 GeV based on the data sets taken in Run 10 (year 2010) at RHIC. Two sets of trigger were used to record the Au+Au events, one is *minbias* trigger, the other one is *central* trigger. In Au+Au collisions, the

Table 3.1: Centrality classes and corresponding $< N_{part} > < N_{coll} > < b >$ in Au+Au collisions at $\sqrt{s_{\rm NN}}$=200 GeV.

Centrality	$< N_{part} >$	$< N_{coll} >$	$< b > \ (fm)$	N_{evts}	N_{pairs}
0-10%	325.0±4.0	962.2±27.6	3.15±0.14	1.3×10^7	5.1×10^6
10-20%	235.6±8.8	608.8±31.1	5.66±0.23	1.5×10^7	5.8×10^6
20-30%	167.7±10.6	377.3±33.3	7.33±0.27	3.0×10^7	6.3×10^6
30-40%	115.9±11.1	223.8±30.5	8.69±0.31	3.0×10^7	3.5×10^6
40-50%	76.4±10.7	124.3±24.6	9.87±0.35	2.9×10^7	1.7×10^6
50-60%	47.7±9.4	64.4±17.7	10.92±0.40	2.7×10^7	7.6×10^5
60-70%	27.5±7.8	30.5±11.5	11.88±0.45	2.4×10^7	3.1×10^5
70-80%	14.4±5.3	13.4±6.13	12.81±0.50	1.8×10^7	9.0×10^4
0-80%	127.1±7.5	302.6±21.1	8.76±0.30	2.2×10^8	2.3×10^7

Table 3.2: The numbers of events after vertex cuts in p+p and Au+Au collisions.

Trigger	Sampled Luminosity	Vertex cut (cm)	N_{events}
p+p VPDMB	12 nb^{-1}	$\|Vz\| < 50$ && $\|Vz - vpdvz\| < 6$	107 M
p+p HT0 ($E_T > 2.6$ GeV)	1.873 pb^{-1}	$\|Vz\| < 200$	13 M
Au+Au MB	61.86 pb^{-1}	$\|Vz\| < 30$ && $\|Vz - vpdvz\| < 4$	220 M

charged particle reference multiplicity (refmult) measured at mid-rapidity ($|\eta| < 0.5$), for which the track is required to have number of TPC fit points (nFitPts)> 9 and distance-of-closest-approach (dca) < 3 cm, is used for centrality selection. The centrality classes for the data analysis were determined by the refmult cuts from the calculation of Glauber model [Mic07]. The centralities in this analysis are tabulated in the Table 3.1.

The pile up events take a very small fraction in the Au+Au collisions due to the collision rate are much lower than that in p+p collisions. The VPD has better time resolution about 30 ps since each channel has multiple hits in Au+Au collisions. Corresponding Vz difference, as shown in Fig. 3.2, is less than 1 cm. The numbers of events after vertex cuts in Au+Au 200 GeV were shown in Table 3.2.

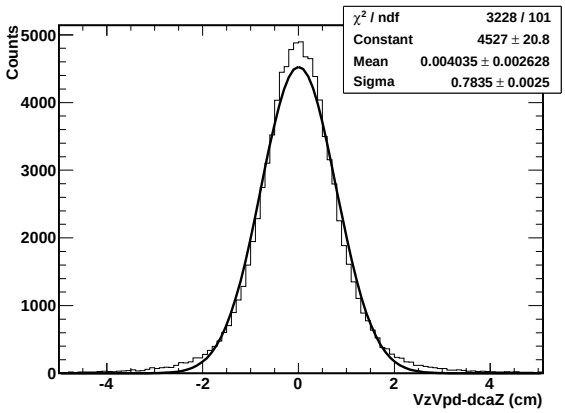

Figure 3.2: Vertex z difference between TPC and VPD measured value, fit by Gaussian function.

3.2 Electron Identification

The electron identification (eID) depends on a combination of TOF and TPC at STAR. By using the velocity (β) information from the TOF and energy loss (dE/dx) measured in the TPC, electrons can be identified up to p_T 3 GeV/c in p+p and Au+Au collisions. Due to the very small electron mass, electron can be separated from the slow hadrons by measuring the time of flight information. Fig 3.3 shows the high velocity cuts $|1/\beta - 1| < 0.03$ for the eID in the p+p collisions. In the Au+Au case, the mean of $1/\beta$ has a little dependence at low momentum (p). The cut form has a little bit difference, it was $|1/\beta - 1/\beta_{mean}| < 0.025$. The $1/\beta_{mean}$ is the mean of $1/\beta$ at each p bin measured from data. After applying the TOF eID cut, the electron and fast hadron are distributed in the different nσ_e region as a function of p_T. The nσ_e vs. p_T distribution after velocity cut is shown in Fig. 3.4. The nσ_e is defined as: Eq. 3.1:

$$n\sigma_e = \frac{1}{R} log(\frac{(dE/dx)_{measured}}{< dE/dx >_{electron}}), \tag{3.1}$$

where $(dE/dx)_{measured}$ is the measured mean dE/dx for a track, $< dE/dx >_{electron}$ is the expected mean dE/dx for Bichsel formula for electron with a given momentum, and R is the dE/dx resolution. All of the electron track selection were listed in the Table 3.3 except nσ_e cut. All candidates must be primary track, and the distance of closest approach

(DCA) between track and event vertex is required to avoid the admixture of tracks from secondary vertices. $nHitsFit$ is the number of hits using for track fitting, it is applied to avoid the multiple counting of split tracks. The maximum number ($nMax$) of $nHitsFit$ is 45 in the TPC. $nDedx$ is the number of points used for dE/dx calculation, this cut is applied to ensure the track has reliable dE/dx.

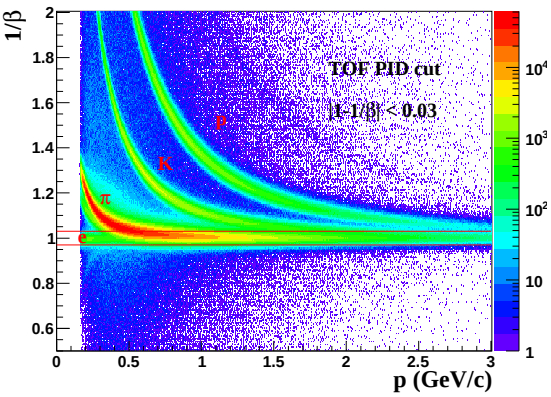

Figure 3.3: Inverse velocity $1/\beta$ vs. p in p+p collisions from the TOF at $|\eta| < 1$. The red line indicates the PID cut $|1/\beta - 1| < 0.03$.

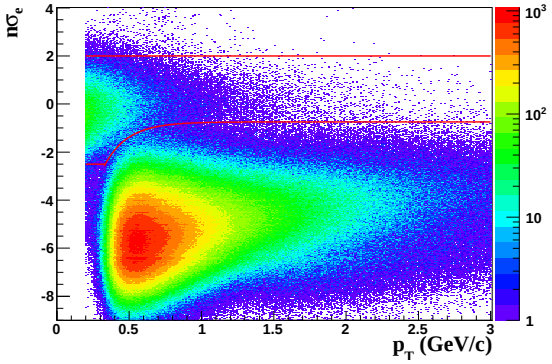

Figure 3.4: The normalized dE/dx distribution as a function of p_T with the cut of $|1/\beta - 1| < 0.03$ in p+p collisions.

Table 3.3: The PID cuts used in di-electrons analysis.

Cut	p+p VPDMB	Au+Au VPDMB
Primary track?	yes	yes
p_T	$p_T > 0.2\text{GeV}/c$	$p_T > 0.2\text{GeV}/c$
η	$\|\eta\| < 1$	$\|\eta\| < 1$
$nHitsFit$	$nHitsFit >= 25$	$nHitsFit >= 20$
$nDedx$	$nDedx >= 15$	$nDedx > 15$
$nHitsFit/nMax$	$nHitsFit/nMax >= 0.52$	$nHitsFit/nMax >= 0.52$
dca	$global\ dca < 1cm$	$global\ dca < 1cm$
$TOF\ cut$	$\|1/\beta - 1\| < 0.03$	$\|1/\beta - 1/\beta_{mean}\| < 0.025$

In the p+p collisions, a Gaussian+exponential function was applied to fit the nσ_e distribution in each p_T slices to select the electrons and estimate the background distribution. We fixed the higher nσ_e cut as 2. The lower nσ_e cut in each p_T slice has been selected at where the electron purity is about 99%. The 2-Gaussian fit matched the data not quite well. Another fit, exponential combine a Gaussian (exp+Gaus), was applied to describe

the nσ_e distribution. The 2-Gaussian and exp+Gaus(fixed width) fits were shown as Fig. 3.5, Fig. 3.6, Fig. 3.7, Fig. 3.8.

In the exp+Gaus fit, width and mean of Gaussian function were set as free parameters at first, then the widthes of all p_T slices were fit by a constant (shown in Fig 3.9), after that the nσ_e distribution was fit again with the fixed width. The reason of fixing the width is that the mean value could shift by the dE/dx calibration, but the width does not change much. The electron purity of two fits is shown in Fig. 3.10. Because the 2-gaus fit always overestimated the electron purity, the exp+Gaus fit were used to estimate the electron purity and nσ_e cut efficiency.

The Gaussian and exponential functions represent electron and hadron components individually. We derive the purity value and dE/dx cut efficiency on electron candidates as a function of $p_T$from the fits, as shown in the Fig. 3.4. The purity is defined as the ratio of the electron counts in the area of dotted Gaussian to the counts of all particles. The efficiency is defined as the ratio of the electron counts in the area of dotted Gaussian within an nσ_e range to the total electron counts in the whole area of dotted Gaussian without an nσ_e cut. The electron purity and efficiency of nσ_e cuts is shown in Fig. 3.11.

In the Au+Au collisions, the electron has more hadron contaminations even after high velocity cuts. The contamination is due to the high occupancy of TOF in the Au+Au collisions. If there are two tracks matched with same TOF cell, but the fast track (such as electron) was missed or not reconstructed in the TPC. The misidentified time of flight will be given to the slow hadron track. The nσ_e lower cut was above than a function $f(p) = 1.5p - 2.3$ at $p < 1$ GeV/c and -0.8 at $p > 1$ GeV/c, and the cut efficiency and purity were estimated by multi histogram fits. Each hadron component's histogram was obtained by a narrow mass cut by TOF.

The nσ_e cuts of p+p and Au+Au are shown as the two lines in the Fig 3.4 and Fig 3.12. The overall purity of electron is about 99% in p+p and 97% in Au+Au.

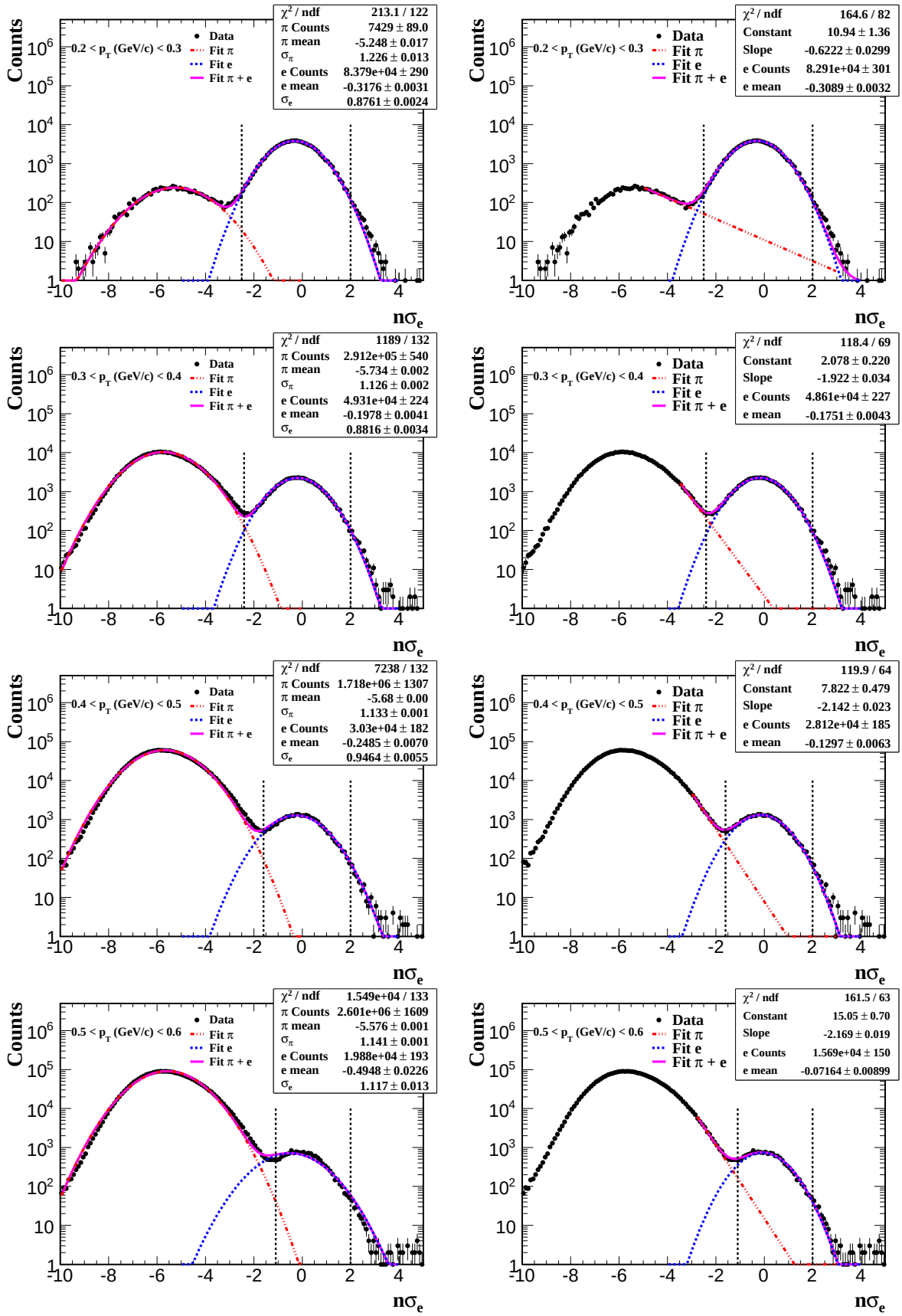

Figure 3.5: Left: 2-Gaussian fit, Right: exponential + Gaussian fit.

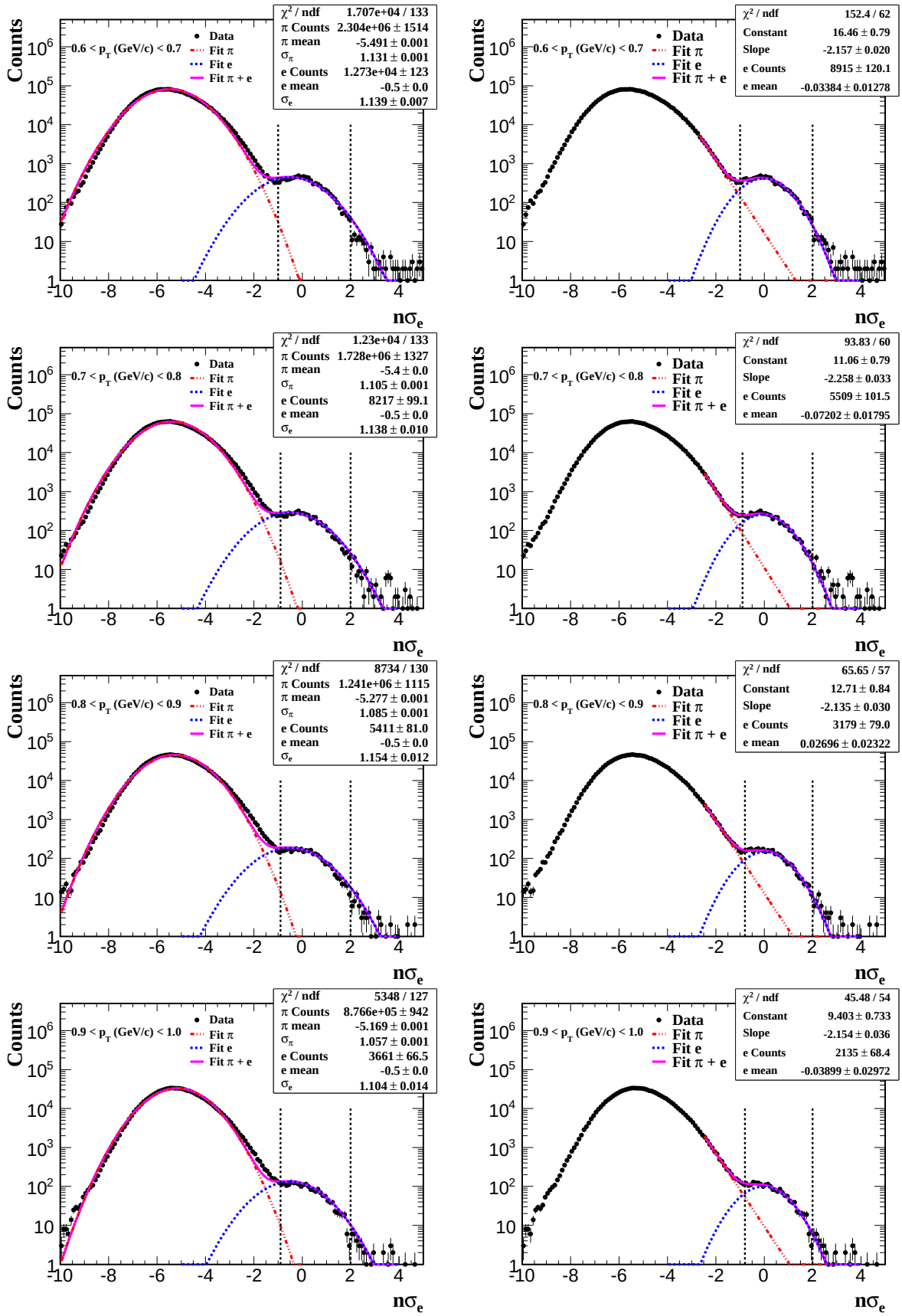

Figure 3.6: Left: 2-Gaussian fit, Right: exponential + Gaussian fit.

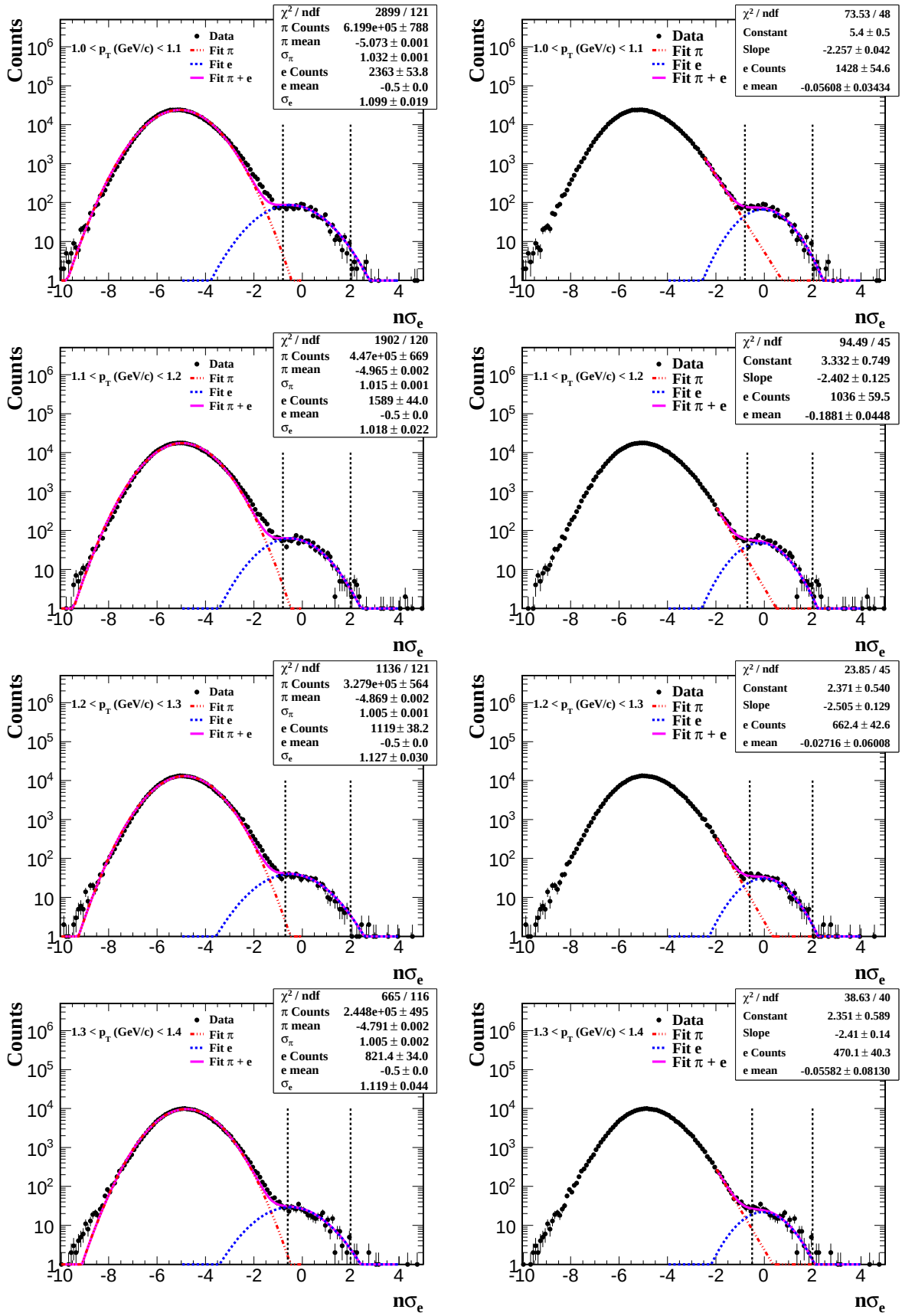

Figure 3.7: Left: 2-Gaussian fit, Right: exponential + Gaussian fit.

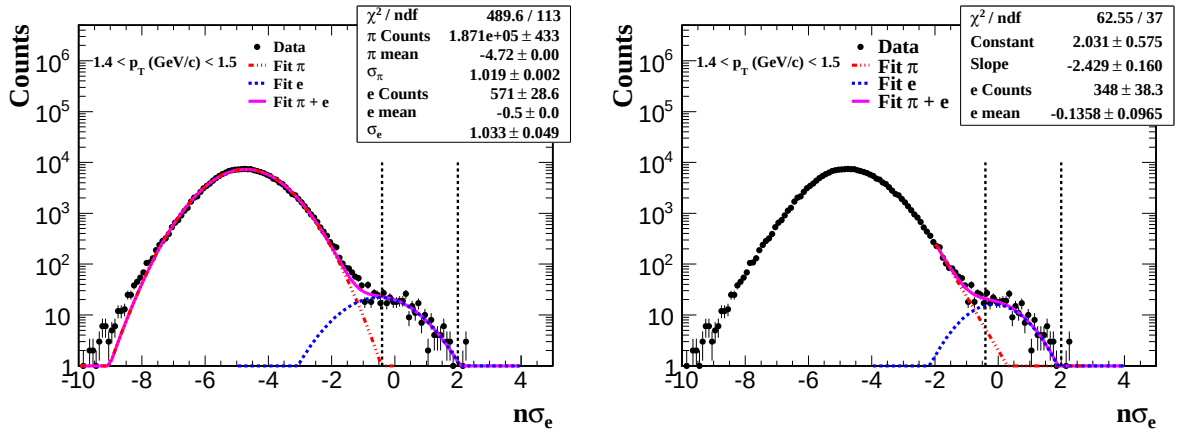

Figure 3.8: Left: 2-Gaussian fit, Right: exponential + Gaussian fit.

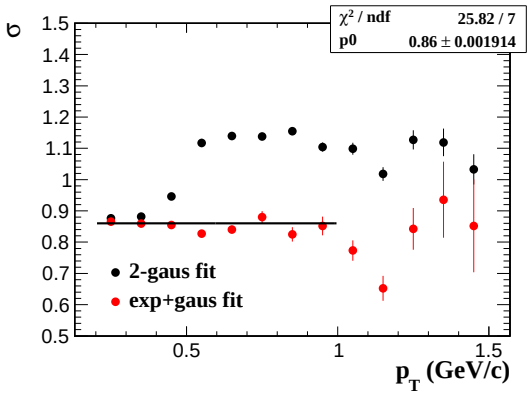

Figure 3.9: $n\sigma_e$ width fit.

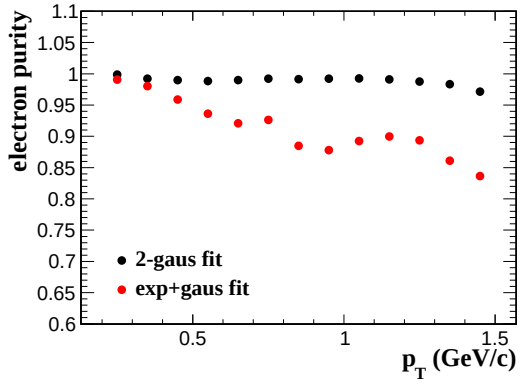

Figure 3.10: Electron purity estimation from two kinds of fit.

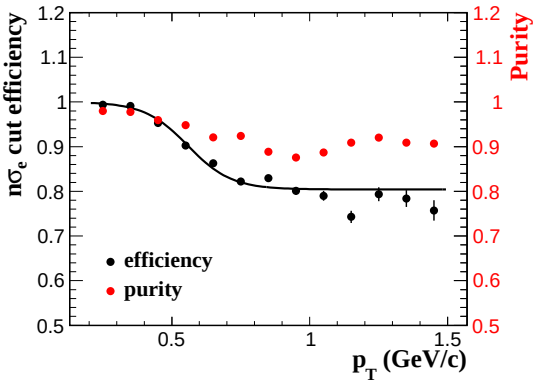

Figure 3.11: $n\sigma_e$ cuts efficiency and the purity after fixing width fit for electron candidates as a function of p_T at $|\eta| < 1$ in p+p.

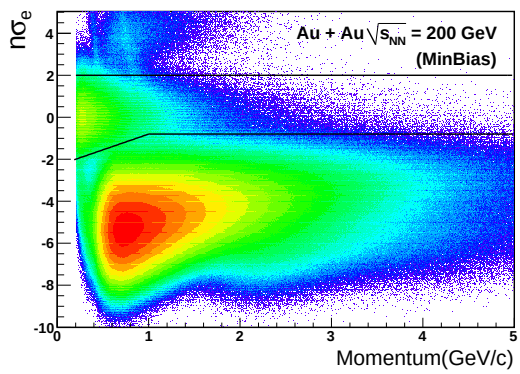

Figure 3.12: The normalized dE/dx distribution as a function of p_T with the cut of $|1/\beta - 1/\beta_{mean}| < 0.03$ in Au+Au collisions.

3.3 Pair reconstruction

With a high purity for the electron samples, the e^+e^- are combined to reconstruct the invariant mass distributions (M_{ee}) marked as *foreground* pairs which include like sign pairs and unlike sign pairs in same events. The invariant mass of pairs m_{ee} are calculated as:

$$m_{ee}^2 = (E_+ + E_-)^2 - ((\overrightarrow{p})_+ + (\overrightarrow{p})_-)^2, \tag{3.2}$$

with $E_\pm = \sqrt{\overrightarrow{p}_\pm^2 + m_e^2}$, $m_e = 0.511$ MeV/c, and the momentum $\overrightarrow{p}_\pm$ was measured with TPC. The electron candidates are required to be in the range of $|\eta| < 1$ and $p_T > 0.2$ GeV/c while the resulting ee pairs are required to be in the rapidity range of $|y_{ee}| < 1$.

The signal pairs consist of light flavor hadron decays, heavy flavor hadron decays, and Drell-Yan contributions. The background in the unlike sign pairs are dominated by random combinatorial background and cross pairs. The cross pair is the case that two partner tracks come from different parents but same source (*e.g.* $\pi^0 \to \gamma e^+e^-$, one track is from π^0, the other track is from the converted γ). The random combinatorial background is just combined by electrons and positrons from different sources. These two kinds of background can be reproduced by like sign pairs. For reducing the statistical errors, mixed event technique was used to increase the statistics of combinatorial background at higher mass region.

3.3.1 Background analysis

As mentioned in Sec. 3.3, two methods are used for background reconstruction, based on like-sign and mixed-event techniques.

In the like-sign technique, the electron pairs with the same charge sign are reconstructed from the same event. It does not contain any signal pairs and reproduces a direct measurement of correlated pairs and combinatorial background. While the unlike and like sign pairs had equal acceptance and efficiency, the signal pairs can be directly obtained through the subtraction of like sign pairs from unlike sign pairs. Here the like

sign is using the geometrical mean of e^+e^+ and e^-e^- pairs in real events:

$$\langle N_{\pm\pm}\rangle = 2\sqrt{\langle N_{++}\rangle\langle N_{--}\rangle}, \tag{3.3}$$

The opposite sign tracks are projected to different ϕ directions in magnetic field in the detectors. The acceptance difference between the like and unlike sign need to be estimated by using the mixed event method, and also need to be corrected for the background subtraction.

The correction of acceptance difference between like and unlike sign can be estimated from the difference of mixed like sign and mixed unlike sign pairs. Since the discrepancy between them only come from the detector acceptance. The acceptance correction factor is evaluated as:

$$f_{acpt}(m_{ee}, p_T) = \frac{B_{+-}(m_{ee}, p_T)}{\sqrt{B_{++}(m_{ee}, p_T)B_{--}(m_{ee}, p_T)}}\ , \tag{3.4}$$

Where $B_{+-}(m_{ee}, p_T)$, $B_{++}(m_{ee}, p_T)$ and $B_{--}(m_{ee}, p_T)$ are the numbers of e^+e^-, e^+e^+ and e^-e^- pairs in mixed-event, respectively. The mixed-event technique will be detailed below.

In order to have a higher statistical accuracy, the mixed event background was reproduced as well. The electrons from different events were combined to reconstruct the structure of combinatorial background. To keep the same structure, event samples are split to event pools of centrality, Vz, and reaction plane. In order to ensure the mixed events have similar acceptance, we only mix events, which have collision vertices within 5 cm of each other along the beam line direction.

3.3.2 Normalization

To subtract the combinatorial background by event mixing technique, the mixed event background should be normalized to the same amplitude of real background. The like sign background has same quantity as the number of the real background. So it can be used for normalizing the mixed event. In STAR acceptance, the mixed event subtracted

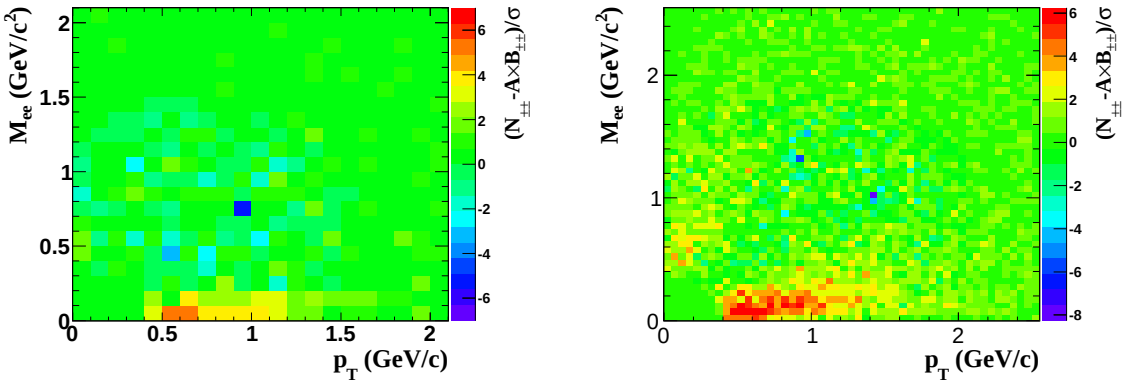

Figure 3.13: The difference between real and mixed-events like-sign distributions divided by its standard deviation $(N_{\pm\pm} - A \times B^{comb}_{\pm\pm})/\sigma_{N_{\pm\pm}}$ in p+p data (left) and in PYTHIA [SMS06] (right). The background $B^{comb}_{\pm\pm}$ is normalized to the foreground $N_{\pm\pm}$ in the normalization range $0.4 < M_{ee} < 1.5$ GeV/c^2, A is the normalization factor.

like sign spectrum is shown in the Fig. 3.13. The $(N_{\pm\pm} - A \times B^{comb}_{\pm\pm})/\sigma_{N_{\pm\pm}}$ in the figure indicates the discrepancy in each mass and p_T bin. It shows that the difference between mixed event and like sign is dominant by the cross pair located at very low mass region ($M_{ee} < 0.3$ GeV/c^2). At last the normalization area is chosen as: $0.4 < M_{ee} < 1.5$ GeV/c^2 in p+p, $0.7 < M_{ee} < 3.0$ GeV/c^2 in Au+Au.

The PYTHIA calculation shows a weak correlation at away side due to the correlated electron pairs from jet, but the data do not. The mass of correlated pairs depends on the opening angle of two tracks, the random combinatorial background has a flatten distribution as function of $\Delta\phi$. But the correlated pairs background, which come from jet, have a correlation in near side and away side. The ratio of like sign to mixed event background as a function of mass, also indicates the two background shapes are similar at mass > 0.4 GeV/c^2, which is shown in the Fig. 3.14 panel (a). HT events in p+p were used to increase the background statistics at high mass region. The ratios in HT events is shown in panel b) in Fig. 3.14. Fig. 3.14 (c) shows the distribution of the difference of the azimuthal angles ($\Delta\phi$) of the two electrons in the unlike-sign, like-sign and mixed-event pairs. The difference between like-sign and mixed-event pairs at low $\Delta\phi$ range can be attributed to cross-pair contributions. By selecting $M_{ee} > 1$ GeV/c^2, the $\Delta\phi$ distributions of like-sign and mixed-event pairs match nicely with each other as shown in Fig. 3.14 (d),

indicating that mixed-event background subtraction is valid in the corresponding mass region. For minimum-bias events, mixed-event background with high statistics is used for $M_{ee} > 0.7$ GeV/c^2.

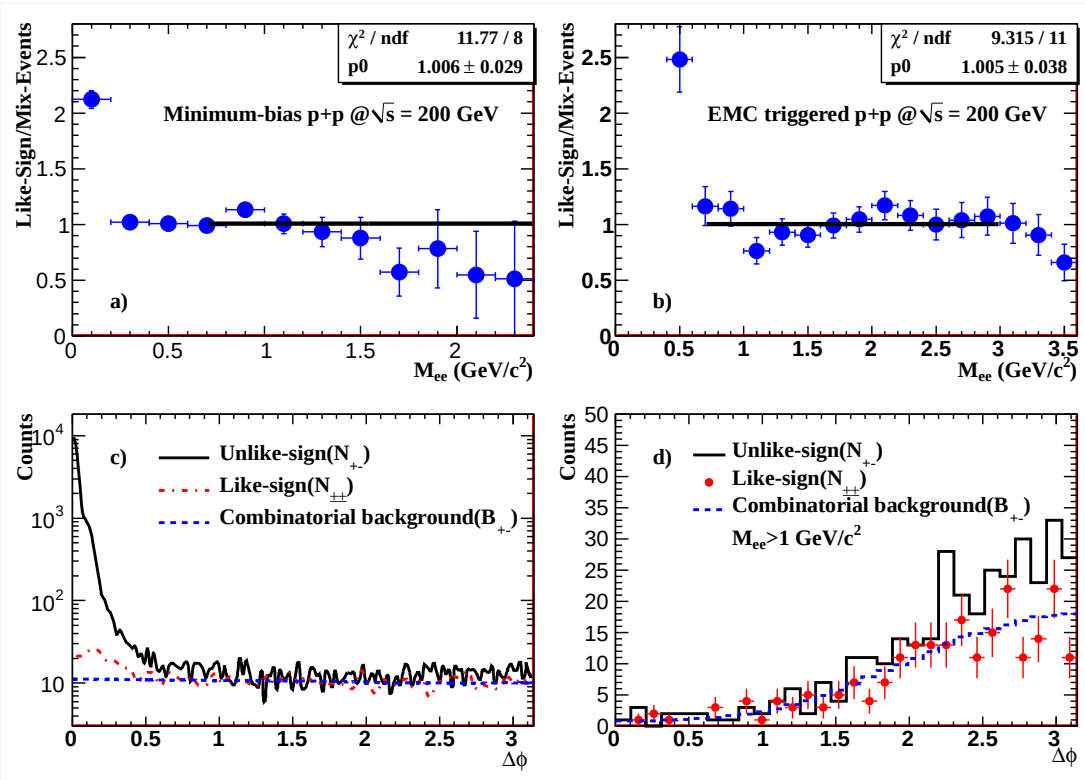

Figure 3.14: Panel (a): The ratio of like-sign over mixed-event distributions in minimum-bias p+p collisions. Panel (b): The ratio of like-sign over mixed-event distributions in EMC triggered p+p collisions. Panel (c): The $\Delta\phi$ distribution of the difference of the azimuthal angles. of the two electrons in the unlike-sign, like-sign and mixed-event pairs in minimum-bias p+p collisions. Panel (d): The $\Delta\phi$ distributions of like-sign and mixed-event pairs by selecting $M_{ee} > 1$ GeV/c^2in minimum-bias p+p collisions. Errors are statistical.

For minimum-bias events, at $M_{ee} > 0.7$ GeV/c^2, the unlike sign pairs was subtracted by the normalized mixed event background due to more statistics of mixed event. Lower than 0.7 GeV/c^2, it was subtracted by like sign pairs corrected with acceptance factor f_{acpt}. The mass distributions of unlike sign, like sign, and normalized mixed event in p+p are shown in Fig. 3.15. The ratios of over background signal after two different subtraction in p+p and Au+Au are shown in Fig. 3.16. The e^+e^-mass distributions after the background subtraction for p+p and Au+Au are represented in Fig. 3.17. Alternatively, we subtract

the like-sign background in the whole mass region. The difference in the yields of di-electron continuum from the two methods is taken as systematic uncertainties.

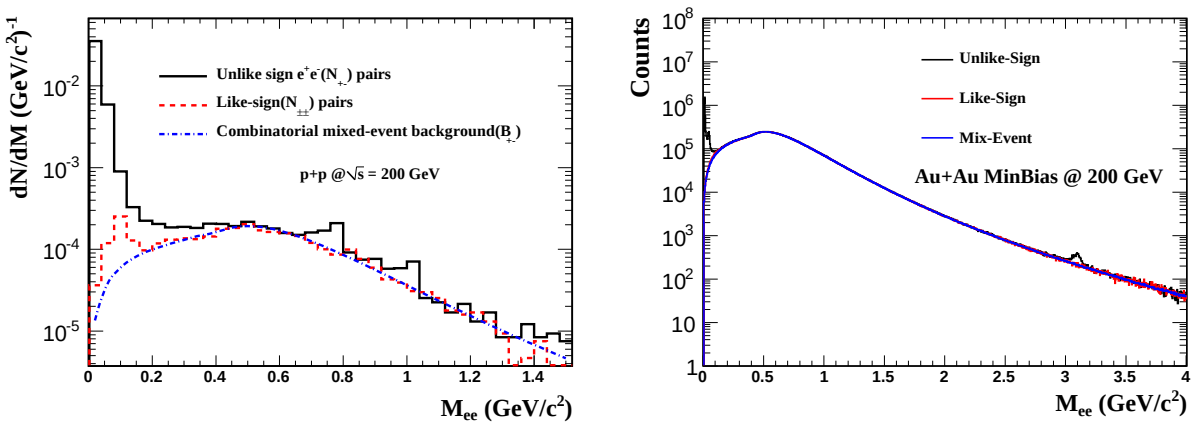

Figure 3.15: The e^+e^-pair invariant mass distributions for unlike-sign foreground, like-sign and mixed-event background. Left is for p+p collisions, right is for Au+Au collisions.

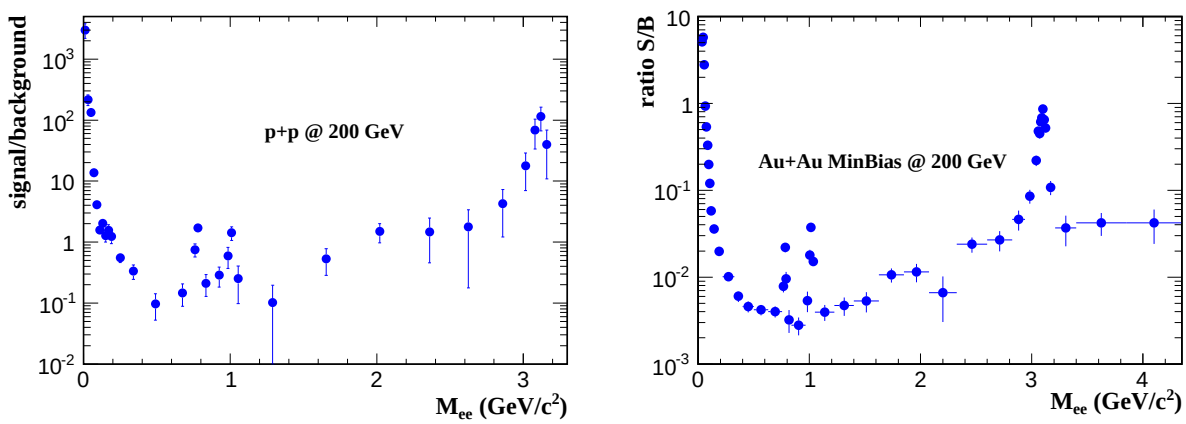

Figure 3.16: The signal over background ratio. Left is for p+p collisions, right is for Au+Au collisions.

3.4 Efficiency and Acceptance

For the di-electron continuum, the raw yield of di-electron signal has to be corrected for the efficiency within the STAR acceptance of $|y_{e^+e^-}|<1$, $|\eta_e|<1$ and $p_T(e)>0.2$. The pair detection efficiency within STAR acceptance was calculated by single electron efficiency from TPC+TOF. The single electron efficiency includes the TPC tracking efficiency, TOF

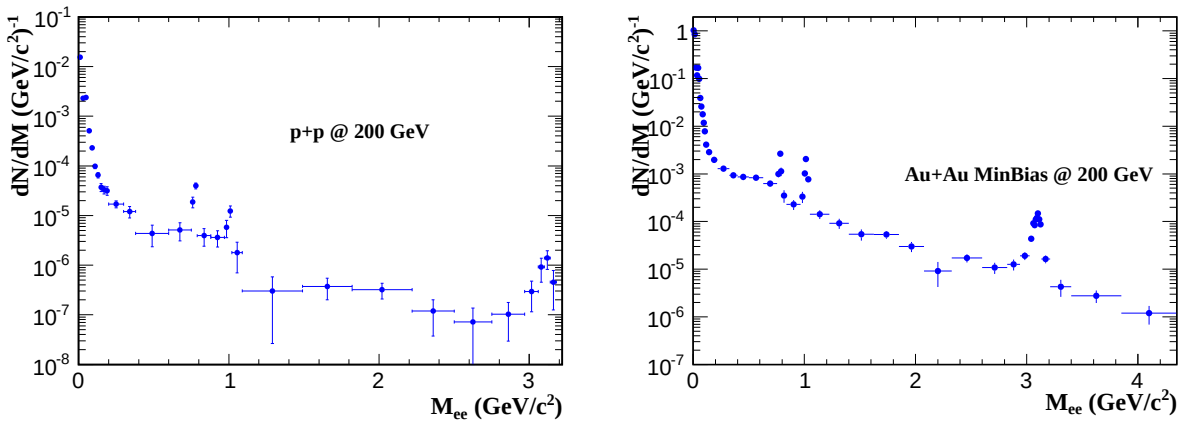

Figure 3.17: Background-subtracted mass spectrum for dielectrons. Left is for p+p collisions, right is for Au+Au collisions.

acceptance and detector response, the dE/dx efficiency, PID cut efficiency ($1/beta$ and nσ_e cut), as listed at below:

- TPC tracking efficiency: track reconstruction efficiency include acceptance.
- TOF efficiency: include TOF matching efficiency and acceptance.
- $|1/\beta - 1| < 0.03$ cut efficiency.
- number of dE/dx fit points ($nDedx$) cut efficiency.
- n$\sigma_e$cut efficiency.

The TPC tracking efficiency is obtained by embedding the electron tracks to a real event and run them through GSTAR [Lon] (the framework software package to run the STAR detector simulation using GEANT [Ago03, All06] and TRS [Lon] (the TPC Response Simulator)). The real event with embedded electron tracks is called simulated event. It passed through the standard STAR reconstruction chain, then we can have the reconstructed information of the embedded tracks. The TPC tracking efficiency is calculated by dividing the number of reconstructed tracks by the input number of embedded tracks, as following function:

$$\varepsilon_{TPC} = \frac{N_{rc}}{N_{emb}}, \tag{3.5}$$

N_{rc} is the number of reconstructed electron tracks with associated embedding tracks, and N_{emb} is the number of embedded electron tracks.

The other efficiencies were calculated from data. The TOF efficiency is defined as the number of tracks with TOF matched divided by all of the TPC tracks passing the track quality cuts, and as function:

$$\varepsilon_{TOF} = \frac{N_{TOF}}{N_{TPC}}, \tag{3.6}$$

where N_{TOF} is the number of TOF matched tracks, and N_{TPC} is the number of TPC tracks passing quality cuts. The efficiency of TOF PID cut $|1/\beta - 1| < 0.03$, is calculated by using an enriched sample of pion tracks. The efficiency difference between pion and electron is about 2%. We corrected it in final calculation. Usually, we are using gaussian fit to $1/\beta$ to determine the efficiency.

The *nDedx* cut efficiency also come from real data because the inefficiency associated with *nDedx* quantities are currently not well simulated in STAR [Gon]. To study the *nDedx* cut efficiency, the tracks were selected by two sets of quality cuts, one is by applying all of the quality cuts except the *nDedx* cut, the other one is with all of the cuts. So the inefficiency of the *nDedx* cut is obtained by comparing the number of tracks with and without the *nDedx* cut.

The efficiency of TPC nσ_e cut, is determined by the fit method of PID. In p+p, we are using the exp+Gaus to fit the nσ_e distribution, while in Au+Au, we are using multi histograms to fit. It will be discussed in Sec. 3.4.1 and Sec. 3.4.2 separately.

3.4.1 In p+p collisions

The TPC track quality cuts are listed in Table 3.3. The *nDedx* cut efficiency as a function of p_T is shown in Fig. 3.18. A constant fit gave a value of 97% for *nDedx* efficiency.

The TOF matching efficiency doesn't have a strong p_T dependence, but has a particle species dependence, electron efficiency is slightly higher than the pion efficiency. The

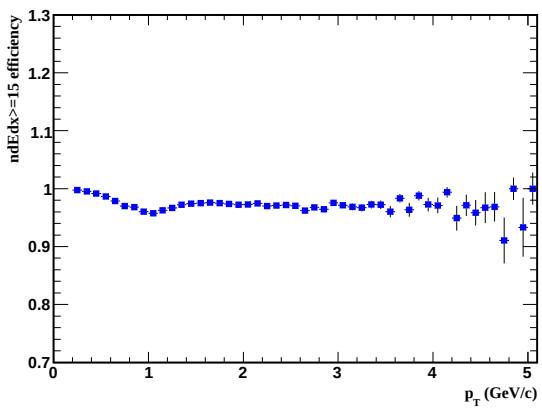

Figure 3.18: *nDedx* cut efficiency in p+p at 200 GeV.

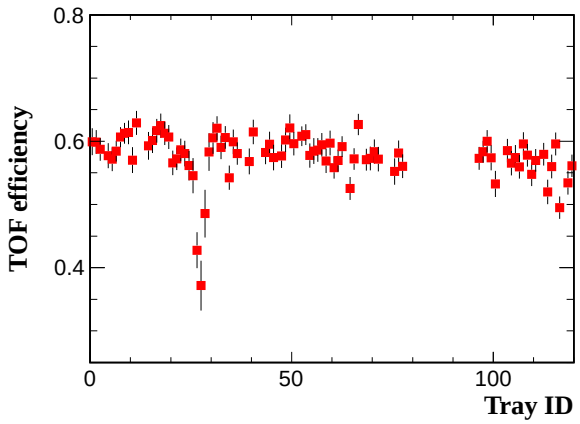

Figure 3.19: The TOF efficiency as a function of tray ID. Tray 1-60 is at $\eta > 0$, with tray 1 covering 75 to 80 degree in azimuth, tray 2 covering 81 to 86, and so on. Tray 61-120 is $\eta < 0$, with tray 61 covering 105 to 110 degree in azimuth, tray 62 covering 111 to 116, and so on. The gaping hole corresponds to the 28% trays that still needed to be installed in 2009.

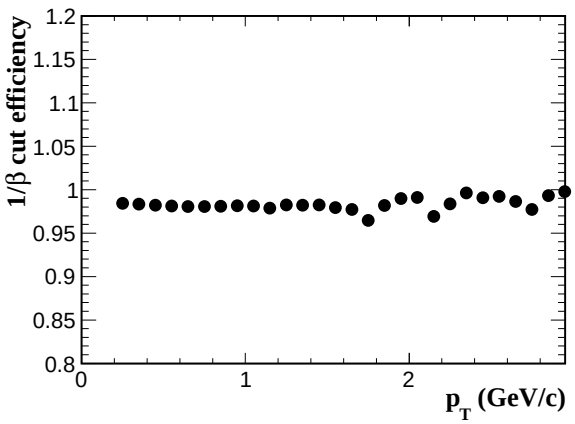

Figure 3.20: $1/\beta$ cut efficiency in p+p at 200 GeV.

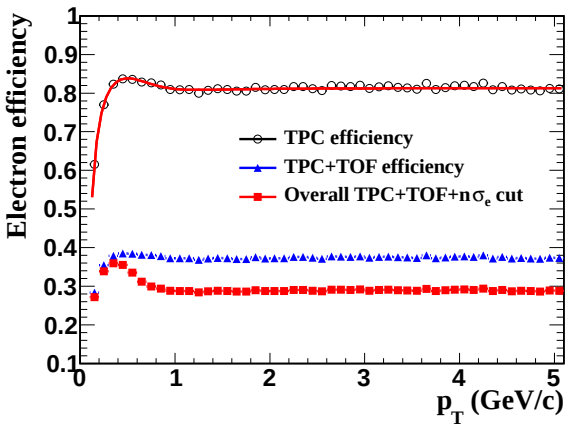

Figure 3.21: The efficiency for single electrons as a function of p_T in p+p collisions at $\sqrt{s_{\rm NN}}$= 200 GeV.

efficiency for kaon and proton are significantly lower than that for pion at low p_T due to weak decay and scattering effect. But difference between electron and pion is quite small. It is hard to get clean electron sample at full p_T range. So after the track quality cuts, we used pion sample with a TPC PID cut $|n\sigma_\pi| < 0.5$ to obtain a $p_T$dependent TOF matching efficiency calculation in Au+Au. In p+p, we use $|n\sigma_e| < 0.5$ cut to calculate the TOF matching efficiency for electron in the overall p_T range. The p_T dependance of electron TOF matching efficiency is negligible in p+p. The VPDMB triggered events had pile-up effect due to high luminosity in p+p. The TOF efficiency will be reduced 2-4% by the pile-up tracks. In order to obtain the correct TOF efficiency, we used pp2pp VPDMB triggered events to do the efficiency calculation. The pp2pp VPDMB triggered event is same trigger sets as VPDMB trigger but was running at a low luminosity situation, therefore the pile-up effect in this kind event is negligible. The TOF efficiency as a function of Tray ID is shown in Fig. 3.19. Tray 1- 60 is at $\eta > 0$, with tray 1 covering 75 to 80 degree in azimuth, tray 2 covering 81 to 86, and so on. Tray 61-120 is $\eta < 0$, with tray 61 covering 105 to 110 degree in azimuth, tray 62 covering 111 to 116, and so on.

The nσ_e efficiency is already shown in the Fig. 3.11. The TPC efficiency as function of p_T with all the track quality cuts except $nDedx$ is shown as circles in Fig. 3.21. After weighted the TOF efficiency in each tray, the combined TPC and TOF efficiency is shown as the blue triangles. With additional TPC PID cut the efficiency is shown as the red squares.

The single electron efficiencies include the TPC tracking efficiency and TOF matching efficiency in Au+Au are shown in Fig. 3.23.

3.4.2 In Au+Au collisions

The track quality cuts in Au+Au had some minor difference compared to those in p+p. But the efficiency calculation method is same. The efficiencies calculated from data including $nDedx$ cut efficiency ($nDedx > 15$), $1/\beta$ cut efficiency and nσ_e cut efficiency are shown in Fig. 3.22. Fig. 3.23 shows the TPC tracking and TOF matching efficiency for

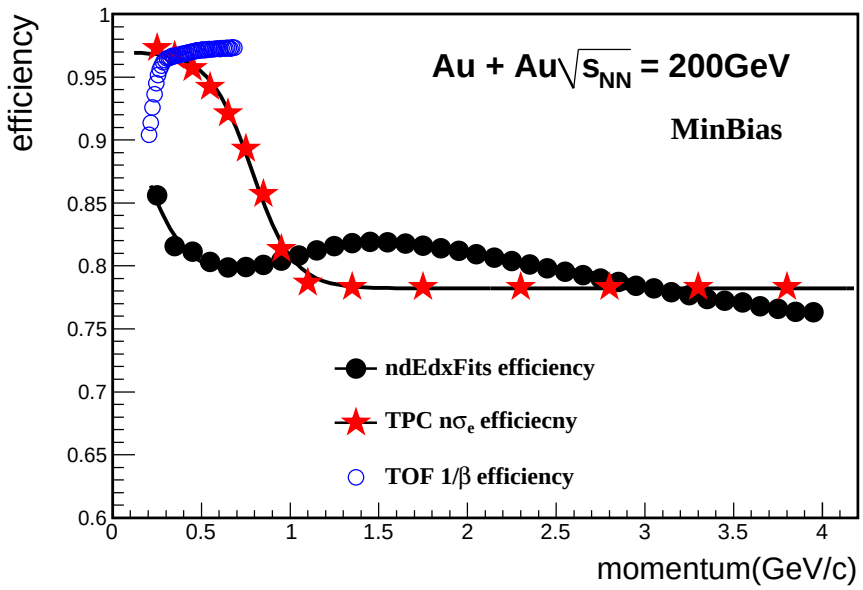

Figure 3.22: The efficiencies calculate from data in Au+Au collisions. Black dots represent *nDedx* cut efficiency. Open circles are The TOF $1/\beta$ efficiency at low momentum. Red stars show the nσ_e cut efficiency.

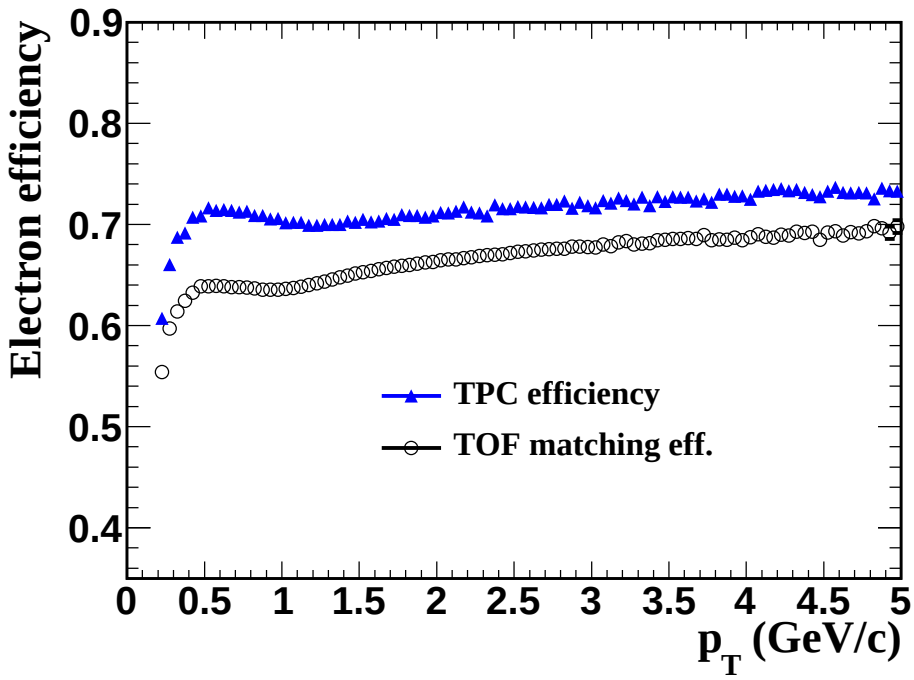

Figure 3.23: The efficiency for single electrons as a function of p_T in the pseudo-rapidity of $|\eta| < 1$ in Au+Au collisions at $\sqrt{s} = 200$ GeV . Blue triangle is the TPC tracking efficiency. Open circles represent TOF matching efficiency.

single electrons as a function of p_t in the pseudo-rapidity of $|\eta| < 1$ in Au+Au collisions at $\sqrt{s} = 200$ GeV.

The nσ_e distribution was fitted by multi nσ_e histograms, each nσ_e histogram represents one particle or misidentified component. The shape of each nσ_e distribution is obtained by a very pure invariant mass cut from TOF. The detail has been discussed in the Sec. 3.2.

3.4.3 Pair detection efficiency

The electron pair efficiency is determined by a simulation folding method. In the simulation folding method, we use the decay kinematics of the di-electron sources and sample with a flat η and a flat ϕ distribution, after that we sample the measured p_T distribution for mesons and heavy flavor parents. The meson momentum spectra are collected from previous publications at RHIC energy. For heavy flavor components, the non-photonic electron p_T spectra and PYTHIA [SMS06] were used for sampling. The details will be discussed in Sec. 3.5.

The efficiency factor for di-electron continuum within the STAR acceptance, which is $y_{e^+e^-} < 1$, $|\eta_e| < 1$, and $p_T(e) > 0.2$ GeV/c, is obtained by two steps: we use GEANT simulations to obtain cocktail A within STAR acceptance as the procedure described in Sec. 3.5. For cocktail A the efficiency factors for single electrons are set to 100%, and the result is shown by the solid line in Fig. 3.24 (a). Cocktail B is obtained from GEANT simulations with proper efficiency factors including the TPC tracking, TOF acceptance and response, and dE/dx cut for single electrons as described above, and shown as the dashed line in Figure 3.24 (a). The ratio of these two is the efficiency factor for the di-electrons and is shown in Fig. 3.24 (b) in p+p collisions at $\sqrt{s} = 200$ GeV. Fig. 3.24 shows the Au+Au results.

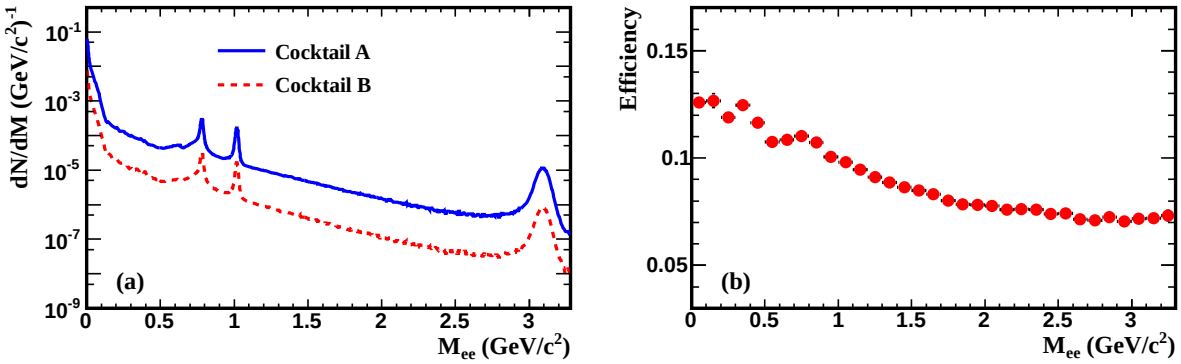

Figure 3.24: (a) The M_{ee} distribution within STAR acceptance with the efficiency factors for single electrons set to be 100% (solid line) or be the correct (dashed line). (b) The efficiency of di-electron continuum as a function of M_{ee} within the STAR acceptance, which is $|y_{e^+e^-}|<1$, $|\eta_e|<1$, and $p_T(e)>0.2$ GeV/c, in p+p collisions at $\sqrt{s}$ = 200 GeV. .

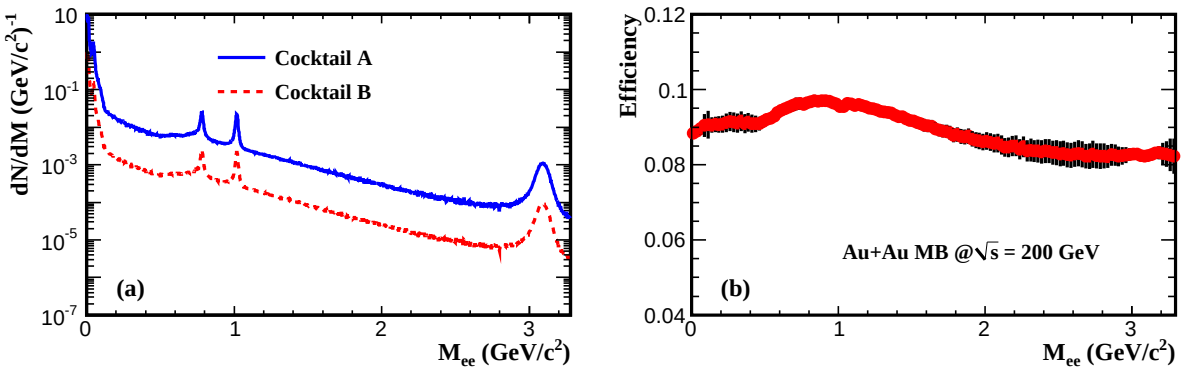

Figure 3.25: (a) The M_{ee} distribution within STAR acceptance. The descriptions for lines are same as Fig. 3.24. (b) The efficiency of e^+e^-pair efficiency in Au+Au at $\sqrt{s_{\rm NN}}$= 200 GeV.

3.5 Cocktail simulation

The di-electron signals come from light flavor hadron and heavy flavor hadron decays. To reproduce meson sources, we generate Monte-Carlo (MC) parent particles which can contribute to di-electrons and let them decay with the expected dynamics. For the MC particle, we sample its transverse momentum, with a measured p_T distribution, flat rapidity, and flat azimuth distribution. After it decays in a simulated process, electron pairs can be reconstructed by daughter electrons which are weighted with the efficiency and applied acceptance cuts. For heavy flavor source, we used PYTHIA as the generator. The non-photonic electron (NPE) measurement [Aga11a] and ratio of B meson decayed electrons to B and D meson decayed electrons [Agg10] are used to constrain the PYTHIA settings to generate $c \to e$ and $b \to e$ yields. Since the $b \to e$ is still unknown, we used the PYTHIA 6.416 with CTEQ5L parton distribution function [Lai00] to generate it. Then we constrain the yields to match with the ratio of B decayed electrons to B+D decayed electrons. Once the PYTHIA settings are determined, the $c\bar{c} \to ee$ component can be reconstructed from the PYTHIA p+p minbias events. By comparing the reconstructed and input electron pairs, the efficiency as function of mass can be obtained. After the efficiency correction, the e^+e^-signal can be directly compared with the e^+e^-simulated cocktail.

3.5.1 Light flavor meson

For light flavor mesons, the first input is the rapidity density dN/dy of mesons which is determined by a Tsallis blast-wave (TBW) [Tan09] fit to published data:

$$\frac{dN}{m_T dm_T} \propto m_T \int_{-Y}^{+Y} cosh(y)dy \int_{-\pi}^{+\pi} d\phi \int_0^R rdr \times(1 + \frac{q-1}{T}(m_T cosh(y)cosh(\rho) - p_T sinh(\rho)cos(\phi)))^{-1/(q-1)} \tag{3.7}$$

Where $\rho = \tanh^{-1}(\beta_s(r/R)^n)$ is the flow profile growing as n-th power from zero at the center of the collisions to β_s at the hard-spherical edge(R) along the transverse radial

direction (r), and $\beta = \beta_s/(1+1/(n+1))$ is the average flow velocity, here n=1. For p+p collisions, $\beta = 0$, $T = 0.0964 \pm 0.004$ GeV, and $q-1 = 0.0926 \pm 0.003$. For Au+Au minbias 0-80%, $\beta = 0.466c$, $T = 0.1170 \pm 0.0019$ GeV, and $q-1 = 0.0416 \pm 0.0013$. The invariant yields as function of p_T for all the mesons are shown in Fig. 3.26 and Fig. 3.27. The fit shows the meson productions can be described by the TBW model. Accordingly, the TBW fit is extended to some mesons which does not have measurement yet (for example η'). The other two inputs are rapidity and azimuthal angle, they are using flat distributions within (-1,1) and ($-\pi$,π).

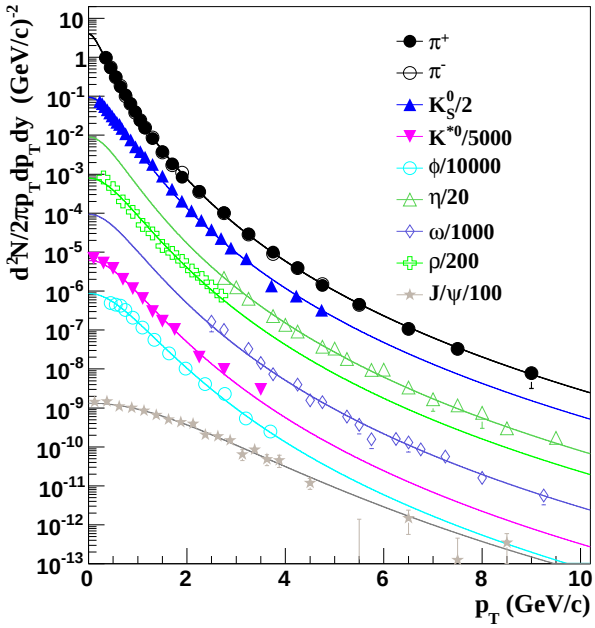

Figure 3.26: The Tsallis Blast-Wave fit for meson measurements in p+p at 200 GeV.

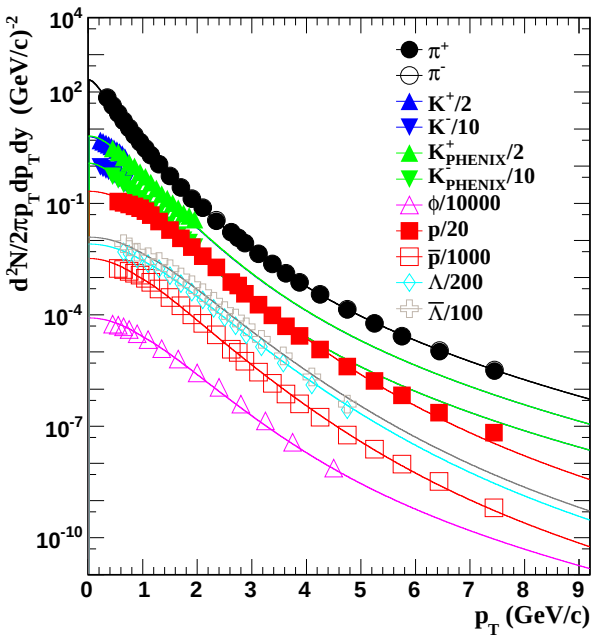

Figure 3.27: The Tsallis Blast-Wave fit for meson and baryon measurements in Au+Au at 200 GeV.

The yields of π^0, η, η', ρ, ω, ϕ, and J/ψ in p+p and Au+Au are given in the Tab. 3.5 and Tab. 3.6. They are extracted by integrated the fits over all p_T. The data uncertainties and references are also given in the tables.

Once we have the meson yields and p_T spectra, the decay kinematics will determine the decayed di-electron spectrum. For two body decays, the width of ω, ϕ, and J/ψ are quite small comparing to the mass smearing of detector momentum resolutions. Their mass width are from the number of PDG [Nak10].

For the Dalitz decays of π^0, η and η', we use the formula below:

$$\frac{dN}{dm_{ee}} \propto \sqrt{1-\frac{4m_e^2}{m_{ee}^2}}(1+\frac{2m_e^2}{m_{ee}^2})\frac{1}{m_{ee}}(1-\frac{m_{ee}^2}{M_h^2})^3|F(m_{ee}^2)|^2. \tag{3.7}$$

In which, m_e is the electron mass, m_{ee} is the di-electron mass, M_h is the mass of the hadron which decays into di-electrons. $F(m_{ee}^2)$ is the electro-magnetic transition form factor. For the Dalitz decays of vector mesons ω and ϕ ($A \to Be^+e^-$), the formula is below:

$$\frac{dN}{dm_{ee}} \propto \sqrt{1-\frac{4m_e^2}{m_{ee}^2}}(1+\frac{2m_e^2}{m_{ee}^2})\frac{1}{m_{ee}}[(1+\frac{m_{ee}^2}{M_A^2-M_B^2})^2-\frac{4M_A^2m_{ee}^2}{(M_A^2-M_B^2)^2}]^{3/2}|F(m_{ee}^2)|^2 \tag{3.8}$$

In which the M_A and M_B are the mass of particle A and B, respectively. The form factor is parameterized below:

$$F(m_{ee}^2) = \frac{1}{1-m_{ee}^2\Lambda^{-2}} \tag{3.9}$$

This is used for most of the Dalitz decays except for $\eta' \to \gamma e^+e^-$. For η', the parametrization is from [Lan85]:

$$|F(m_{ee}^2)|^2 = \frac{1}{(1-m_{ee}^2\Lambda^{-2})^2+\Gamma_0\Lambda^{-2}} \tag{3.10}$$

The Γ_0 is 1.99×10^{-2} GeV^2. The Λ parameters are listed in Table 3.4. The $\rho^0 \to e^+e^-$ line shape is below:

$$\frac{dN}{dm_{ee}dp_T} \propto \frac{m_{ee}M_\rho\Gamma_{ee}}{(M_\rho^2-m_{ee}^2)^2+M_\rho^2(\Gamma_{\pi\pi}+\Gamma_{ee}\Gamma_2)^2} \times PS, \tag{3.11}$$

$$\Gamma_{\pi\pi} = \Gamma_0\frac{M_\rho}{m_{ee}}(\frac{m_{ee}^2-4M_\pi^2}{M_\rho^2-4M_\pi^2})^{3/2}, \tag{3.12}$$

$$\Gamma_{ee} = \Gamma_0\frac{M_\rho}{m_{ee}}(\frac{m_{ee}^2-4m_e^2}{M_\rho^2-4m_e^2})^{1/2}, \tag{3.13}$$

$$PS = \frac{m_{ee}}{\sqrt{m_{ee}^2 + p_T^2}} e^{-\frac{\sqrt{m_{ee}^2+p_T^2}}{T}}. \tag{3.14}$$

In which M_ρ is 776 MeV, M_π is the π mass, Γ_0 is 149 MeV, Γ_2 is the B.R. of $\rho^0 \to e^+e^-$, PS is the Boltzmann phase space factor, and T is 160 MeV.

Table 3.4: The parameterized electro-magnetic transition form factor Λ of hadrons.

meson	$\Lambda^{-2}(GeV^{-2})$
π^0	1.756 [Nak10]
η	1.756 [Arn09b]
ω	1.756 [Arn09b]
ϕ	3.8 [AB02]
η'	1.84 [Lan85]

The invariant yield of hadrons using in the simulation are shown in the Tab. 3.5 and Tab. 3.6.

Table 3.5: All of the hadron rapidity densities used in di-electron analysis in p+p.

meson	$\frac{dN}{dy}\|_{y=0}$	relative uncertainty.	data used
π^0	1.28 ± 0.18	14%	STAR $(\pi^+ + \pi^-)/2$ [Abe09]
η	0.17 ± 0.039	23%	PHENIX [Adl07b]
ρ	0.22 ± 0.043	15%	STAR [Ada04]
ω	0.133 ± 0.028	21%	PHENIX [Ada11]
ϕ	0.0173 ± 0.0035	20%	STAR [Ada05c]
η'	$(4.07 \pm 1.15) \times 10^{-2}$	29%	PHENIX [Ada11]
J/ψ	$(2.44 \pm 0.38) \times 10^{-5}$	15%	PHENIX [Ada07a]

3.5.2 Heavy flavor contribution

The simulation of heavy flavor contribution is from PYTHIA. There are two measurements to constrain the bottom contribution. One is ratio of B decayed electrons to B+D decayed electrons, measured by electron and hadron correlation [Agg10]. The other one is NPE measurement [Aga11a] in Run 8. We use a power law fit to describe the yields of NPE in the full range of p_T.

In p+p collisions, the B decayed electron was calculated with PYTHIA 6.416 with

Table 3.6: All of the hadron rapidity densities used in di-electron analysis in Au+Au minbias 0-80%.

meson	$\frac{dN}{dy}\|_{y=0}$	relative uncertainty.	data used
π^0	105.4 ± 8.1	8%	STAR $(\pi^+ + \pi^-)/2$ [Abe09]
η	10.77 ± 0.32	30%	PHENIX [Adl07b]
ρ	5.4 ± 0.1	22%	STAR [Ada04]
ω	8.6 ± 2.8	33%	PHENIX [Mil07]
ϕ	2.4 ± 0.11	15%	STAR [Ada05c]
η'	2.05 ± 0.2	100%	PHENIX [Rya09, Nak10]
J/ψ	$(1.79 \pm 0.15) \times 10^{-3}$	15%	PHENIX [Ada07b]
ψ'	$(2.6 \pm 0.7) \times 10^{-4}$	27%	PHENIX [Gav95, Sil09]

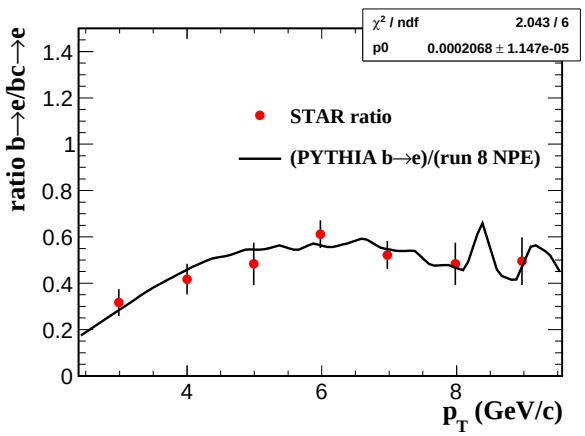

Figure 3.28: Fit the simulated $b \to e/NPE_{run8}$ to the ratio of $b \to e$ to $b \to e{+}c \to e$ in p+p at 200 GeV.

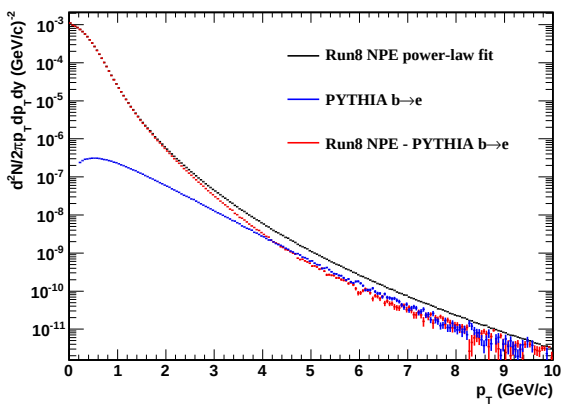

Figure 3.29: The fixed $b \to e$ and $c \to e$ from PYTHIA simulation.

CTEQ5L parton distribution function [Lai00]. The yields of $b\bar{b}$ can be obtained by fitting the ratio of B decayed electrons to NPE measurement to the published ratio. The fit is shown in Fig. 3.28. The bottom cross section from fit is $6.2 \pm 0.34\mu b$. PHENIX measurement value is $\sigma_{b\bar{b}} = 3.2^{+1.2}_{-1.1}(stat.)^{+1.4}_{-1.3}(syst.)\mu b$ [Ada09]. The difference will be taken as uncertainty of bottom cross section. The simulated $b \rightarrow e$ and $c \rightarrow e$ are shown in the Fig. 3.29.

The charmed hadron decayed electron was calculated with two sets of PYTHIA parameters marked as Set I and II. Set I is default PYTHIA 6.416 with CTEQ5L setting named. Set II has some tuned parameters compare with Set I. The different parameters are:

- PARP(91)=1 (k_T factor)
- PARP(67)=1 (parton shower level).

The two sets of parameters were using MSEL=1. There is a difference between MSEL=1 and MSEL=4. The MSEL=4 set doesn't include the process that outgoing charm current combined with a energetic parton to create a string and did not fragment into charmed hadron. To check the results from PYTHIA, the D spectra [Ada05b] and the previous $c \rightarrow e$ spectra are used for comparing. The comparisons are shown in Fig. 3.30. Set II shows good agreement between the data and simulation. The difference between Set I and II will be taken as systematic uncertainty of charm component. The $c\bar{c} \rightarrow ee$ is also reconstructed from the events generated by Set II. The charm cross section is using $0.956 \pm 0.10mb$. This number is from minimum χ^2 calculation between data and simulation. The data include D^0 spectra [Ada05b], two NPE measurements [Ada05b, Aga11a] and di-electron measurement. The detail will be discussed in Chapter. 4. The charm cross section from STAR earlier publication in p+p 200 GeV is $1.4 \pm 0.2(stat.) \pm 0.4(syst.)\ mb$ [Ada05b], while from PHENIX is $567 \pm 57 \pm 193\ \mu b$ [Ada06]. These two numbers are also scaled to indicate the uncertainty of charm contribution to di-electron continuum, shown in the Chapter. 4.

In Au+Au collisions, because the charm cross section follow the number of binary (N_{bin}) scaling, the charm cross section from p+p is scaled by the number of binary collisions to match with data. Here $N_{bin} = 302.6$ in Au+Au minbias 0-80%.

The cocktail within STAR acceptance in p+p and Au+Au collisions are shown in the Fig. 3.31 and Fig. 3.32, respectively.

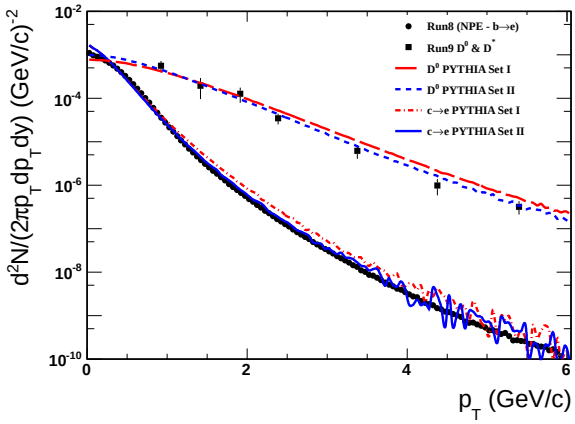

Figure 3.30: Comparisons of $c \to e$ and D^0 yields data and PYTHIA simulation in p+p at 200 GeV.

3.6 Systematic uncertainties

In p+p collisions, the systematic uncertainties of data mainly come from:

- Background subtraction.
- Fast hadron contamination.
- Efficiency calculation.
- Like-sign and mixed-event difference at $M_{ee} > 0.7$ GeV/c^2.
- Normalization.

The background subtraction uncertainties include the normalization factor uncertainty and the acceptance correction uncertainty. The normalization uncertainties is calculated

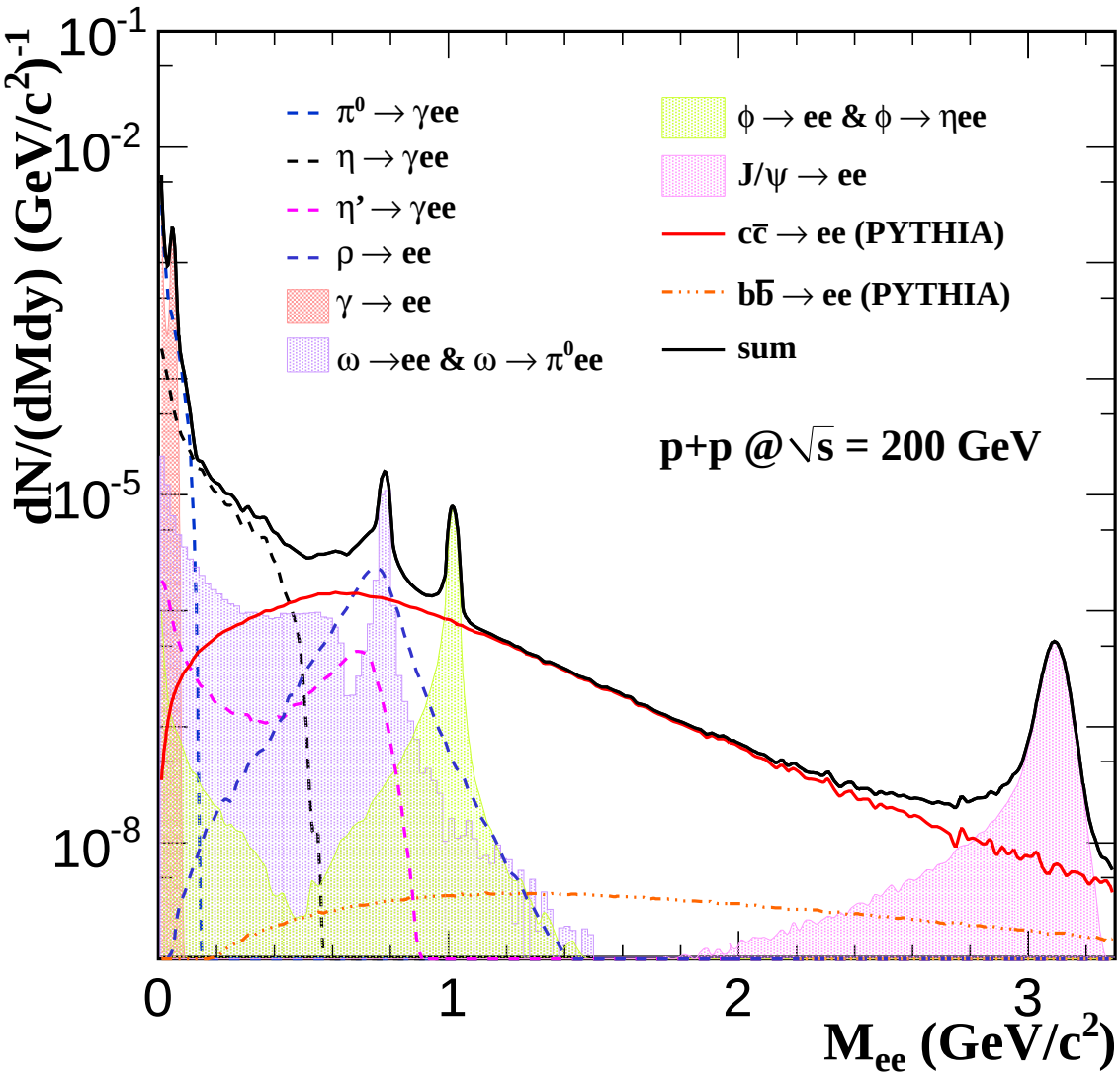

Figure 3.31: The cocktail within STAR acceptance in p+p at 200 GeV.

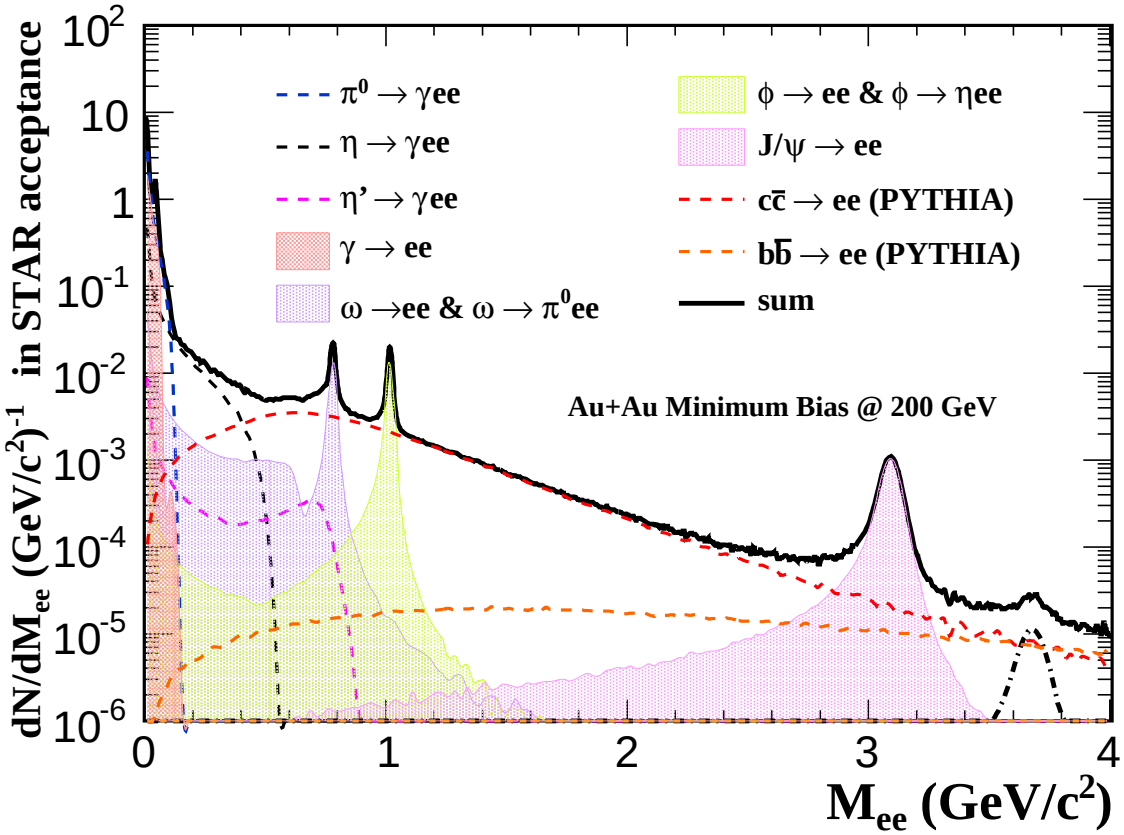

Figure 3.32: The cocktail within STAR acceptance in Au+Au at 200 GeV.

by changing the normalization range from (0.4,1.5) to (0.4,1.) GeV/c^2. The signal after background subtraction with and without f_{acpt} will give the acceptance correction uncertainty. The background subtraction is a small effect ($< 10\%$) in p+p collisions. The fast hadron contamination is studied by selecting the pure pion as same amount of the contaminated pion to make pion pairs but using the electron mass instead of pion mass, to see the effect of the misidentified pairs. The contaminated pion is estimated by the exp+gaus fit as described in Sec. 3.2. The contamination is also a small effect, and in the low S/B ratio mass range. The embedding efficiency has a 5% uncertainties for each track. It was propagated to electron pairs with 10% uncertainties. The last uncertainties is the difference between like sign and mixed event at $M_{ee} > 0.7$ GeV/c^2. Over 0.7 GeV/c^2, we only subtracted mix event background, but there is still some difference between like sign and mixed event. To be conservatively estimated, the difference was also taken into systematic uncertainties. The normalization uncertainty is the uncertainty of non-singly-diffractive cross section measurement in p+p.

The cocktail simulation uncertainties include yield uncertainties of mesons and the cross section uncertainties of charm and bottom.

All of the uncertainties in p+p are shown in the Fig. 3.33.

In Au+Au collisions, the systematic uncertainties of electron pair signal are listed at below:

- Background subtraction.
- Acceptance correction.
- Fast hadron contamination.
- Like-sign and mixed-event difference at $M_{ee} > 0.7$ GeV/c^2.

The background subtraction uncertainty calculation is same as that in p+p. The acceptance uncertainty has been studied by different correction methods, one is to scale the integrated f_{acpt} of whole p_T range for each mass bin, the other one is to scale the f_{acpt}

bin by bin as described in Eq. 3.4. This difference in the final yields is less than 5%. The hadron contamination in Au+Au is larger than that in p+p. The hadron mass can be calculated via time-of-flight as

$$m = \sqrt{p^2(1/\beta^2 - 1)}. \tag{3.15}$$

β is measured by TOF+TPC. We selected a pure hadron sample (π, K, p) by cutting on a narrow mass range around the hadron mass to make the contaminated pairs but with electron mass, then scaled the number of tracks to the same amounts of the contaminated hadrons. This is similar to the p+p case, but the contaminated hadrons include π, K, p and merged π, while p+p case only has π. The last uncertainty from data, the difference between like sign and mixed event is studied same way as that in p+p.

We scaled the yields of mesons and the cross section uncertainties of charm and bottom (by N_{bin} scaling) for cocktail simulation, the yields uncertainties are propagated to the cocktail uncertainties. All of the uncertainties in p+p and Au+Au are shown in the Fig. 3.33 and Fig. 3.34, respectively.

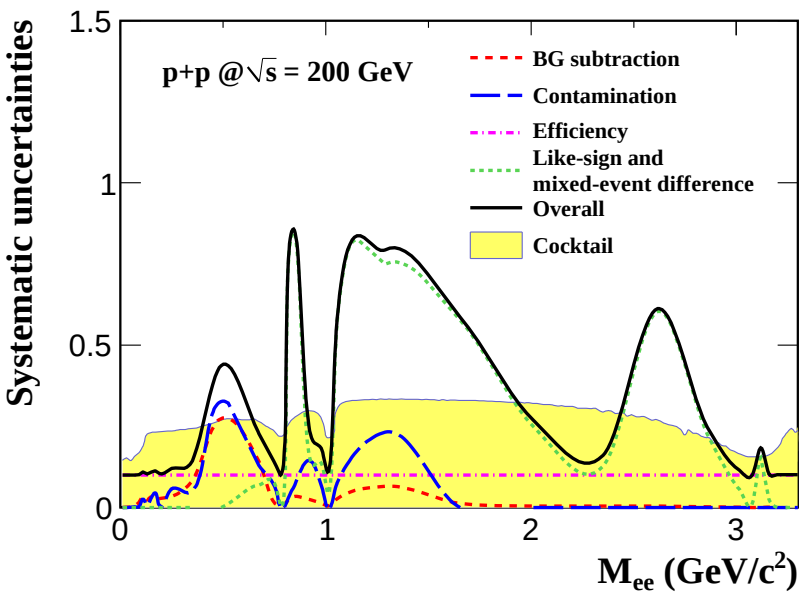

Figure 3.33: Systematic uncertainties as a function of mass from different source contributions in p+p at 200 GeV. Also shown are the systematic uncertainties for the cocktail simulation.

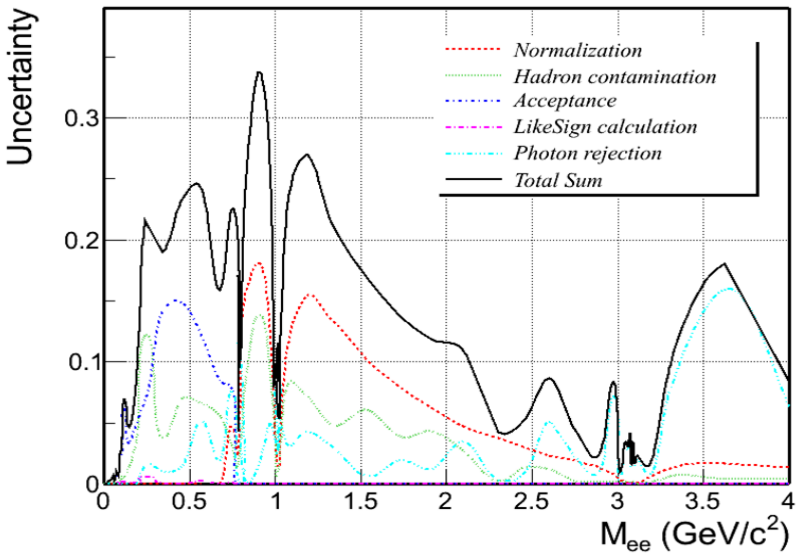

Figure 3.34: Systematic uncertainties from different sources in Au+Au at 200 GeV.

Table 3.7: Systematic uncertainties from different sources for di-electron continuum.

source	p+p	Au+Au
background subtraction	0-27%	0-18%
contamination	0-32%	0-14%
likesign and mixed-event difference	1-84%	0-15%
efficiency	10%	10%
normalization	14%	-
cocktail simulation	14-33%	10-33%

Tab. 3.7 shows systematic uncertainties of all the sources.

CHAPTER 4

Results and Discussion

The background rejection and subtraction was applied to the di-electrons foreground. The e^+e^- signals were obtained as described in Sec. 3.3.1. In this chapter, the various results of this analysis are introduced. Comparison of di-electron expected production to data in p+p will be discussed in Sec. 4.1. The simulation of expected production is called cocktail simulation. The charm cross section and yields of ϕ and J/ψ are presented in Sec. 4.1. The branching ratio limit of rare decay $\eta \rightarrow ee$ extracted from di-electrons is presented in same section. The ω resonance p_T spectra in p+p and Au+Au collisions are concluded in Sec. 4.2. The preliminary results of the analysis of Au+Au minimum bias event are presented in Sec. 4.3.

4.1 Di-electron production in p+p Collisions at 200 GeV at STAR

After efficiency correction, the invariant mass spectrum of di-electron within STAR acceptance compared to the expectation contributions in p+p collisions at 200 GeV is shown in Fig. 4.1. The expectation contributions have been sampled the momentum resolution and radiation energy loss effect. The ratio of data to cocktail simulation is shown in lower panel. Within the uncertainties, the cocktail simulation is consistent with the measured di-electron continuum. The precision of the data leaves little room for studying the virtual photons in p+p collisions at $\sqrt{s} = 200$ GeV.

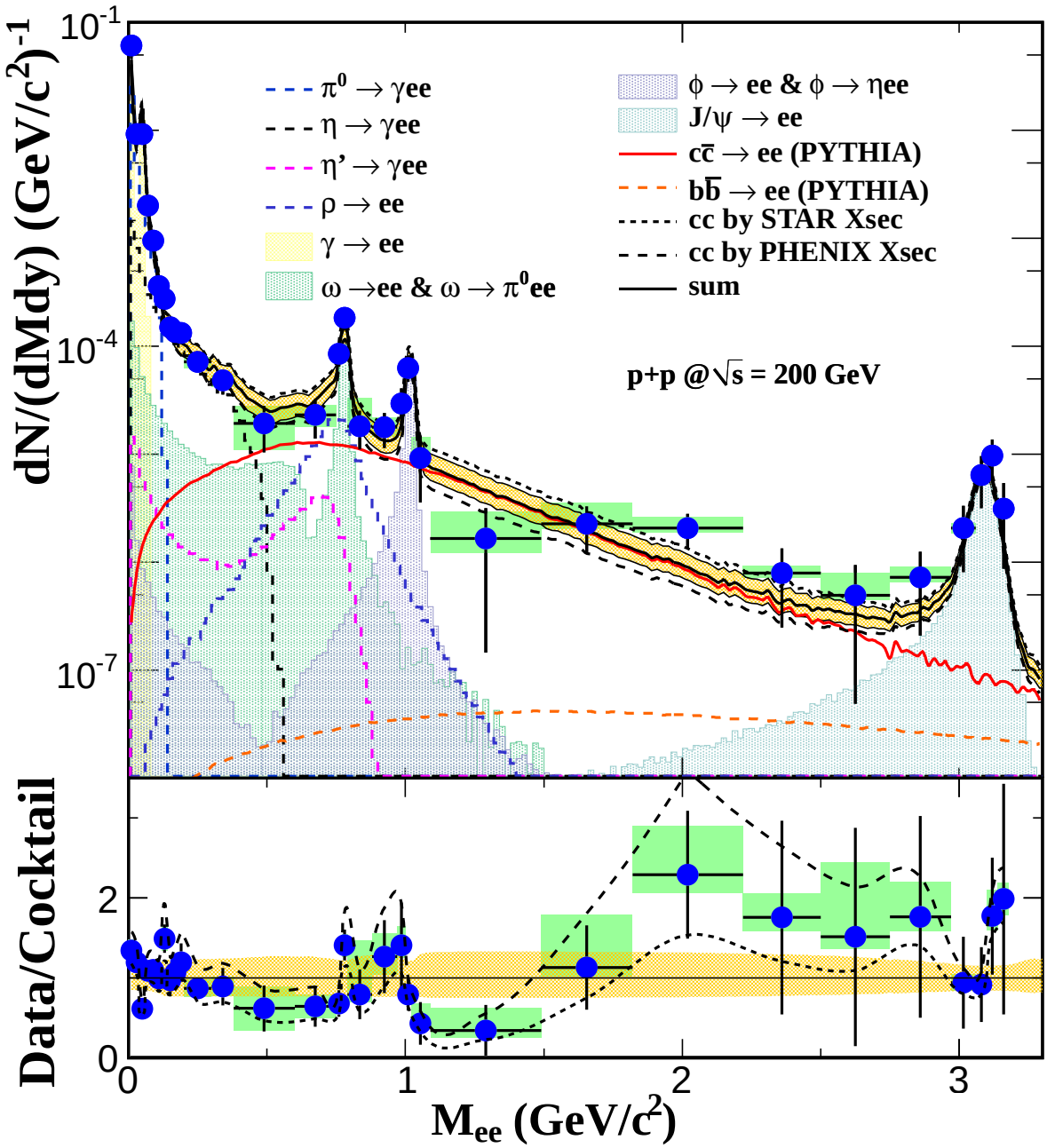

Figure 4.1: The comparison for di-electron continuum between data and simulation after efficiency correction within the STAR acceptance in 200 GeV minimum-bias p+p collisions. The di-electron continuum from simulations with different source contributions are also shown. The statistical errors are shown as bars. The systematic uncertainties are shown as boxes. The 14% normalization uncertainty on data is not shown. The band on top of the curve illustrates the systematic uncertainties on cocktail.

4.1.1 Charm cross section in p+p at 200 GeV

The e^+e^- invariant mass spectra from open heavy-flavor pair were obtained by using PYTHIA. The PYTHIA setting is discussed in Sec. 3.5.

The di-electron data was fitted by the charm decayed $e^+e^-$from PYTHIA alone, as shown in the Fig. 4.2. Red triangles show the charm dominant range. The random charm to e^+e^-contribution was reproduced by the two daughter electrons from charmed hadron decays, in which the correlation of e^+e^- were artificially broken. The difference of two fits are considered as systematic uncertainty. The fit to di-electron alone gives a charm cross section of $0.83 \pm 0.23(stat.) \pm 0.26(syst.)\ mb$.

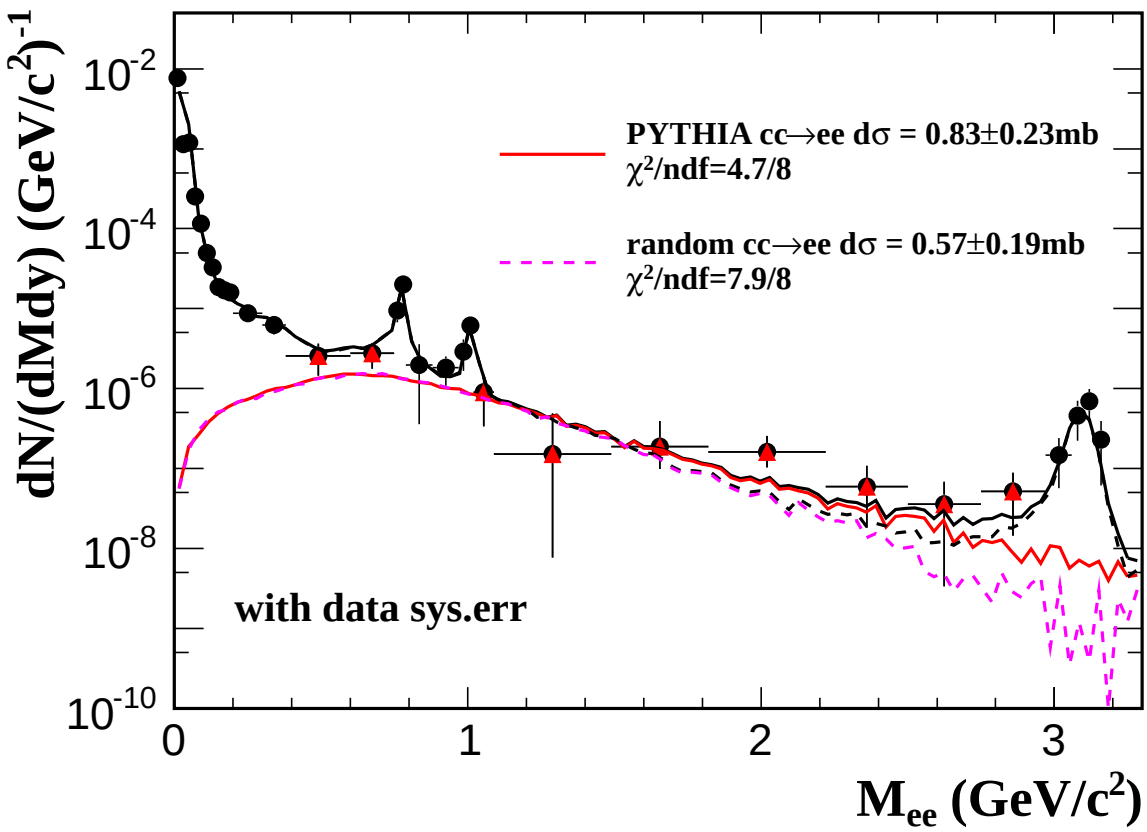

Figure 4.2: $e^+e^-$of charm components from PYTHIA simulation fit to the data shown as red line. Red triangles show the fit data points which are dominant by charm contributions. The fit of random e^+e^-pair is estimated to be the systematic uncertainty.

The simultaneous fit to the di-electron continuum, open charm [Ada05b], and non-photonic electron [Aga11a] spectra can yield a charm cross section. Scaling the same

charm cross section, the simulated production of di-electron, charmed hadron and non-photonic electron from PYTHIA can be compared to the data. The χ^2 between them quantifies the best common scaling factor, the charm cross section. Fig. 4.3 left panel shows the expected simulation spectra scaled by a certain charm cross section compared to the measurements, right panel shows the overall χ^2 as a function of the charm cross section. The minimum χ^2 is located at a charm cross section of 0.96 mb. Using the default PYTHIA setting (Set I in Sec. 3.5.2), the minimum χ^2 will give a number of 0.69 mb. The difference is considered as the systematic uncertainty. The simultaneous fit thus yields a charm cross section of $0.96 \pm 0.10(stat.) \pm 0.27(syst.)\ mb$, which is used to scale the charm contribution in Fig. 4.1.

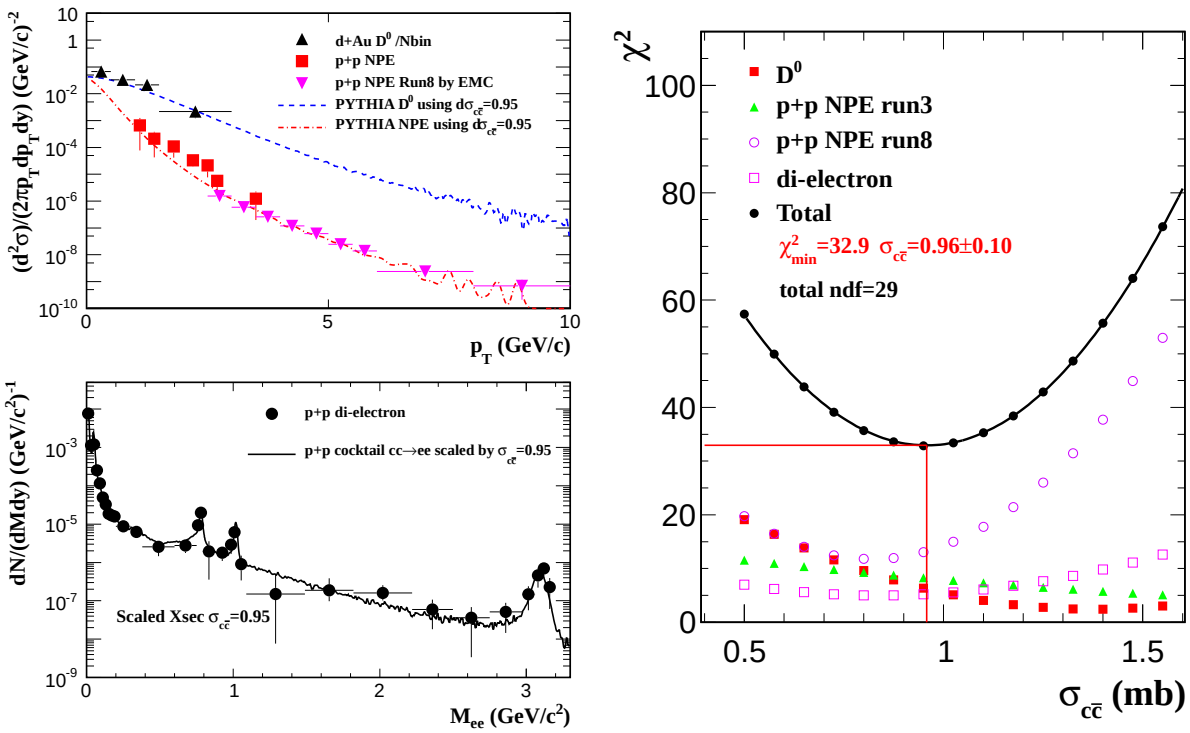

Figure 4.3: Left: The simulations scaled with a charm cross section number compared to the corresponding measurements in p+p collisions. Right: χ^2 between simulation and measurement as a function of input charm cross section.

4.1.2 Yields of ϕ and J/ψ in p+p at 200 GeV

Yields of the long-lived vector mesons with narrow peak of di-electron invariant mass, such as $\omega, \phi, and\ J/\psi$, can be extracted from this analysis. The ω will be discussed in the Sec. 4.2. Here we use the mixed-event technique to reconstruct the background, and the cocktail without the vector meson which we want to measure can describe residual background from other sources. Such as for ϕ, two components, ϕ meson mass distribution and the cocktail excluding ϕ were used to fit the data. Then the yields can be extracted from fit.

We use two components to fit the distribution of M_{ee} at $0.98 < M_{ee} < 1.04$ GeV/c^2 for ϕ and at $3 < M_{ee} < 3.16$ GeV/c^2 for J/ψ: one for the $\phi \rightarrow e^+e^-$ or $J/\psi \rightarrow e^+e^-$ signal and one for the residual background. The line shapes of $\phi \rightarrow e^+e^-$ and $J/\psi \rightarrow e^+e^-$ are from simulations as discussed in Sec. 3.5. The residual background shape and magnitude are obtained from the cocktail simulation. The systematic uncertainties of the ϕ and J/ψ dN/dy due to the residual background are negligible. This is evaluated by changing the magnitude of the background allowed by the uncertainties of the cocktail simulation. The systematic uncertainties on the efficiency correction factors are about 10%. The normalization uncertainty is 14% in p+p collisions.

Fig. 4.4 shows the fits to the M_{ee} distributions to obtain the total yields dN/dy for ϕ and J/ψ at mid-rapidity in non-singly diffractive p+p collisions at $\sqrt{s} = 200$ GeV. The dN/dy for ϕ is 0.012±0.003(stat.)±0.002(syst.), consistent with the measurements from $\phi \rightarrow K^+K^-$ from STAR [Ada05c]. The dN/dy for J/ψ is (2.6±0.8 (stat.)±0.5(syst.))$\times 10^{-5}$, consistent with the measurements from PHENIX [Ada07a].

4.1.3 Rare decay

Rare processes like leptonic decays of hadrons provide possible observables in searching for traces of new physics beyond the Standard Model (BSM) [Dor10, BES09, SLW92, BSS88]. The branching ratio (B.R.) of $\eta \rightarrow e^+e^-$ can be predicted in SM with good precision, which is 2.3×10^{-9}. Couplings from BSM physics can increase this B.R. signif-

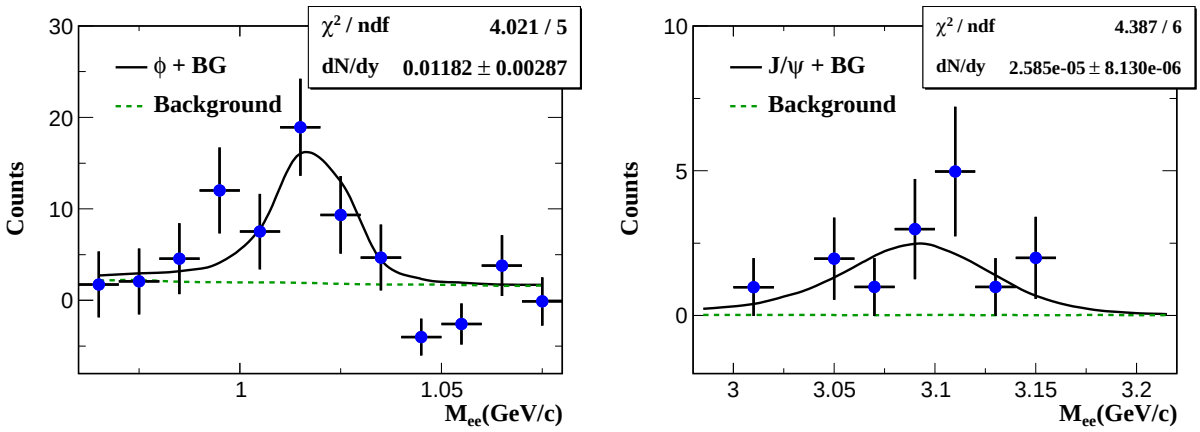

Figure 4.4: Left: The M_{ee} distribution after the mixed-event background subtraction at $0.95 < M_{ee} < 1.08$ GeV/c^2 in p+p collisions at $\sqrt{s} = 200$ GeV. The curve represents the fit in the range of $0.98 < M_{ee} < 1.04$ GeV/c^2. Errors on data points are statistical. Right: The M_{ee} distribution after the mixed-event background subtraction at $2.85 < M_{ee} < 3.30$ GeV/c^2 in p+p collisions at $\sqrt{s} = 200$ GeV. The curve represents the fit in the range of $3 < M_{ee} < 3.16$ GeV/c^2. Errors on data points are statistical.

icantly [Dor10]. The B.R. measurement is an important observation to test the BSM.

The cocktail can describe the data reasonably well around the η mass without the $\eta \rightarrow e^+e^-$ decay channel. We zoom into the low mass range and show the data and cocktail comparison in Fig. 4.5. The dashed curve is the cocktail with the $\eta \rightarrow e^+e^-$ decay channel included in the fit. The dot-dashed peak is the $\eta \rightarrow e^+e^-$ contribution with the upper limit of its B.R. from the PDG [Nak10], which is 2.7×10^{-5} [BB08]. The best fit is shown as the solid curve. In our measurements, at a 90% confidence level, the upper limit for $\eta \rightarrow e^+e^-$ is found to be 4.3×10^{-6}.

4.2 ω meson yields in p+p and Au+Au Collisions at 200 GeV at STAR

As mentioned in Sec. 4.1.2, two components fit is used to extract the yields of long-lived vector mesons. For ω, it is used to extract the $\omega \rightarrow e^+e^-$ signal in the invariant mass range of $0.7 < M_{ee} < 0.85$ GeV/c^2: one of the components is the $\omega \rightarrow e^+e^-$ line shape and the other one is the residual background. The line shape of $\omega \rightarrow e^+e^-$ and the shape and

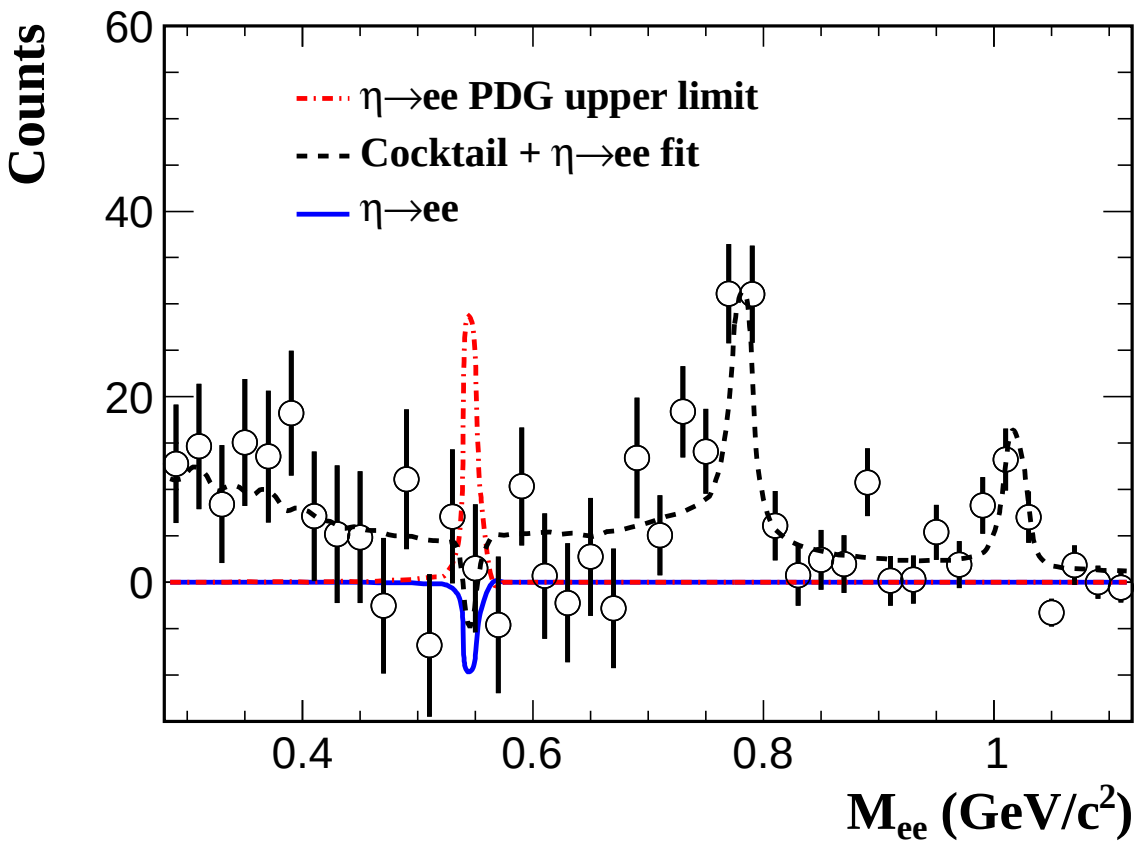

Figure 4.5: m_{ee} distribution for di-electron production in p+p collisions at $\sqrt{s} = 200$ GeV. The dashed curve is the cocktail with the $\eta \to e^+e^-$ decay channel included in the fit. The dot-dashed peak is the $\eta \to e^+e^-$ contribution with the upper limit of its branching ratio from the PDG [BB08], which is 2.7×10^{-5}. The best fit is shown as the solid curve.

magnitude of the background are from the simulations, as discussed in detail in Sec.3.5. The systematic uncertainties of the $\omega \rightarrow e^+e^-$ raw yields are derived by changing the magnitude of the background and the analysis cuts. The total contribution is about 20%. Fig. 4.6 shows the fit to the M_{ee} distribution at $0.7 < M_{ee} < 0.85$ GeV/c^2 in three different p_T bins in p+p collisions at $\sqrt{s} = 200$ GeV.

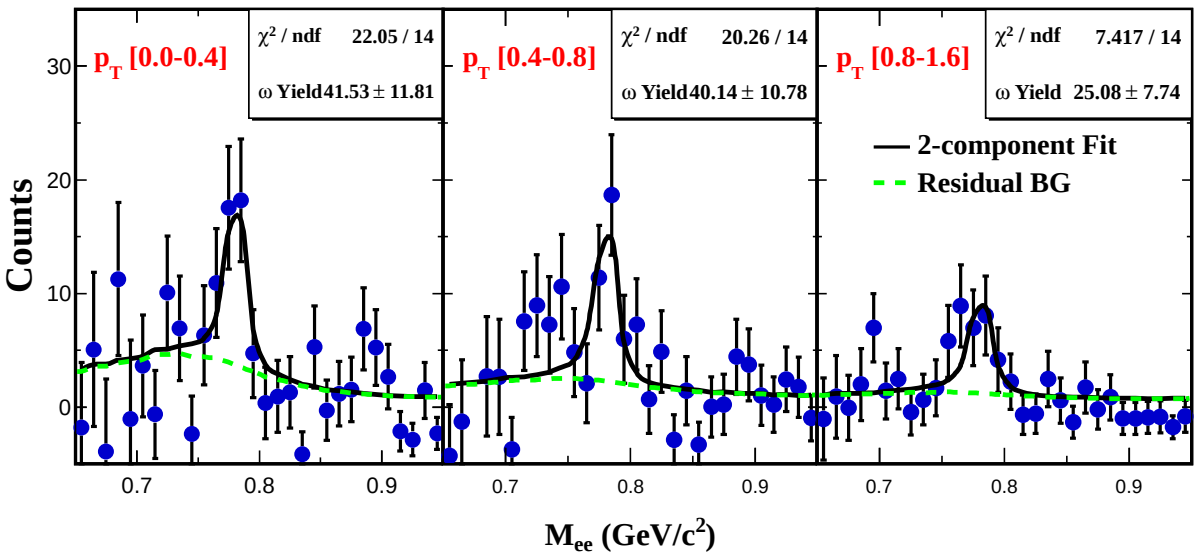

Figure 4.6: The M_{ee} distribution for three different p_T bins after the mixed-event background subtraction at $0.65 < M_{ee} < 0.95$ GeV/c^2 in p+p collisions at $\sqrt{s} = 200$ GeV. The curves represent fits in the range of $0.7 < M_{ee} < 0.85$ GeV/c^2. Errors on data points are statistical.

Fig. 4.7 shows the fit results in Au+Au collisions.

While the di-electron continuum has only been corrected for efficiency within the STAR acceptance, the vector meson spectra ($\omega \rightarrow e^+e^-$) are corrected for all detector effects and acceptance and are presented as final differential invariant yields as a function of p_T, detailed in Sec.3.4. Combining the TPC tracking, TOF acceptance and response, and the dE/dx cut efficiency, the total efficiencies for $\omega \rightarrow e^+e^-$ at $|y| < 1$ in p+p and Au+Au is shown in Fig. 4.8.

The efficiency and acceptance corrected ω invariant yields $d^2N/(2\pi p_T dp_T dy)$, after correction for $\omega \rightarrow e^+e^-$ B.R. are presented in Fig. 4.9. Star symbols are the yields in non-singly diffractive p+p collisions at $\sqrt{s} = 200$ GeV. The circled symbols represent

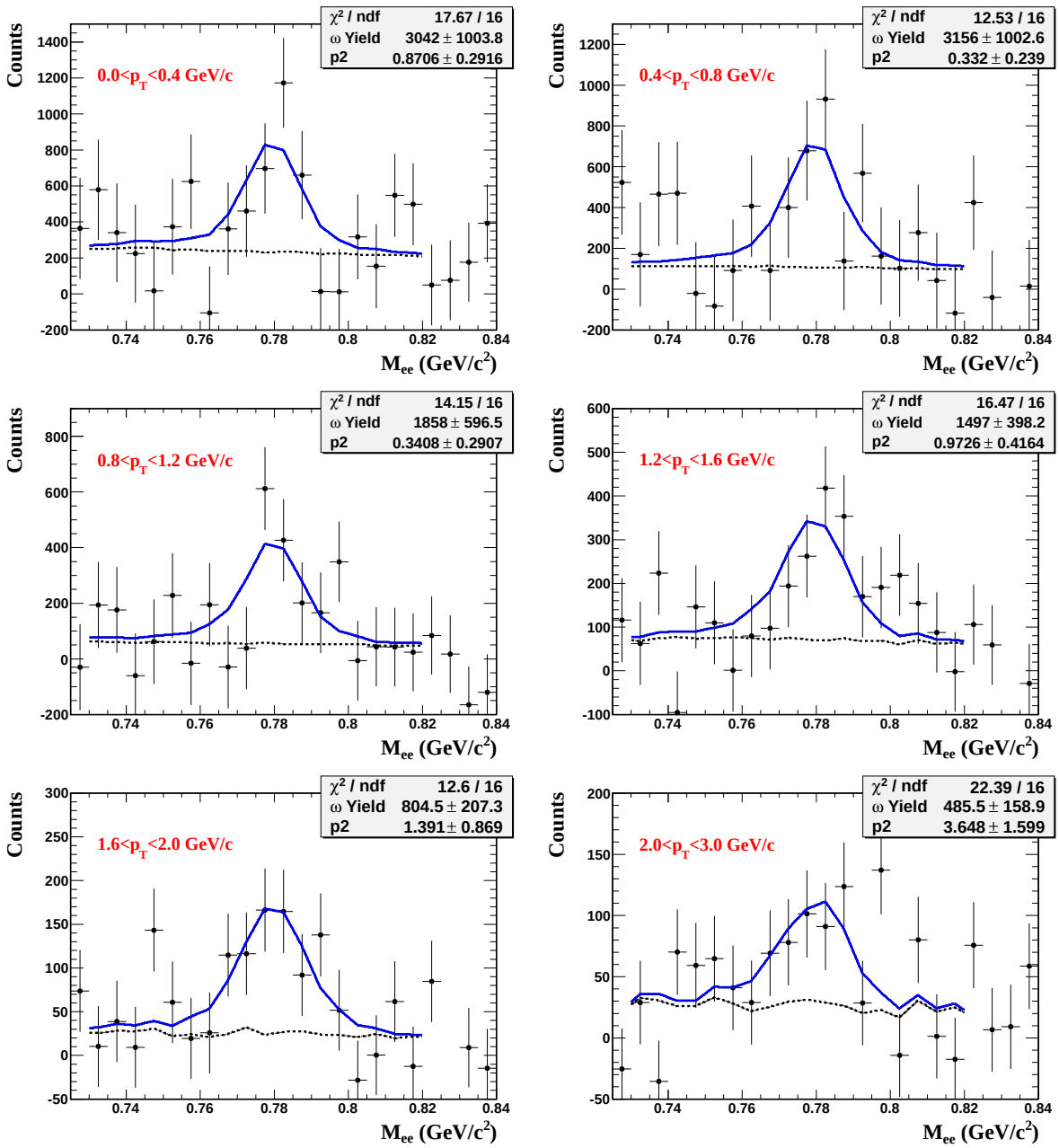

Figure 4.7: The M_{ee} distribution for six p_T bins from 0-3 GeV/c after the mixed-event background subtraction at $0.65 < M_{ee} < 0.95$ GeV/c^2 in Au+Au collisions at $\sqrt{s} = 200$ GeV. The curves represent fits in the range of $0.73 < M_{ee} < 0.82$ GeV/c^2. Errors on data points are statistical.

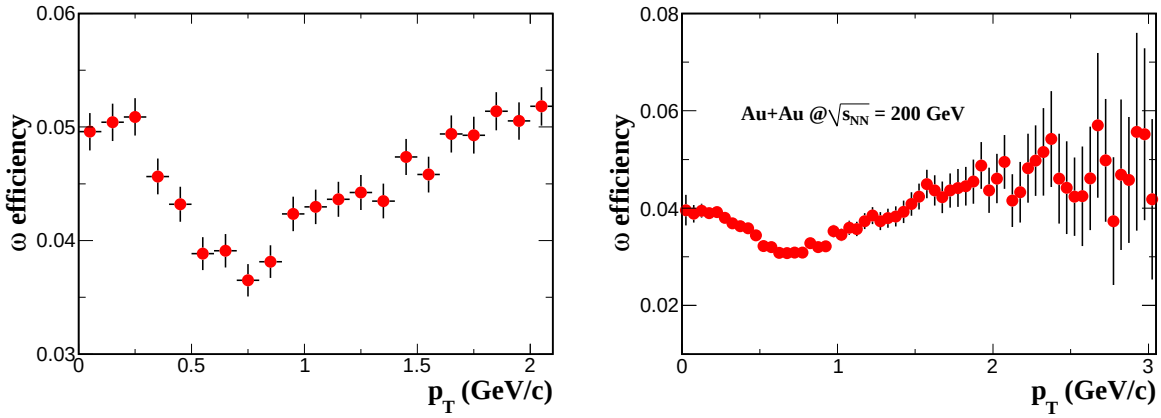

Figure 4.8: The efficiency including STAR acceptance for $\omega \rightarrow e^+e^-$ at $|y|<1$. Left is for p+p collisions, right is for Au+Au collisions.

PHENIX published results [Ada11]. The bars are statistical errors. Red squares are the yields in Au+Au minimum bias collisions. The boxes are systematic uncertainties, which are dominated by the fit and efficiency correction factors. The present ω yields from di-leptonic decays in p+p are consistent with the previous results [Ada11] and the extrapolation from the Tsallis fit to the high p_T ω yields [Tan09, Adl07a]. The broken dashed blue line is the ω line shape predicted by TBW fit to other light hadrons in Au+Au MB collisions. The expected ω line shape is scaled by a yields of 8.6±2.8 [Mil07]. The prediction and data are matched each other well, it indicates that the ω meson has same flow velocity as other light hadrons in Au+Au MB events. A normalization uncertainty of 14% is not shown for p+p collisions.

4.3 Di-electron production in Au+Au Collisions at 200 GeV at STAR

Fig. 4.10 compares the di-electron mass spectrum within STAR acceptance in Au+Au minimum bias events to the expected yield from the cocktail simulation. The cocktail simulation is described in Sec. 3.5. The charm contribution is generated from PYTHIA, and scaled by the charm cross section in p+p $(0.96 \pm 0.10(stat.) \pm 0.27(syst.)mb)$ and the number of binary collisions (N_{coll}), which is 302 for Au+Au minimum bias events.

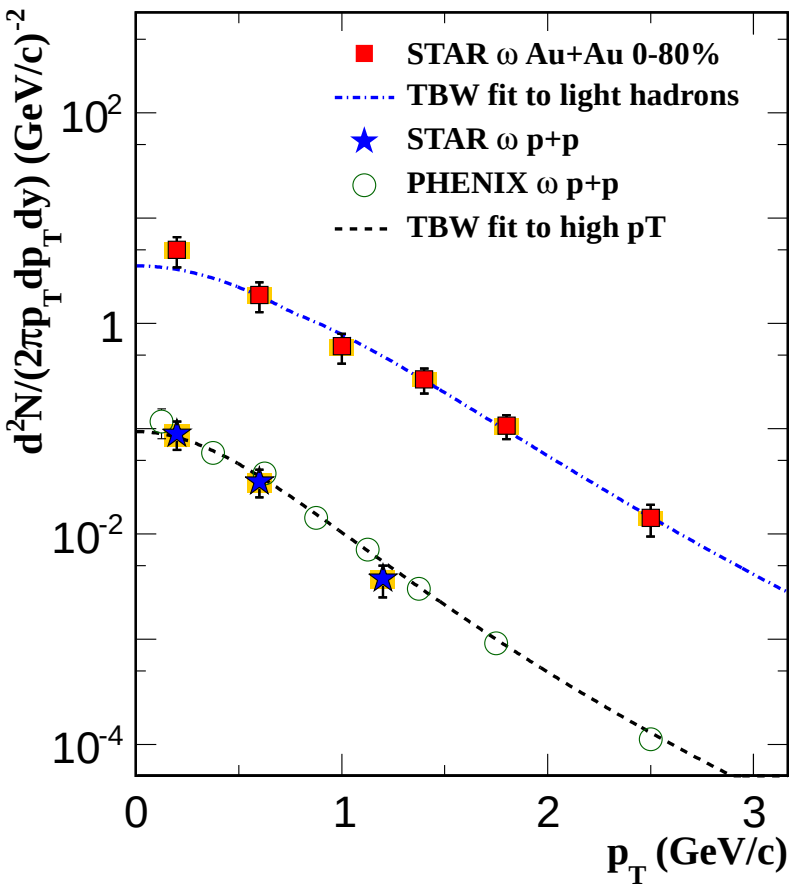

Figure 4.9: The $\omega \to e^+e^-$ invariant yield, divided by its B.R.. Star symbols are the yields in non-singly diffractive p+p collisions at $\sqrt{s} = 200$ GeV. Red squares are the yields in Au+Au minimum bias collisions. The circles represent PHENIX published results [Ada11]. The bars are statistical errors and boxes are systematic uncertainties. The lines represent predictions of Tsallis blast-wave function by fitting other measurements in p+p and Au+Au.

For hadron sources, the scale factor of meson yields are based on the yields presented in Tab. 3.6. The cocktail does not include the ρ meson contribution, because ρ can be modified in medium due to the short life time and strong coupling to $\pi\pi$ channel. The green box shows the systematic uncertainties mentioned in Sec. 3.6. The yellow band shows systematic uncertainty of cocktail simulation. Fig. 4.10 lower panel shows the ratio between data and simulation. The Au+Au mass spectra show a little excess above the cocktail, in particular for the mass range 0.15-0.75 GeV/c^2. The ratio of integral yields to the cocktail at this mass range is $1.53 \pm 0.07(stat.) \pm 0.41(syst.)$.

As we mentioned in the Sec. 1.4.2, the di-electron continuum can be directly compared to theoretical calculation. Through the comparison between data and model calculation, the properties of the medium, such as temperature, might be derived.

4.3.1 Comparison of STAR and PHENIX di-electron continuum

The excess in the LMR region is not as large as the PHENIX measurement shown in Fig. 1.10. The ratio of integrated yields to cocktail is $4.7 \pm 0.4(stat.) \pm 1.5(syst.)$ [Ada10] in the mass 0.15-0.75 GeV/c^2 from PHENIX measurements. The difference between two measurements is at 2σ level. To address the difference where come from, we repeated the cocktail simulation and applied the PHENIX acceptance in the simulation. The simulation procedures of PHENIX di-electron measurement are described in [Ada10].

Fig. 4.11 shows the reproduced cocktail within PHENIX acceptance compared to the cocktail presented by PHENIX. The green dotted dash line shows the PHENIX cocktail. The blue solid line is the cocktail reproduced by our method. The reproduced cocktail is consistent with the PHENIX cocktail simulation. The charm contribution $c\bar{c} \rightarrow ee$ is scaled by same charm cross section ($567 \pm 57(stat.) \pm 224(syst.)\mu b$ [Ada06]) which PHENIX used [Ada10]. Our cocktail simulation within PHENIX acceptance are consistent with the PHENIX cocktail simulation.

We also generate a cocktail within STAR acceptance by same procedures. The difference between the two cocktail is only the acceptance. The STAR di-electron continuum

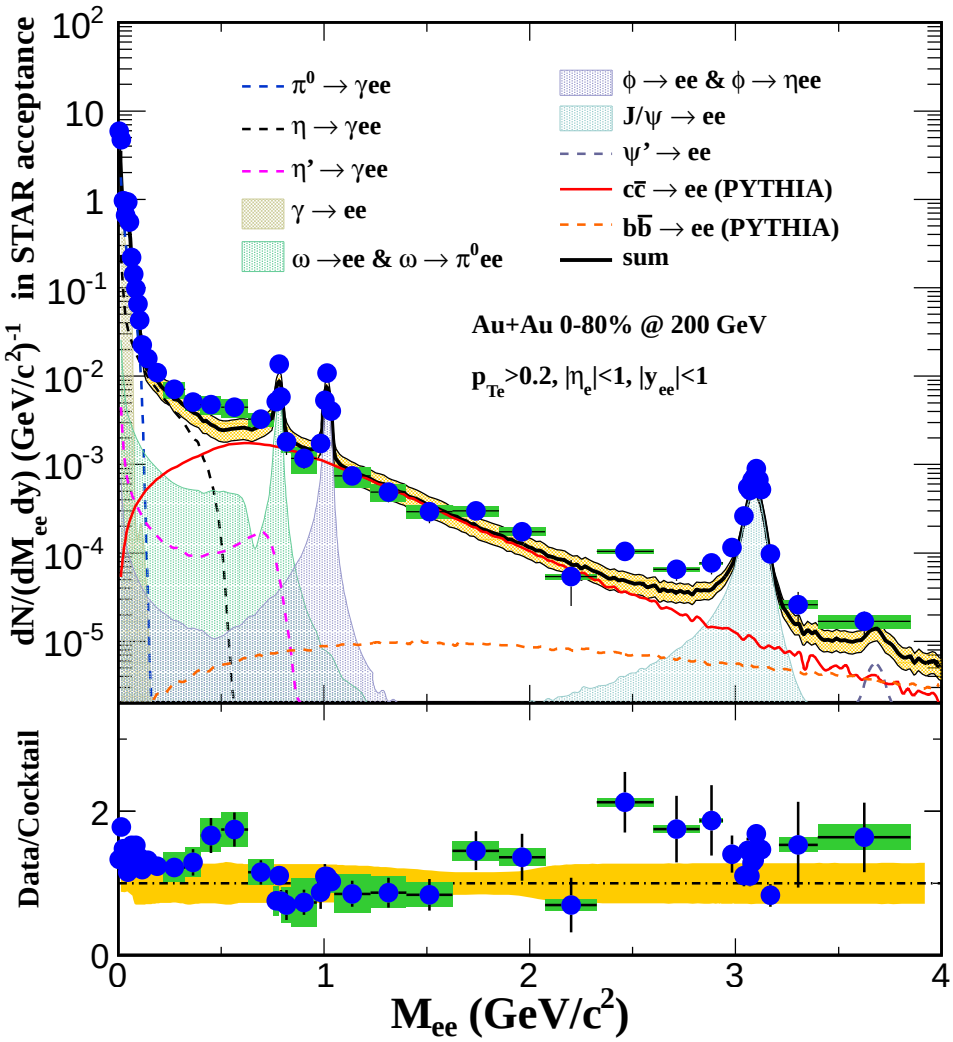

Figure 4.10: Comparison for di-electron continuum between data and simulation after efficiency correction within STAR acceptance in minimum bias Au+Au collisions at $\sqrt{s_{\rm NN}}$=200 GeV. The di-electron continuum from simulation includes light hadron and correlated decays of charm, bottom and Drell-Yan. The charm contribution is generated from PYTHIA and scaled by the number of binary collisions. Statistical errors are shown as bars. The systematic uncertainties are shown as boxes. The bottom panel shows the ratio of data to cocktail.

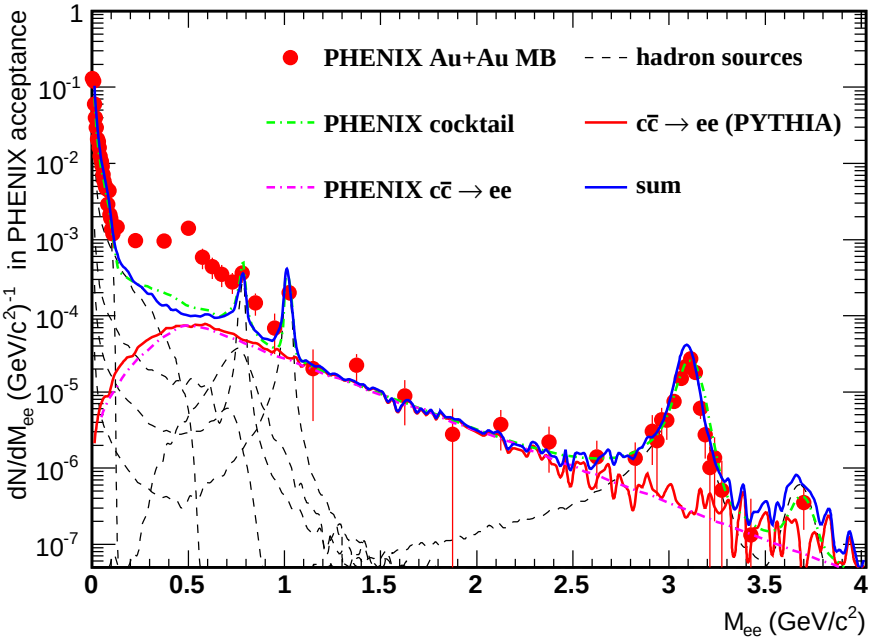

Figure 4.11: The di-electron cocktail within PHENIX acceptance compared to PHENIX cocktail in minimum bias Au+Au collisions at $\sqrt{s_{\rm NN}}$=200 GeV. Blue solid line is the reproduced cocktail within PHENIX acceptance. Green dotted dashed line is PHENIX cocktail in the [Ada10]. Statistical errors are shown as bars. Red solid line is charm contribution scaled by PHENIX charm cross section. Magenta dotted dashed line is the charm contribution by PHENIX PYTHIA simulation in the [Ada10].

is scaled by the acceptance difference, then compared to the PHENIX di-electron continuum. Fig. 4.12 shows the comparison of PHENIX and STAR di-electron continuum, STAR di-electron continuum is scaled by the acceptance difference between PHENIX and STAR. The cocktails are similar, but the data can not match with each other. The comparison shows that the difference of excess in LMR come from measurements. The different acceptance between the STAR and PHENIX might introduce some effect.

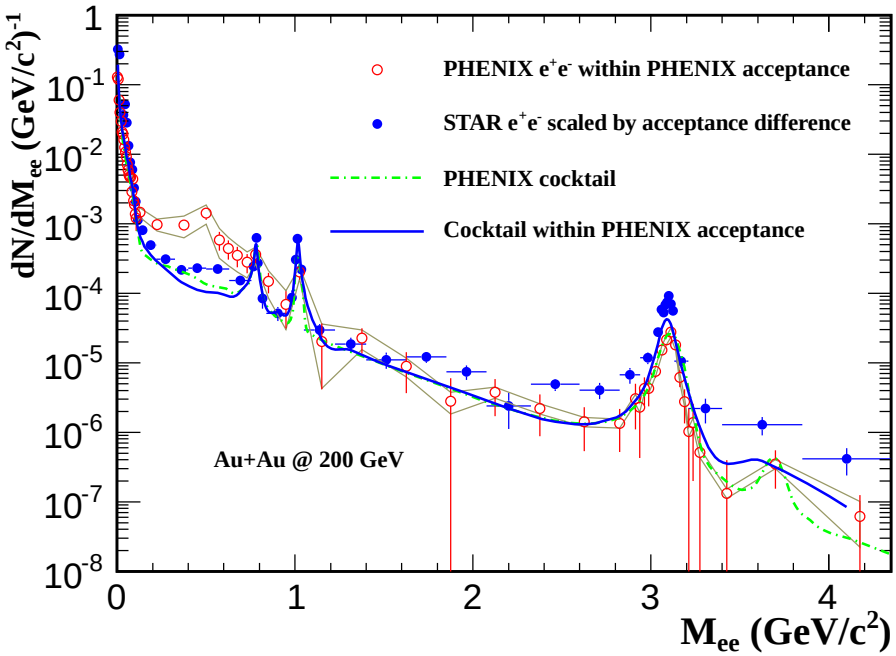

Figure 4.12: Comparison for di-electron continuum between STAR and PHENIX in minimum bias Au+Au collisions at $\sqrt{s_{\rm NN}}$=200 GeV. Blue dots represent the STAR di-electron continuum scaled by the acceptance difference between STAR and PHENIX. Open circles show the PHENIX data. Statistical errors are shown as bars. Band is the PHENIX data systematic uncertainties.

CHAPTER 5

Summary and Outlook

5.1 Summary

In summary, we measured the di-electron continuum in p+p and Au+Au collisions at $\sqrt{s} = 200$ GeV within STAR acceptance at RHIC. These measurements were enabled by the Time-Of-Flight detector upgrade. The measurement in p+p collisions allowed us to extract the charm cross section in the intermediate mass region ($0.96 \pm 0.10(stat.) \pm 0.27(syst.)mb$) and the rapidity density (dN/dy) of ϕ ($0.12 \pm 0.003(stat.) \pm 0.002(syst.)$) and J/ψ ($2.6 \pm 0.8(stat.) \pm 0.5(syst.) \times 10^5$) meson. The new upper limit of the branching ratio for $\eta \rightarrow e^+e^-$ is set to be 4.3×10^{-6}. The differential invariant yields of ω meson are measured in p+p and Au+Au collisions. A study of the ω spectra shows the ω follows the light hadron flow behavior in minimum bias Au+Au collisions.

The results in p+p provide a reference for the di-electron continuum measurement in heavy ion collisions. The ratio of di-electron continuum in minimum-bias Au+Au collisions to the expectation is measured to be $1.53 \pm 0.07(stat.) \pm 0.41(syst.)$ in the mass range 0.15-0.75 GeV/c^2.

5.2 Outlook

The di-electron analysis in central Au+Au collision is still ongoing. There are 250 M central data which allow to extract the enhancement in LMR in Au+Au most central collisions. The di-electron in intermediate mass region can be used to study the charm modification and/or QGP thermal radiation in central collisions. Another physics topic,

elliptic flow v_2 of di-electrons will help us to understand the behavior of collective flow of different sources, especially for heavy quark sources. The preliminary v_2 results have been presented at the conference of Strange Quark Matter 2011. More precise measurements will come from a factor of two more data at disk, taken in year 2011. Further more, STAR has proposed to take a factor of 4 more p+p and Au+Au data in the next two years. These future data sets will improve the precision of current di-electron spectrum and elliptic flow measurement. It will also provide an opportunity to study the charm modification and QGP thermal radiation in central Au+Au collisions.

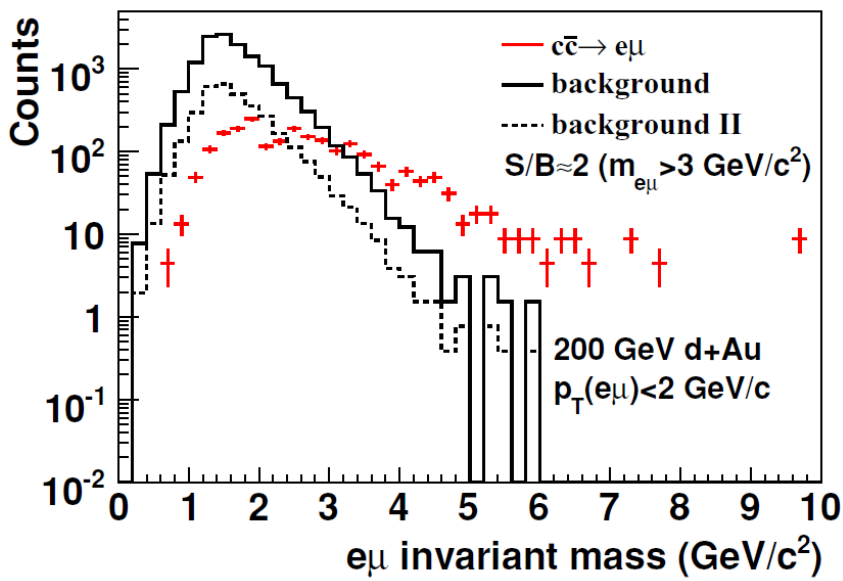

Figure 5.1: The expected electron-muon correlation from charm pair production and from background of random combination in d+Au collisions. The statistics of simulation are equivalent to 2 billion minimum bias d+Au collisions. Figure is taken from [Rua09].

As mentioned in Sec. 2.3, STAR has proposed several detector upgrades which are related to this analysis: Muon Telescope Detector (MTD) [Rua09] and Heavy Flavor Tracker (HFT) [Sha07a, Kap08].

MTD can trigger on di-muon events to obtain high statistics. It will allow us to distinguish the thermal contribution from open charm contribution in IMR by electron-muon correlation. Fig. 5.1 shows the simulation results of the electron muon invariant mass distribution from charm pair production and from background. The cross symbols are the signal. The solid line represents random combinatorial background in d+Au

collisions. The measurement of electron-muon spectrum and v_2 by MTD will address the heavy flavor contribution to the di-lepton spectrum and elliptic flow v_2.

In addition, the HFT upgrade should significantly improve open charm reconstruction in a broad p_T range at mid rapidity. It will measure open charm hadrons, and enable precision study of charm quark collectivity and energy loss.

APPENDIX A

Publication list

Publication List

- *Observation of the antimatter helium-4 nucleus*
  (Principal Author), H. Agakishiev *et al.* (STAR Collaboration), *Nature* **473**, 353, arXiv:1103.3312v2 (2011)

- *Di-lepton production in p+p collisions at 200 GeV from STAR*
  Bingchu Huang (for the STAR Collaboration), J. Phys. Conf. Ser. **316**:012006, doi:10.1088/1742-6596/316/1/012006 (2011)

- *Projection of a measurement of the Non-photonic Electron v_2 in Au+Au Collisions at STAR*
  Bingchu Huang, Yi-Fei Zhang, Zi-Ping Zhang, Zhang-Bu Xu and Xin Dong, *Int. J. Mod. Phys. E* **20**:1701-1708, DOI No:10.1142/S0218301311019507 (2011)

- *Simulation of the enhancement of η' meson's production in p+p collision at 200 GeV*
  Bingchu Huang, proceedings of the 10th International Conference on Nucleus-Nucleus collisions (NN2009), Beijing, China, August 2009, *Nucl. Phys.* **A834**, 313C (2010)

- *Simulation of the enhancement of η meson's production in p+p collisions at 200 GeV*

Bingchu Huang, Yifei Zhang, Ziping Zhang, JOURNAL OF UNIVERSITY OF SCIENCE AND TECHNOLOGY OF CHINA, **38**, 11, (2008)

References

[AB02] M. Achasov and K. et al. Beloborodov. "Measurement of the $\phi \to \pi^0 e^+ e^-$ decay probability." *JETP Letters*, **75**:449–451, 2002. 10.1134/1.1494039.

[Abe09] B. I. Abelev et al. "Systematic Measurements of Identified Particle Spectra in pp, d^+ Au and Au+Au Collisions from STAR." *Phys. Rev.*, **C79**:034909, 2009.

[Abr97] M. C. Abreu et al. "J / psi and Drell-Yan cross-sections in Pb Pb interactions at 158 GeV/c per nucleon." *Phys. Lett.*, **B410**:327–336, 1997.

[Ack03] K. H. Ackermann et al. "STAR detector overview ." *Nucl. Instrum. Meth.*, **A499**:624–632, 2003.

[Ada04] John Adams et al. "rho0 production and possible modification in Au + Au and p + p collisions at s(NN)**(1/2) = 200-GeV." *Phys. Rev. Lett.*, **92**:092301, 2004.

[Ada05a] John Adams et al. "Experimental and theoretical challenges in the search for the quark gluon plasma: The STAR collaboration's critical assessment of the evidence from RHIC collisions." *Nucl. Phys.*, **A757**:102–183, 2005.

[Ada05b] John Adams et al. "Open charm yields in d + Au collisions at s(NN)**(1/2) = 200-GeV." *Phys. Rev. Lett.*, **94**:062301, 2005.

[Ada05c] John Adams et al. "Phi meson production in Au + Au and p + p collisions at s**(1/2) = 200-GeV." *Phys. Lett.*, **B612**:181–189, 2005.

[Ada06] A. Adare et al. "Measurement of high-p(T) single electrons from heavy- flavor decays in p + p collisions at s**(1/2) = 200-GeV." *Phys. Rev. Lett.*, **97**:252002, 2006.

[Ada07a] A. Adare et al. "J/ψ production versus transverse momentum and rapidity in p^+p collisions at $\sqrt{s}$ = 200-GeV." *Phys. Rev. Lett.*, **98**:232002, 2007.

[Ada07b] A. Adare et al. "J/ψproduction vs centrality, transverse momentum, and rapidity in Au+Aucollisions at $\sqrt{s_{\rm NN}}$= 200- GeV." *Phys. Rev. Lett.*, **98**:232301, 2007.

[Ada09] A. Adare et al. "Measurement of Bottom versus Charm as a Function of Transverse Momentum with Electron-Hadron Correlations in p+p Collisions at sqrt(s)=200 GeV." *Phys. Rev. Lett.*, **103**:082002, 2009.

[Ada10] A. Adare et al. "Detailed measurement of the e^+e^- pair continuum in $p+p$ and Au+Au collisions at $\sqrt{s_{NN}} = 200$ GeV and implications for direct photon production." *Phys.Rev.*, **C81**:034911, 2010.

[Ada11] A. Adare et al. "Measurement of neutral mesons in p+p collisions at $\sqrt(s)$= 200 GeV and scaling properties of hadron production." *Phys. Rev.*, **D83**:052004, 2011.

[Adl07a] S.S. Adler et al. "Production of omega mesons at Large Transverse Momenta in p + p and d + Au Collisions at s**(1/2)(NN) = 200-GeV." *Phys.Rev.*, **C75**:051902, 2007.

[Adl07b] Stephen Scott Adler et al. "High transverse momentum eta meson production in p+p, d+Au and Au+Au collisions at S(NN)**(1/2) = 200-GeV." *Phys. Rev.*, **C75**:024909, 2007.

[Aga11a] H. Agakishiev et al. "High p_T non-photonic electron production in p+p collisions at $\sqrt{s}$ = 200 GeV." *Phys. Rev.*, **D83**:052006, 2011.

[Aga11b] H. Agakishiev et al. "Observation of the antimatter helium-4 nucleus." *Nature*, 2011.

[Agg10] M. M. Aggarwal et al. "Measurement of the Bottom contribution to non-photonic electron production in $p + p$ collisions at $\sqrt{s}$=200 GeV." *Phys. Rev. Lett.*, **105**:202301, 2010.

[Ago03] S. Agostinelli et al. "GEANT4: A simulation toolkit." *Nucl. Instrum. Meth.*, **A506**:250–303, 2003.

[All03] C. E. Allgower et al. "The STAR endcap electromagnetic calorimeter." *Nucl. Instrum. Meth.*, **A499**:740–750, 2003.

[All06] John Allison et al. "Geant4 developments and applications." *IEEE Trans. Nucl. Sci.*, **53**:270, 2006.

[Ams08] C. Amsler et al. "Review of particle physics." *Phys. Lett.*, **B667**:1, 2008.

[And03] M. Anderson et al. "The STAR time projection chamber: A unique tool for studying high multiplicity events at RHIC." *Nucl. Instrum. Meth.*, **A499**:659–678, 2003.

[Arn03] L. Arnold et al. "The STAR silicon strip detector (SSD)." *Nucl. Instrum. Meth.*, **A499**:652–658, 2003.

[Arn08] R. Arnaldi et al. "Evidence for radial flow of thermal dileptons in high-energy nuclear collisions." *Phys.Rev.Lett.*, **100**:022302, 2008.

[Arn09a] R Arnaldi et al. "Evidence for the production of thermal-like muon pairs with masses above 1 GeV/c^2 in 158A GeV Indium-Indium Collisions." *Eur. Phys. J.*, **C59**:607–623, 2009.

[Arn09b] R. Arnaldi et al. "Study of the electromagnetic transition form-factors in $\eta \to \mu^+\mu^-\gamma$ and $\omega \to \mu^+\mu^-\pi^0$ decays with NA60." *Phys. Lett.*, **B677**:260–266, 2009.

[BB08] M. Berłowski and Chr. et al. Bargholtz. "Measurement of η meson decays into lepton-antilepton pairs." *Phys. Rev. D*, **77**:032004, Feb 2008.

[BC08] E. L. Bratkovskaya and W. Cassing. "Dilepton production and off-shell transport dynamics at SIS energies." *Nucl. Phys.*, **A807**:214–250, 2008.

[Bed03] M. Beddo et al. "The STAR barrel electromagnetic calorimeter." *Nucl. Instrum. Meth.*, **A499**:725–739, 2003.

[Ber03] F. Bergsma et al. "The STAR detector magnet subsystem." *Nucl. Instrum. Meth.*, **A499**:633–639, 2003.

[BES09] James D. Bjorken, Rouven Essig, Philip Schuster, and Natalia Toro. "New Fixed-Target Experiments to Search for Dark Gauge Forces." *Phys. Rev.*, **D80**:075018, 2009.

[Bet09] Siegfried Bethke. "The 2009 world average of α_s." *The European Physical Journal C - Particles and Fields*, **64**:689–703, 2009. 10.1140/epjc/s10052-009-1173-1.

[Bic06] H. Bichsel. "A method to improve tracking and particle identification in TPCs and silicon detectors." *Nucl. Instrum. Meth.*, **A562**:154–197, 2006.

[BR91] G. E. Brown and Mannque Rho. "Scaling effective Lagrangians in a dense medium." *Phys. Rev. Lett.*, **66**:2720–2723, May 1991.

[BR02] G.E. Brown and Mannque Rho. "On the manifestation of chiral symmetry in nuclei and dense nuclear matter." *Phys.Rept.*, **363**:85–171, 2002.

[BSS88] L. Bergstrom, R. Safadi, and P. Singer. "Phenomenology of $\Sigma^+ \to pl^+l^-$ and the structure of the weak non-leptonic Hamiltonian." *Zeitschrift für Physik C Particles and Fields*, **37**:281–292, 1988. 10.1007/BF01579914.

[CB99] W. Cassing and E. L. Bratkovskaya. "Hadronic and electromagnetic probes of hot and dense nuclear matter." *Phys. Rept.*, **308**:65–233, 1999.

[Cer96] E. Cerron Zeballos et al. "A New type of resistive plate chamber: The Multigap RPC." *Nucl. Instrum. Meth.*, **A374**:132–136, 1996.

[Dam08] S. Damjanovic. "Thermal dileptons at SPS energies." *J. Phys.*, **G35**:104036, 2008.

[Don06] Xin Dong. "The time-Of-flight detector for RHIC / STAR and the related physics." *AIP Conf. Proc.*, **865**:332–337, 2006.

[Dor10] A. E. Dorokhov. "Rare decay $\pi^0 toe^+e^-$ as a Test of Standard Model." *Phys. Part. Nucl. Lett.*, **7**:229–234, 2010.

[DTZ07] K. Dusling, D. Teaney, and I. Zahed. "Thermal dimuon yields at NA60." *Phys.Rev.*, **C75**:024908, 2007.

[DZ09] K. Dusling and I. Zahed. "Low mass dilepton radiation at RHIC." *Nucl.Phys.*, **A825**:212–221, 2009.

[DZ10] Kevin Dusling and Ismail Zahed. "Thermal photons from heavy ion collisions: A spectral function approach." *Phys. Rev.*, **C82**:054909, 2010.

[FG72] Harald Fritzsch and Murray Gell-Mann. "Current algebra: Quarks and what else?" *eConf*, **C720906V2**:135–165, 1972.

[Gav95] R. Gavai et al. "Quarkonium production in hadronic collisions." *Int. J. Mod. Phys.*, **A10**:3043–3070, 1995.

[Gon] Johan Enmanuel Gonzalez. "J/ψproduction in Au+Aucollisions at center of mass energy = 200-GeV." UMI-32-35748.

[GOR68] Murray Gell-Mann, R. J. Oakes, and B. Renner. "Behavior of Current Divergences under $SU_3 \times SU_3$." *Phys. Rev.*, **175**:2195–2199, Nov 1968.

[GW73a] David J. Gross and Frank Wilczek. "Asymptotically Free Gauge Theories. I." *Phys. Rev. D*, **8**:3633–3652, Nov 1973.

[GW73b] David J. Gross and Frank Wilczek. "Ultraviolet Behavior of Non-Abelian Gauge Theories." *Phys. Rev. Lett.*, **30**:1343–1346, Jun 1973.

[Her01] Gunar Hering. "Dielectron production in heavy ion collisions at 158-GeV/c per nucleon." 2001. Ph.D. Thesis (Advisor: Peter Braun-Munzinger).

[HLO03] M. Harrison, T. Ludlam, and S. Ozaki. "RHIC project overview." *Nucl. Instrum. Meth.*, **A499**:235–244, 2003.

[HP74] H and David Politzer. "Asymptotic freedom: An approach to strong interactions." *Physics Reports*, **14**(4):129 – 180, 1974.

[JG61] J.Goldstone. "Field Theories with Superconductor Solutions." *Nuovo Cim.*, **19**:154, 1961.

[Kap08] Jan Kapitan. "Open charm measurement with HFT at STAR." 2008.

[KLP01] F. Karsch, E. Laermann, and A. Peikert. "Quark mass and flavor dependence of the QCD phase transition." *Nucl. Phys.*, **B605**:579–599, 2001.

[KLW90] S. Klimt, M. Lutz, and W. Weise. "Chiral phase transition in the SU(3) Nambu and Jona-Lasinio model." *Physics Letters B*, **249**(3-4):386 – 390, 1990.

[Koc03] L. Kochenda et al. "STAR TPC gas system." *Nucl. Instrum. Meth.*, **A499**:703–712, 2003.

[Lai00] H. L. Lai et al. "Global QCD analysis of parton structure of the nucleon: CTEQ5 parton distributions." *Eur. Phys. J.*, **C12**:375–392, 2000.

[Lan85] L. G. Landsberg. "Electromagnetic Decays of Light Mesons." *Phys. Rept.*, **128**:301–376, 1985.

[Lan03] J. M. Landgraf et al. "An overview of the STAR DAQ system." *Nucl. Instrum. Meth.*, **A499**:762–765, 2003.

[Llo05] W. J. Llope. "The large-area time-of-flight upgrade for STAR." *Nucl. Instrum. Meth.*, **B241**:306–310, 2005.

[Lon] Hui Long. "Midrapidity lambda and antilambda production in Au+Au collisions at the Relativistic Heavy Ion Collider." UMI-30-63922.

[MBC11] J. Manninen, E.L. Bratkovskaya, W. Cassing, and O. Linnyk. "Dilepton production in p+p, Cu+Cu and Au+Au collisions at 200 AGeV." *Eur.Phys.J.*, **C71**:1615, 2011.

[Mic07] Stephen J. Sanders Peter Steinberg Michael L. Miller, Klaus Reygers. "Glauber Modeling in High Energy Nuclear Collisions." *Ann.Rev.Nucl.Part.Sci*, **57**:205–243, 2007.

[Mil07] Alexander Milov. "Multi-Particle Decays of Light Mesons Measured by PHENIX at RHIC." 2007.

[MT85] Larry D. McLerran and T. Toimela. "Photon and Dilepton Emission from the Quark - Gluon Plasma: Some General Considerations." *Phys. Rev.*, **D31**:545, 1985.

[Nak10] K. Nakamura et al. "Review of particle physics." *J. Phys.*, **G37**:075021, 2010.

[Pol73] H. David Politzer. "Reliable Perturbative Results for Strong Interactions?" *Phys. Rev. Lett.*, **30**:1346–1349, Jun 1973.

[Rap01] Ralf Rapp. "Signatures of thermal dilepton radiation at ultrarelativistic energies." *Phys. Rev. C*, **63**:054907, Apr 2001.

[Rap02] Ralf Rapp. "Thermal lepton production in heavy ion collisions." 2002.

[Rua08] Lijuan Ruan. "Prototype Performance of Novel Muon Telescope Detector at STAR." 2008.

[Rua09] L. Ruan et al. "Perspectives of a Midrapidity Dimuon Program at RHIC: A Novel and Compact Muon Telescope Detector." *J. Phys.*, **G36**:095001, 2009.

[RW00] R. Rapp and J. Wambach. "Chiral symmetry restoration and dileptons in relativistic heavy ion collisions." *Adv.Nucl.Phys.*, **25**:1, 2000.

[Rya09] V. Ryabov. "Hadronic decays of light mesons measured by the PHENIX experiment at RHIC." *Nucl. Phys.*, **A827**:395c–397c, 2009.

[Sha06a] M. Shao et al. "Extensive particle identification with TPC and TOF at the STAR experiment." *Nucl. Instrum. Meth.*, **A558**:419–429, 2006.

[Sha06b] M. Shao et al. "Extensive particle identification with TPC and TOF at the STAR experiment." *Nucl. Instrum. Meth.*, **A558**:419–429, 2006.

[Sha07a] A. Shabetai. "The HFT, a Heavy Flavor Tracker for STAR." *Eur. Phys. J.*, **C49**:169–175, 2007.

[Sha07b] R. Shahoyan. "NA60 results on charm and intermediate mass dimuons' production in In In 158-GeV/A collisions." *J.Phys.G*, **G34**:S1029–S1032, 2007.

[Sha09] Ming Shao et al. "Upgrade of the calibration procedure for a STAR time-of-flight detector with new electronics." *Measur. Sci. Tech.*, **20**:025102, 2009.

[Shu78] Edward V. Shuryak. "Quark-Gluon Plasma and Hadronic Production of Leptons, Photons and Psions." *Phys. Lett.*, **B78**:150, 1978. [Sov.J.Nucl.Phys.28:408,1978].

[Sil09] Cesar Luiz da Silva. "Quarkonia measurement in p+p and d+Au collisions at by PHENIX Detector." *Nuclear Physics A*, **830**(1-4):227c – 230c, 2009. Quark Matter 2009 - The 21st International Conference on Ultrarelativistic Nucleus-Nucleus Collisions.

[Sim08] F. Simon et al. "The Forward GEM Tracker of STAR at RHIC." 2008.

[SLW92] Martin J. Savage, Michael E. Luke, and Mark B. Wise. "The Rare decays pi0 → e+ e-, eta → e+ e- and eta → mu+ mu- in chiral perturbation theory." *Phys. Lett.*, **B291**:481–483, 1992.

[SMS06] Torbjorn Sjostrand, Stephen Mrenna, and Peter Skands. "PYTHIA 6.4 physics and manual." *JHEP*, **05**:026, 2006.

[Sun08] Y. J. Sun et al. "New Prototype Multi-gap Resistive Plate Chambers with Long Strips." *Nucl. Instrum. Meth.*, **A593**:307–313, 2008.

[Tan09] Zebo Tang et al. "Spectra and radial flow at RHIC with Tsallis statistics in a Blast-Wave description." *Phys. Rev.*, **C79**:051901, 2009.

[USA07] USA-NSAC. "Long-range plan." 2007.

[Xu08] Yi-chun Xu et al. "Calibration of ionization energy loss at relativistic rise with STAR Time Projection Chamber." 2008.